Post-Cardiac Arrest Myocardial Dysfunction

FOUAD JOHN TAGHAVI

MB ChB, MRCS

Thesis submitted in accordance with the requirements for the degree of Doctor of Medicine

The University of Leeds

School of Medicine

UK

February 2017

Intellectual Property and Publications Statements

The candidate confirms that the work submitted is his own, except where work which has formed part of jointly authored publications has been included. The contribution of the candidate and the other authors to this work has been explicitly indicated below. The candidate confirms that appropriate credit has been given within the thesis where reference has been made to the work of others.

Chapters 2-4 in Thesis contains work from jointly authored publications:

Taghavi, F*., Lee, P*., Yan, P., Ewart, P., Ashley, E. A., Loew, L. M., Kohl, P., Bollensdorff, C., Woods, C. (2012). In Situ Optical Mapping of Voltage and Calcium in the Heart. *PLoS ONE*, *7*(8), e42562. http://doi.org/10.1371/journal.pone.0042562.g005
Figures 1,3,4 & 5 work I was involved with, including conception and design of experiments, performed experiments, analysis of data and writing up.

Taghavi, F*., Woods, C. E*., Shang, C*., Downey, P., Zalewski, A., Rubio, G. R., Liu, J., Homburger, J., Grunwald, Z., Qi, W., Bollensdorff, C., Thanaporn, P., Ali, A., Riemer, R., Kohl, P., Mochly-Rosen, D., Gerstenfeld, E., Large, S., Ali, Z., Ashley, E. (2016). In Vivo Post–Cardiac Arrest Myocardial Dysfunction Is Supported by Ca 2+/Calmodulin- Dependent Protein Kinase II–Mediated Calcium Long-Term Potentiation and Mitigated by Alda-1, an Agonist of Aldehyde Dehydrogenase Type 2Clinical Perspective. *Circulation*, *134*(13), 961–977. http://doi.org/10.1161/CIRCULATIONAHA.116.021618
Figures 1,2,3,4 & 8 work I was involved with, including conception and design of experiments, performed experiments, analysis of data and writing up.

* joint co-authors

Acknowledgements

I am indebted to my supervisor Stephen Large for his continued support, expert advice, guidance and encouragement throughout this venture. I am also grateful to my co-supervisors, Euan Ashley, Mark Drinkhill and Professor Homer, who have provided me with recourses and facilities to complete my investigations; without their motivation and support, this research would not have been possible. I would especially like to thank Chris Woods for his constant support, enthusiasm and mentorship. I am sure he will remain a close friend for the rest of my life. I am extremely grateful to Ayyaz Ali for planting the seed that got me interested in DCD research, teaching me rodent model of cardiopulmonary bypass, and for his help in setting up my research fellowship.

A huge thanks to David Charo who guided me through the lab and taught me how to isolate myocytes and analyze pressure volume loops.

I would like to thank Peter Lee who guided me through imaging and for his construction of the MAT-LAB control device for CF stretch.

I am extremely grateful to Papworth Hospital NHS Foundation Trust for awarding me The Gledhill Fellowship, which enabled me to embark on this project. I would like to express my thanks to my wife Tammy, whom I met during my research fellowship, for her constant love and support. I must finally thank my parents for their support at every step of this journey; I dedicate this thesis to them.

Abstract

One of the major medical advances of the twentieth century is the development of cardiac transplantation. Cardiac transplantation is the definitive treatment for end-stage heart disease. Cardiac transplantation relies on organs procured from Brain Dead Donors (DBD). Donation after Circulatory Death (DCD) organs are being increasingly used for renal, liver and lung transplantation. Hearts from DCD donors have not been utilized as there is a fear that they will have sustained irreversible myocardial injury post cardiac arrest. We have a limited understanding of Post cardiac arrest myocardial depression due to the lack of a good physiological model of the disease. ***Objective:*** To develop a model of *in-vivo* cardiac arrest and resuscitation in order to characterize the biology of the associated myocardial dysfunction and test potential therapeutic strategies. ***Methods and Results:*** We developed a rodent model of post arrest myocardial depression (DCD model) using extracorporeal membrane oxygenation for resuscitation, followed by invasive haemodynamic measurements. In isolated cardiomyocytes, we assessed mechanical load and Ca^{2+}-induced Ca^{2+} release (CICR) simultaneously using the microcarbon fiber technique and observed reduced function and myofilament calcium sensitivity in the post arrest group. Additionally, in contrast with findings from Langendorff models of ischemia-reperfusion, there is a marked augmentation of CICR in isolated cells. This increase in calcium serves to maintain contraction in the face of myofilament dysfunction and, it seems to be mediated by autophosphorylation of calcium-calmodulin protein kinase II (CAMKII). It is further dependent on ryanodine receptor calcium but not PKA leading us to speculate that it is triggered by adrenergic activation but maintained by CAMKII. Finally, activation of aldehyde-dehydrogenase II by the small molecule Alda-1 dramatically improved whole animal and cellular contractile performance after arrest, and restored CICR to close to normal levels. ***Conclusions:*** Cardiac arrest and reperfusion lead to calcium cardiac memory, which support cardiomyocyte contractility in the face of post arrest myofilament calcium sensitivity. Alda-1 mitigates these effects and improves outcome.

Table of Contents

List of Tables

List of Figures

List of Abbreviations

APLAC - Administrative Panel on Laboratory Animal Care

ALDH2 - Aldehyde dehydrogenase II

AP – Action potential

BSD – Brain stem death

CAMKII - calcium-calmodulin protein kinase II

CFFR - calcium-force-frequency-relationships

CI - contractility index

CICR – Calcium induced calcium release

CPB – Cardiopulmonary bypass

CVI - Falk Cardiovascular Research Institute (CVI)

DBD – Donation after brain-stem death

DCD – Donation after circulatory death

EAM – Electromanatomic mapping

ECG – Electrocardiogram

ECMO - Extracorporeal membrane oxygenation

EDLTR - End-diastolic length-tension relationships

EDPVR - End diastolic pressure volume relation

EDPVR - End systolic pressure volume relation

EJV – External jugular vein

EMCCD - Electron-multiplied charge-coupled-device

ESLTR - End-systolic length-tension relationships

FA – Femoral artery

I/R - Ischemia/reperfusion

ICP – Inter cranial pressure

IJ – Internal jugular

ILCOR - International Liaison Committee on Resuscitation

IVC – Inferior vena cava

LED – light emitting diode

LV – Left ventricle

LV – Left ventricle

MAP – Mean arterial pressure

NCX - Sodium calcium exchanger

PA – Pulmonary artery

PCAS - Post-cardiac arrest syndrome

PCAS - Post-cardiac arrest syndrome

PE - Polyethylene

PKA – Protein Kinas A

PMAD - Post-myocardial arrest dysfunction

PRSW - Pre-load recruitable stroke work

PV – Pressure volume

PV – Pressure volume

RV – Right ventricle

RVP – Rapid ventricular pacing

RVU – Relative volume units

RyR - Ryanodine receptor

SCV – Superior vena cava

T – Tau

CHAPTER 1. INTRODUCTION

One of the major medical advances of the twentieth century is the development of cardiac transplantation. Since its introduction this procedure has improved and extended the lives of patients suffering from heart failure and despite advances in medical therapy cardiac transplantation still remains the definitive treatment for end-stage heart disease. Cardiac transplantation relies on donors and their families agreeing to donate their organs.

There are three different ways for people to donate organs for transplantation, these are

- Brain stem death – This is where a person no longer has activity in their brain stem due to a severe brain injury. They have permanently lost the potential for consciousness and the capacity to breathe. This may happen even when a ventilator is keeping the person's heart beating and oxygen is circulated through their blood. This group of donors are called DBD (Donation after Brain Stem Death) donors
- Circulatory death – Is the irreversible loss of function of the heart and lungs after a cardiac arrest from which the patient cannot or should not be resuscitated. It can also be the planned withdrawal of life-sustaining treatment from a patient within the Intensive Care Unit or the Emergency Department. These donors are known as DCD (Donation after Circulatory Death) donors.

- Living donation - Whilst you are still alive you can choose to donate a kidney, a small section of your liver, discarded bone from a hip or knee replacement and also your amniotic membrane (placenta).

The biggest hurdle to treating end-stage heart failure with transplantation is the shortage of suitable donor organs.[1] Currently heart transplantation relies solely on the DBD donors as a source of organs. Over the past fifteen years DCD donors have been a fruitful source of organs substantially increasing the number of successful renal, liver and lung transplantations.[2-6] DCD donors suffer a neurological insult, however, this falls short of fulfilling the criteria for brain-stem death. Due to concerns that periods of ischemia following circulatory arrest may result in severe myocardial injury, donation of hearts after circulatory death (DCD) are not used. However, the earliest successful heart transplants, including the first performed in the world in 1967, utilised organs which had been removed after cardiac arrest and confirmation of death of the donor.[7] Boucek et al in 2008 reported a series of three successful paediatric heart transplantations from donors who had died from cardio-circulatory causes.[8] In 2009, in-situ resuscitation of an adult human heart donated after circulatory death with subsequent weaning from cardio- pulmonary support was reported.[9] If hearts post DCD can be resuscitated sufficiently this would greatly improve the number of available hearts for transplantation. It is estimated that the use of DCD hearts may increase the number of heart transplants by up to 15%.[10] The focus of my investigation was to ascertain whether hearts sourced from a DCD donor

could be resuscitated and recover function in order to allow for successful transplantation.

1.1. Organ donation

Solid organ transplantation was pioneered through the use of organs from DCD donors in the 1960's. In 1968 the Uniform Anatomic Gift Act allowed adults to designate their organs for transplantation after legal declaration of their death.[11] The Harvard Criteria for irreversible coma were developed in 1968 and two different methods for defining death were established.[12] Death was either defined as irreversible cessation of all brain function or the irreversible and simultaneous loss of circulatory and respiratory function. Prior to the development of brain-stem death criteria, organs were predominantly procured under emergent circumstances after the declaration of death. The acceptance of brain-stem death rapidly led to abandonment of organ procurement from DCD donors as organ retrieval could occur under more controlled circumstances in heart beating donors. It was felt that this practise would be associated with improved organ viability and translate into superior clinical outcomes. The reintroduction of organ donation from DCD donors was first evident in the 1980's and was instituted in response to family requests for organ donation.[13-15] However the realisation that the demand for donor organs was beginning to exceed the supply invigorated the development of further programs of transplantation from DCD donors worldwide.[16,17] A decrease in the incidence of brain death began to compound the problems of donor organ shortage, further increasing the importance of alternative sources for organ donation. Improvements in

neuro-critical care have resulted in a group of patients with devastating neurological injury that do not progress towards brain death. The adoption of protocols for DCD donation avoids the loss of viable and potentially transplantable organs from this group of patients with severe neurological insults.[18]

1.2. Cardiac transplantation – UK

The UK national transplant data has shown that across all organs the total number of deceased donors and transplants fell in 2014/15 for the first time in 11 years.[19] This drop may reflect an increasing number of transplants performed over the last 10 years. In the most recent year there have been fewer transplants but an increasing number of patients have been suspended from the transplant list. Donor and transplant numbers from April 2005 to March 2015 and the number of patients registered on the transplant lists are shown in Figure 1.1. There were 169 fewer deceased donor transplants in 2014-2015 than in the previous year, representing a 5% decrease. The corresponding decrease in the number of deceased donors was 3%.

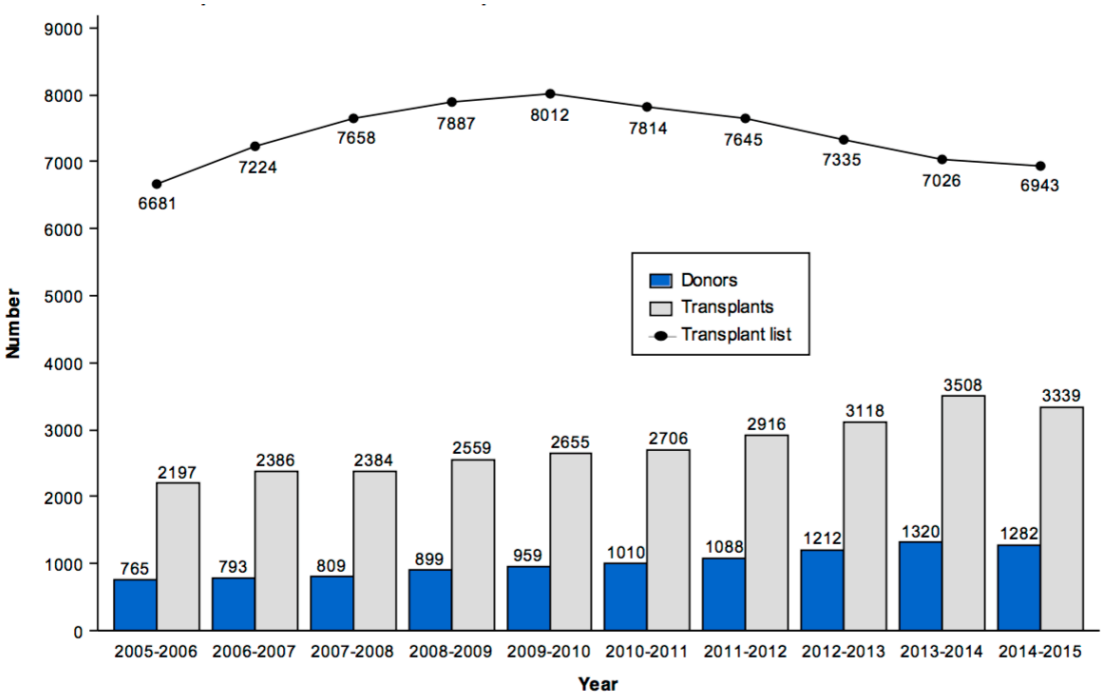

FIGURE 1-1 - NUMBER OF DECEASED DONORS AND TRANSPLANTS IN THE UK, 1 APRIL 2005 - 31 MARCH 2015, AND PATIENTS ON THE ACTIVE TRANSPLANT LIST AT 31 MARCH

When looking across the board at the different types of donors from 2005 - 2015 it is clearly evident that there has been a substantial increase in the number of DCD donors compared to DBD donors.[19] Figure 1.2 shows the number of deceased and living donors in the UK, 1April 2005 – 31 March 2015.

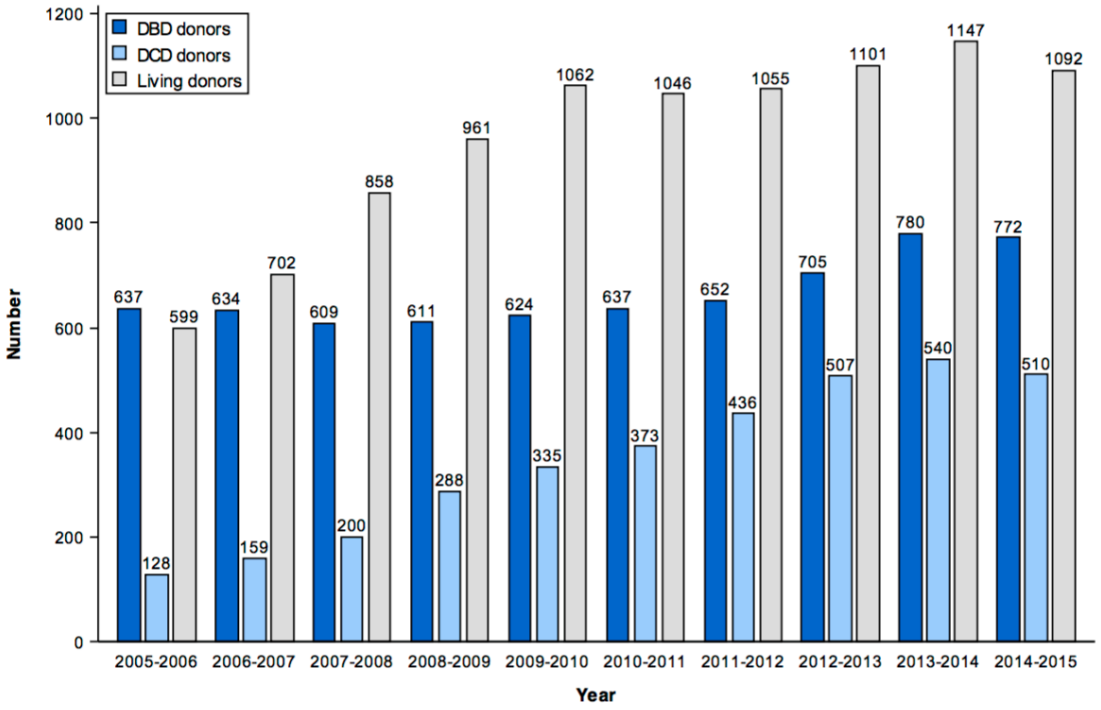

FIGURE 1-2 - NUMBER OF DECEASED AND LIVING DONORS IN THE UK, 1 APRIL 2005 - 31 MARCH 2015

Organs for cardiac transplantation have traditionally come from DBD donors. Heart transplantation is threatened by a shortage of donor hearts.[20] Figure 1.3 shows the number of patients on the active transplant list as of 31st March each year between 2006 and 2015. The number of patient waiting for a heart transplant has increased substantially from 93 in 2009 to 267 in 2015. [21]

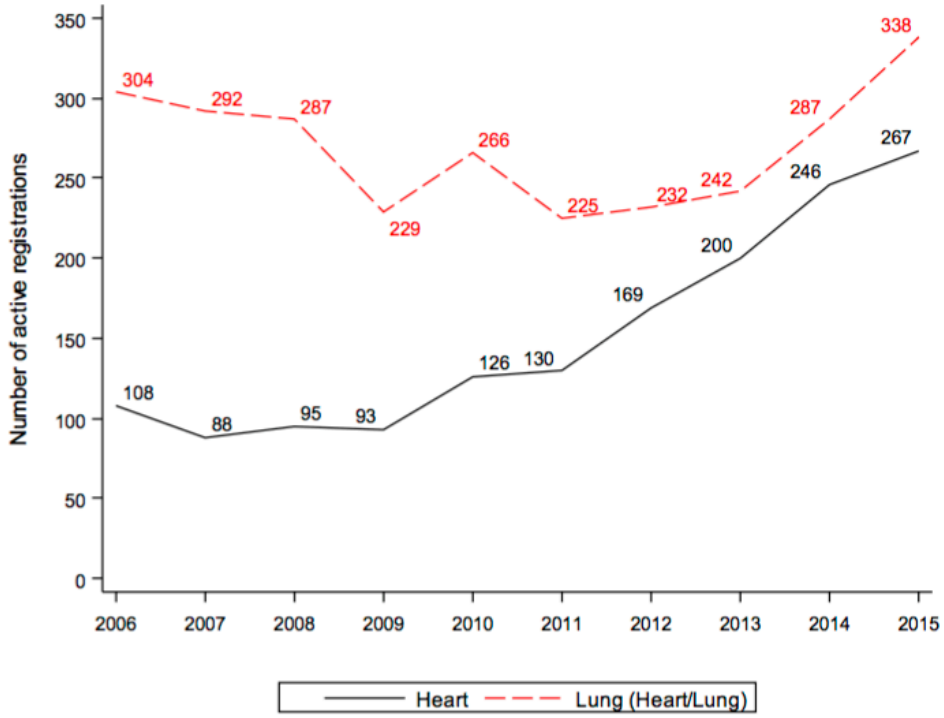

FIGURE 1-3 - NUMBER OF PATIENTS ON ACTIVE TRANSPLANT LIST AT 31 MARCH EACH YEAR, 2006 TO 2015

The figure 1.4 below shows that the number of heart transplantations in the UK remained stable from 2005 – 2012, from 2013 there was an increase in number of hearts transplanted. This increase from 2013 onwards may be due to the implementation of the "Scout" Pilot Programme.[22] Previous studies have demonstrated that early aggressive donor management could lead to increased utilisation of some donor hearts.[23-25] A UK pilot programme was initialised in 2013 which involves sending a member of the cardiothoracic retrieval team, the 'scout', to the donor intensive care unit as soon as consent for organ donation is obtained. Scouts perform donor optimisation with the aim to 1) increase the number of donor hearts retrieved and transplanted and 2) improve the quality of donor hearts retrieved.

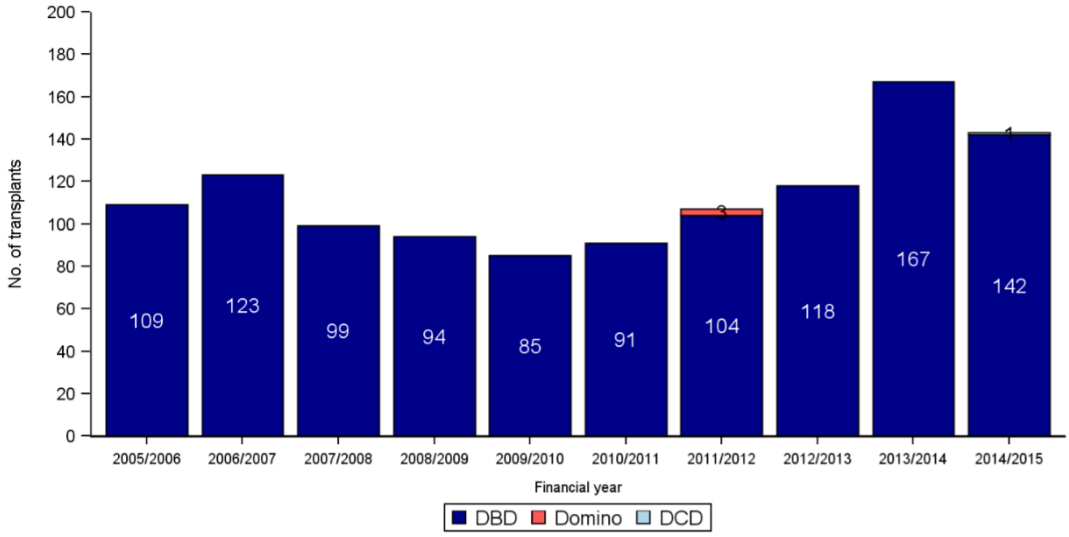

FIGURE 1-4 - NUMBER OF ADULT HEART TRANSPLANTS IN THE UK, BY FINANCIAL YEAR, 1 APRIL 2005 TO 31 MARCH 2015

Figure 1.4 -

Once a patient is placed on the heart transplant waiting list, a suitable donor heart may come along in a few days or it may take years. Unfortunately suitable hearts do not become available for everyone who is on the waiting list. About half the people accepted onto the waiting list receive a transplant within 3 years. [26] Some people on the transplant list who are too unwell to leave hospital and will have to stay in as inpatients until their transplant can be done go onto an “Urgent Heart Allocation” waiting list. Priority is given to these patients.

Figure 1.5 below shows the number of adult heart transplants in the UK from 2005 – 2015 based on the patients’ urgency status.[21] It shows that the chance of a patient receiving a heart transplant while on the non-urgent waiting list is reducing year on year.

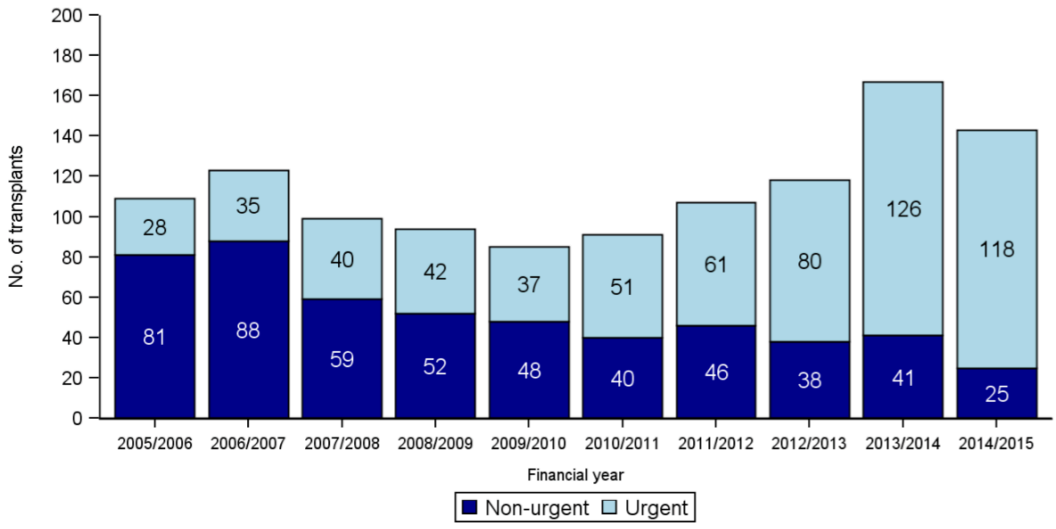

FIGURE 1-5 - NUMBER OF ADULT HEART TRANSPLANTS IN THE UK, BY FINANCIAL YEAR AND URGENCY STATUS, 1 APRIL 2005 TO 31 MARCH 2015

Not all patients placed on the transplant list get transplanted. The figure 1.6 below shows the outcomes of 88 new non-urgent heart registrations to the waiting list from 1 April 2011 to 31 March 2012. [21] The chart shows the proportion of patients transplanted or still waiting six months, one, two and three years after joining the list. It also shows the proportion removed from the transplant list (typically because they become too unwell for transplant) and those who died while on the transplant list. Within six months of listing, 30% of non-urgent heart patients were transplanted while 9% died waiting. Three years after listing only 48% received a transplant.

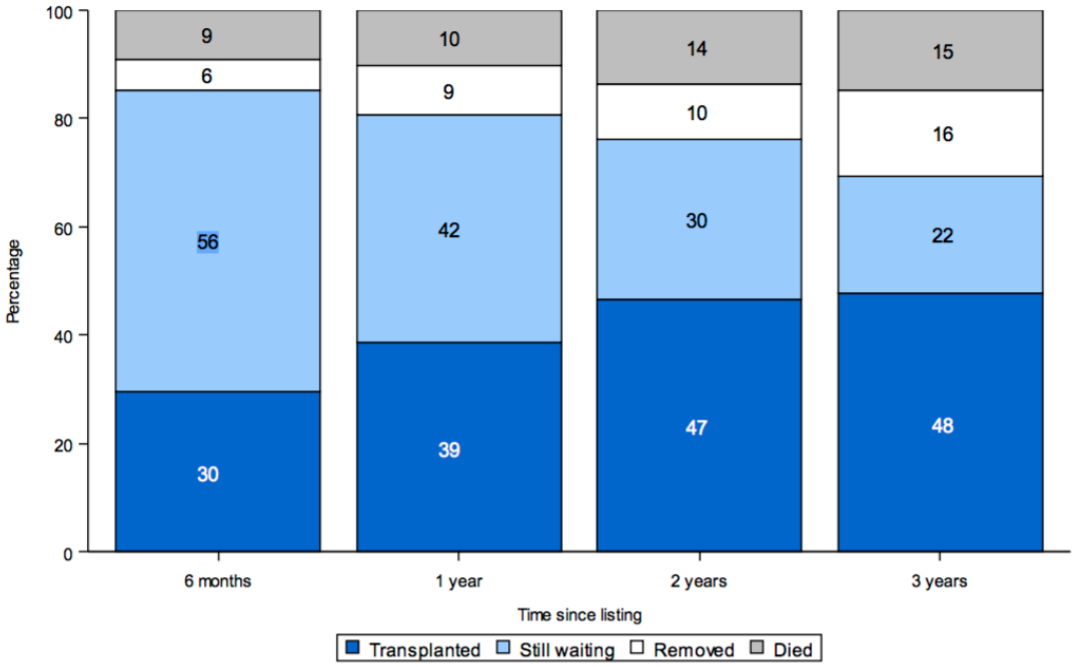

FIGURE 1-6 - POST-REGISTRATION OUTCOME FOR 88 NEW NON-URGENT HEART ONLY REGISTRATIONS MADE IN THE UK, 1 APRIL 2011 TO 31 MARCH 2012

1.3. Cardiac arrest: the final pathway

All DCD donors will succumb to cardiac arrest prior to being declared dead. Therefore a good starting point to investigating these patients is to look at cardiac arrest in the general population. Sudden cardiac arrest is a major cause of death in the Western World.[27] Much effort has gone into both aborting and resuscitating patients after cardiac arrest, but mortality after resuscitation remains 50% for out of hospital and 67% for in-hospital arrest.[28,29] This excess mortality after resuscitation is reflected in the post-cardiac arrest syndrome (PCAS),[28] a condition that potentially encompasses: 1) post-arrest central nervous system dysfunction, 2) post-arrest ischemia/reperfusion (I/R), 3) post-myocardial arrest dysfunction (PMAD); and 4) continuation of the factors precipitating sudden cardiac arrest. PMAD

is believed to be a form of myocardial stunning[30,31] thought to result from a rightward shift in the myofilament calcium sensitivity curve.[32] This stunning has been observed similarly for hypoxic arrest, but also following ventricular fibrillation as well.[33]

In the heart, contraction relies on extracellular Ca entering the cytoplasm through voltage-gated L-type Ca channels. This Ca influx induces opening of ryanodine receptors (RyR), causing them to release Ca stored in the sarcopasmic reticulum. Figure 1.7 shows an illustration of this.[34]

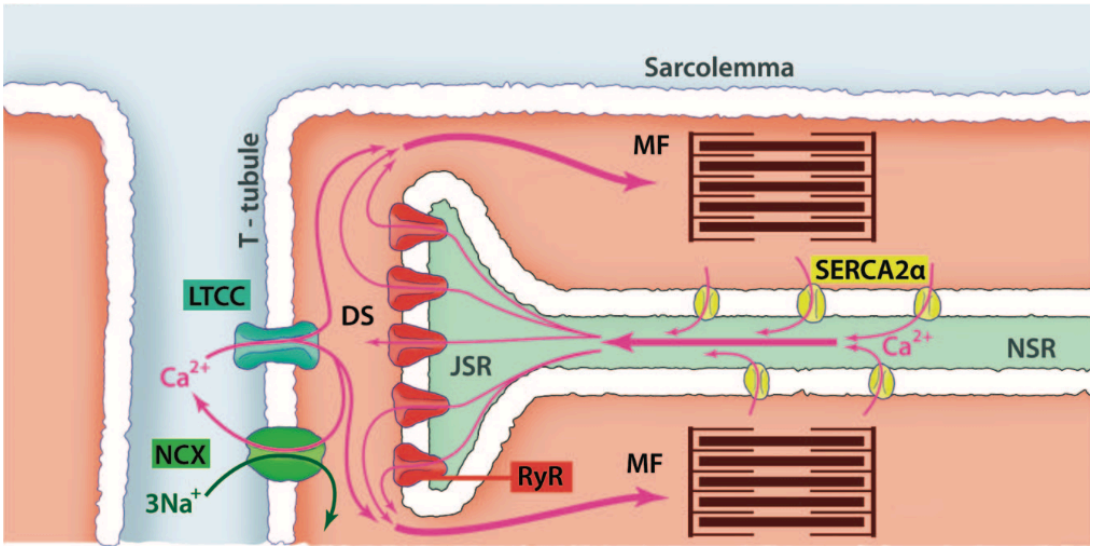

FIGURE 1-7 SCHEMATIC OF A CARDIAC MUSCEL CELL. FORMED BY L-TYPE CA CHANNELS (LTCC) IN THE T-TUBULAR MEMBRANE AND RYRS IN THE APPOSED JUNCTIONAL SR (JSR). EXTRACELLULAR CA ENTERING THROUGH LTCC TRIGGERS RYRS TO OPEN, RELEASEING SR CA INTO THE DIADIC SPACE (DS) AND MYOPLASM (MYO) TO ACTIVATE THE MYOFILAMENTS (MF). CA IS THEN PUMPED BACK INTO THE NON-JUNCTIONAL SR (NSR) BY A CA PUMP (SERCA2A) OR EXTRUDED FROM THE CELL VIA NA/CA EXCHANGE (NCX).

At a cellular level, it is hypothesized that oxidative stress contributes to cytosolic calcium overload which leads to reversible myofilament dysfunction and irreversible cell death,[35,36] the last mediated by mitochondrial calcium loading and initiation of the cell death pathway.[37] Calcium overload has been

explained by two processes: reverse mode operation of the sodium calcium exchanger (NCX) related to intracellular sodium overload during ischemia and sarcoplasmic reticulum ATPase (SERCA) dysfunction related to ATP depletion.[38] Importantly, however, ryanodine receptor (RyR) dependent calcium release has also been shown to support reversible injury,[39] and at the same time these processes can promote irreversible injury via calcium/calmodulin dependent protein kinase II (CAMKII) signalling pathways. The relationship between NCX induced calcium overload and augmentation of calcium induced calcium release (CICR) is critical because CICR generates systolic and diastolic levels an order of magnitude higher in localized domains on a beat to beat basis than that which has been predicted to occur during the very brief (relative to the persistent PMAD phenotype) NCX induced cytosolic calcium overload associated with I/R. However, despite that biochemical pathways modulated during I/R would predict augmented CICR, no long lasting changes in CICR have been demonstrated following reperfusion[40] except for one early report.[38,41] One possible reason for this is that much work in I/R has relied on the explanted Langendorff preparations circulated with saline. The present experiments were carried out in an attempt to overcome some of these limitations. Specifically, because CAMKII signalling has been linked to beta-adrenergic signalling under pathological conditions,[42] and because sudden cardiac arrest has been associated with dramatic elevations in catecholaminergic signalling,[43] we felt that a model including the neurohormonal axis was important. In addition, to date most single cell studies have been carried out using unloaded cardiac mycoytes. Here, we use an *in vivo* model of cardiac

arrest with resuscitation using extracorporeal membrane oxygenation (ECMO) and examined both cellular force and CICR in isolated, loaded ventricular myocytes.

1.4. In Situ Optical Mapping of Voltage and Calcium in the Heart

As we believe that the neurohormonal axis is important we wanted to measure CICR and voltage in-vivo. Electrophysiological testing is a mainstay of clinical arrhythmia diagnosis. For simple arrhythmias, this involves a limited number of intracardiac electrogram measurements. But for complex arrhythmia, where mechanisms often are associated with underlying structural heart disease, spatially-resolved electroanatomic mapping (EAM) improves the efficacy of ablation.[44] The principle behind EAM relies on registering electrical measurements in three-dimensional space to determine the tissue location underlying the arrhythmia focus. However, EAM catalogs the spatial context of electrical signals using an external localization system and triangulates position relative to a reference patch placed externally,[45] rather than by directly visualizing underlying cardiac tissue anatomy and physiology simultaneously.[44]

By comparison, basic science studies of arrhythmia have tended to rely on the higher spatiotemporal resolution of optical mapping using fluorescent probes both to image anatomy directly and to measure relevant physiological parameters such as transmembrane voltage (V_m) and intracellular calcium ($[Ca^{2+}]_i$) dynamics.[46,47] Using the isolated Langendorff-

perfused mammalian heart, optical mapping of these two key parameters has played a pivotal role in arrhythmia research.[48,49] V_m mapping has also been used to delineate normal, peri-infarct, and scarred tissue rapidly in the in vitro setting.[50] Yet, the use of optical mapping in vivo has only been published once to our knowledge (in 1998).[51] In our view, this is largely because it is experimentally challenging. However, a number of continued technological developments have now made the applicability of optical mapping to in vivo preparations more feasible, opening the door to beginning the process towards clinical development of an optical mapping tool [52]. Specifically, second-generation voltage-sensitive dyes with enhanced photo-stability and emission spectra in the near-infrared range have been developed, making them suitable for imaging in the presence of blood [53]. In addition, modern camera frame-rates permit simultaneous multi-colour imaging using a single detector,[54] in particular if combined with multi-band emission filters for optical mapping.[55] Moreover, conventional light sources can be replaced now by powerful light-emitting-diodes (LEDs) which we and others have demonstrated to offer stable illumination that can also be switched on or off with nanosecond-microsecond response times, simplifying multi-parametric imaging.[56] Based on these developments, in combination with a multi-band emission filter, we present a multi-parametric single-camera multi-LED imaging system and show its suitability for in vivo cardiac electrophysiology data acquisition.

1.5. Hypothesis

Our hypothesis is that the DCD heart can be resuscitated after circulatory arrest and recover sufficient function to allow for transplantation, increasing the much needed donor pool to meet current demands. As cytosolic calcium overload which leads to reversible myofilament dysfunction and irreversible cell death is central to the functioning of the organ is would seem appropriate to try and minimise the calcium overload and improve the function of the heart. To test our hypothesis we developed small animal model of DCD heart resuscitation. For purposes of control we utilized a small animal model of DBD. Following global myocardial ischemia in the DCD we instituted in-vivo extracorporeal membrane oxygenation (ECMO) reperfusion to resuscitate the heart. Load-independent contractility of DBD and DCD hearts was acquired using pressure-volume conductance catheters. In addition we examined cellular force in vitro using microcarbon fibre assessment simultaneously with CICR measurements

The forthcoming chapters outline the methodology and the results of our investigation into the feasibility of resuscitating hearts from DCD donors. Our aim was to determine the suitability of these organs for clinical heart transplantation and ascertain any potential targets for therapeutic intervention.

CHAPTER 2.METHODS

This Chapter contains all the methodologies used for experimental procedures and investigations in this thesis.

2.1. RATS

Studies and ethics were approved by the Stanford University Administrative Panel on Laboratory Animal Care and conform to the Guide for the Care and Use of Laboratory Animals published by the National Institutes of Health. Experimental protocols were submitted to the Administrative Panel on Laboratory Animal Care (APLAC) at Stanford University and subsequently approved prior to conducting our investigation.

2.1.1. SOURCE OF ANIMALS

Male Sprague-Dawley rats obtained from Charles River Laboratories, USA were utilized for my experiments.

2.1.2. HOUSING

Animals were housed at the Falk Cardiovascular Research Institute (CVI), Stanford University Medical Center. Temperature controlled cages (20^{o}C to 22^{o}C) were used and the maximum number of animals per cage was limited to three. A 12-hour light - dark cycle was used and animals were given free access to sterile water.

2.1.3. DIET

All rats were given unlimited access to formulated chow. The composition in g/kg was: cereal products 769.5, Hipro soya 140, animal proteins 50, soy oil 8 and mineral mix 32.5)

2.1.4. EXPERIMENTAL SURGERY

Operations were performed in 12-14 week old male Sprague-Dawley rats with an approximate weight of 250 - 300 grams. All procedures were undertaken only after approval of the experimental protocol by our institutional APLAC committee.

2.2. RODENT MODEL OF CARDIAC RESUSCITATION AFTER CIRCULATORY ARREST IN THE DCD DONOR

2.2.1. Ventilation and venous access

The animal was placed in an anaesthetic chamber for induction with isoflurane. The isoflurane vaporizer was adjusted for insufflation of 2-3% isoflurane with an oxygen flow rate of 1-1.5 L/min. After adequate anaesthesia was achieved the animal was removed from the chamber and weighed. Following this the animal was transferred to the operating area and placed on an electric heat pad in a supine position. A nose cone was fitted onto the animal and maintenance of anaesthesia was achieved with 1-2% isoflurane. Oxygen was delivered at a flow rate of 1-2 L/minute. Adequacy of anaesthesia was ensured by a foot pinch manoeuvre and any reaction to

pain was carefully observed. The position of the animal was then secured to the operating area with tape. The temperature probe from the heat pad (ML295/R homeothermic controller and plate, ADInstruments) was inserted into the rectum to monitor body temperature, which was maintained between 35.5^{o}C and 37^{o}C.

A small skin incision was made over the right groin allowing femoral vessels to be identified in the inguinal region. Both femoral artery and vein were dissected out. The inguinal ligament was reflected superiorly to better visualise the vessels proximally. The distal end of the femoral vein was ligated with a 5.0 silk and a small vascular clamp was placed proximally. Following a small venotomy the vessel was cannulated with polyethylene tubing (PE 20). The proximal clamp was released and the tubing advanced further in, this venous access line was secured in place using 5.0 silk ties. The distal end of the tubing was connected to a 28 gauge needle and a 1cc syringe. Adequacy of venous access was assessed by aspirating venous blood and injecting 0.5ml of 0.9% normal saline. This establishes venous access for administration of fluids and medication.

2.2.2. Tracheostomy and mechanical ventilation

A cervical incision was made using dissecting scissors. Blunt dissection was used to expose the trachea. Microsurgical scissors were used to make a small transverse tracheotomy. A 16 gauge intravenous catheter was inserted into the trachea and connected to previously assembled ventilator tubing (Figure 2.1). Mechanical ventilation was commenced using a Harvard

Apparatus 683 small animal ventilator. The ventilation rate was set at 60 strokes per minute with a tidal volume of 3-4 cc. The oxygen flow rate was maintained at 1-2 L minute and 1- 2% isoflurane was continued for maintenance of anaesthesia. The previously sited nose cone was removed and the tracheostomy cannula was secured with a 5.0 silk suture.

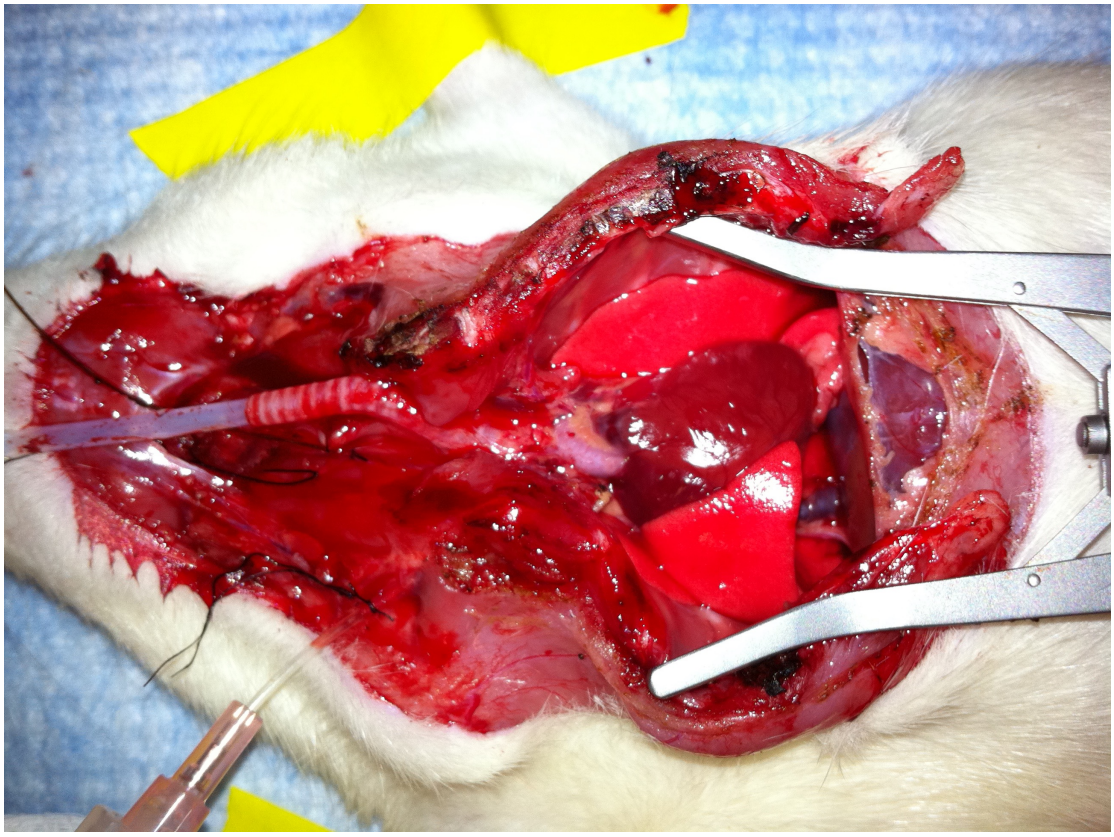

FIGURE 2-1– TRACHEAL INTUBATION

2.2.3. Median Sternotomy

A vertical midline skin incision was made over the sternum and xiphoid process. The xiphoid was excised and the diaphragm dissected free from its attachment to the sternum and costal cartilages. The lower end of the sternum was retracted upwards to visualise the heart and the lungs. The thymus and mediastinal fat was bluntly separated from the internal surface of the sternum and anterior chest wall to which it is often adherent. The

sternum was then divided with electrocautery (Geiger Therma Cauterizer) with caution to avoid the right and left internal thoracic arteries. The sternum was then retracted using a miniature finiochietto retractor (Fine Science Tools, USA) to expose the heart, lungs and great vessels (Figure 2.2). To facilitate visualisation of the heart and great vessels the thymus can be removed with electrocautery. Alternatively, this step can be avoided if exposure of the heart and lungs is not desired.

2.2.4. Arterial cannulation for extracorporeal membrane oxygenation (ECMO) inflow

The animal was administered 100 units of heparin (0.1 ml of 1000 units/ml preparation). The femoral artery had already been dissected during the preparation for venous cannulation of the femoral vein. The distal end of the femoral artery was ligated using a 6.0 silk suture. This ligature was used to retract the artery distally to optimise its exposure for cannulation. A small haemostatic clamp was applied as proximally as possible to occlude the femoral artery. 4.0 mm tygon tubing was connected to a 24 gauge angiocath cannula with a three-way stopcock at the proximal end. This assembly constituted the femoral arterial catheter and served as the inflow route for our ECMO circuit. The apparatus was then primed with normal saline to evacuate air. The three-way stopcock was positioned such that it occluded the proximal end of the cannula to avoid loss of priming fluid. A small arteriotomy was made at the distal end of the femoral artery. Forceps were used to gently dilate the arteriotomy site and the angiocath cannula was advanced into the femoral artery. Approximately 5 mm of the length of the

cannula was advanced into the femoral artery. The cannula was secured with two 5.0 nylon ligatures to compress the vessel against the internal cannula. The clamp previously placed on the femoral artery was removed, a pulsatation was then observed in the column of blood within the cannula confirming adequate positioning. The arterial clamp is then reapplied to the artery to prevent drainage of arterial blood into the cannula, which may precipitate hemodynamic instability. The animal was then rotated 180 degrees such that the head was positioned closest to the operator.

Figure 2.2 below shows the animal taped down to the operating mat with both femoral vein and artery cannulated.

FIGURE 2-2 – FEMORAL ARTERY AND VEIN CANNULA

2.2.5. Insertion of pressure-volume conductance catheter

Continuous acquisition of hemodynamic data was used to complement the procedure and allow for precise monitoring of arterial pressure before and after the experiment. The right common carotid artery was dissected starting in the cervical region. The vessel was separated from the vagus nerve. If a median sternotomy had been performed the vessel was be dissected as far proximally as the aortic arch to make cannulation easier. The carotid artery was ligated as distally in the neck as distal as possible with a 6.0 silk suture. A small occlusive clamp was used to occlude the carotid artery proximal to the site of intended cannulation. A small arteriotomy was made in the artery distally using microsurgical scissors. A 1.4 Fr Millar ultra-miniature pressure-volume (PV) conductance catheter (SPR 839, Millar Instruments, Houston, Texas) was inserted into the vessel through this incision and secured with a 6.0 silk ligature. The vascular clamp was removed and the catheter was advanced retrograde into the aortic arch. The catheter was connected to a Millar Ultra pressure volume system (Millar instruments, Houston) for the acquisition of hemodynamic data. Hemodynamic data was viewed and analysed using Labchart 7 software (ADI instruments). Arterial blood pressure was measured directly from the ascending aorta. After acquisition of baseline haemodynamic data the PV catheter was advance into the LV by crossing the aortic valve. The catheter was manipulated until both the pressure and volume signals were optimised. Baseline PV data from the LV was acquired. The IVC was occluded in order to change the pre-load of the heart, this allows for generation of a series of PV loops for calculation of load independent contractility and compliance. After baseline PV loops were

acquired the catheter was withdrawn into the ascending aorta. To obtain RV pressure volume loops the PV catheter was inserted in a retrograde fashion into the RV through a stab incision in the pulmonary artery.

2.2.6. PV conductance catheter calibration

The volume conductance signal is non-calibrated and needs to be converted to absolute volumes if actual volume status is to be ascertained.

The calibration procedure involves the use of a cuvette comprised of cylinders of known volumes. Using the calibration cuvette a blood sample from the animal was obtained in order to convert arbitrarily assigned relative volume units (RVU) to true volume units such as µl. The cuvette is comprised of a number of cylinders of known and increasing volumes. Freshly drawn blood from a heparinised animal was used to fill the cylinders. The conductance changes were noted in the volume channel on labchart and the RVU value for each cylinder was recorded. The conductance outputs obtained from each of the cylinders can be correlated with the known cylinder volumes to develop a calibration equation for conversion of RVUs into true volume units.

2.2.7. Jugular venous cannulation

A 20 G angiocath cannula was used as the venous cannula, this cannula required modification with two extra holes at its distal end to aid with venous drainage. Prior to cannulation the cannula was attached to a length of 4.0mm tygon tubing with a three way tap at the end and was primed with normal saline to evacuate the air.

The right jugular vein was dissected circumferentially in the cervical region to allowing the passage of a 6-0 ligature beneath the vessel. The vessel was ligated as distal as possible such that there was a sufficient length proximally above the clavicle to allow for cannulation. The distal ligature was retracted to facilitated exposure of the jugular vein. A small haemostatic clamp was applied proximally to occlude the jugular vein. A small venotomy was made at the distal end of the jugular vein. Forceps were used to gently dilate the venotomy site and the angiocath cannula was advanced into the jugular vein. A ligature was loosely placed around the jugular vein to secure the cannula, following which the clamp occluding the vessel was removed. The cannula was then advanced under direct vision into the superior vena cava. The cannula should be held with an angulation of approximately 15 degrees from the anterior surface of the clavicle.

Figure 2.3 below demonstrates internal jugular cannulation with the 20G angiocath, PV conductance catheter inserted into the right carotid artery, in addition to the cannulation of the femoral vessels.

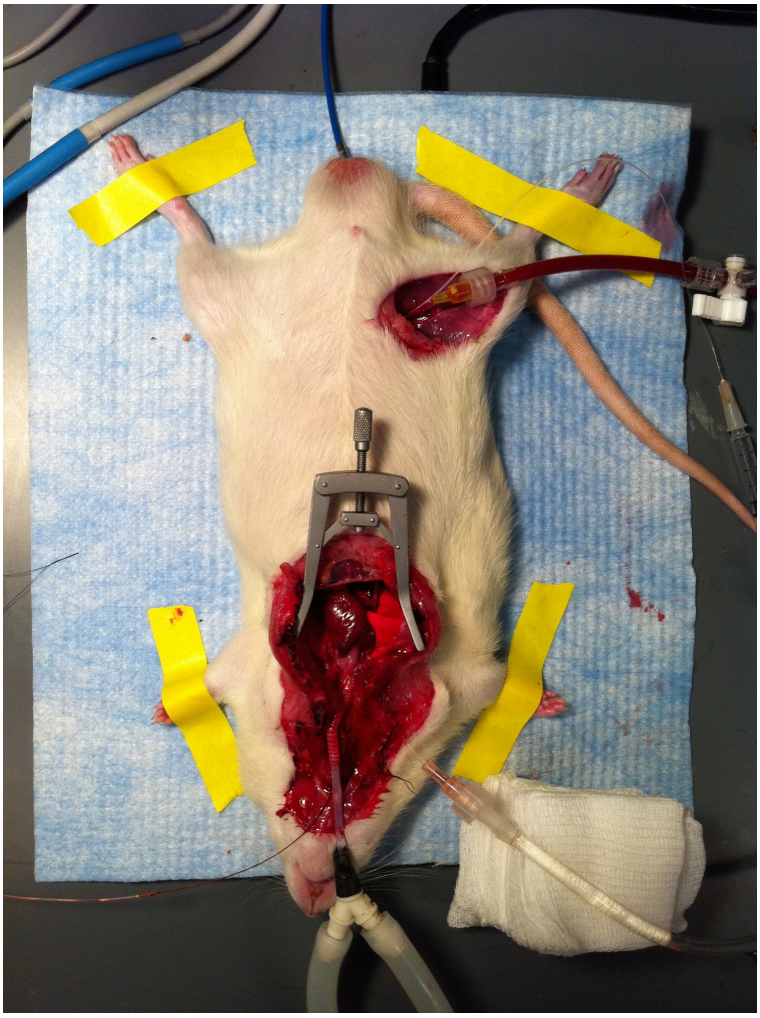

FIGURE 2-3 - IV ACCESS AND MONITORING CANNULATIONS

2.2.8. ECMO circuit

A micro-peristaltic pump (Digital Reglo pump model 1329, Ismatec Ltd, Glattbrugg, Switzerland) was utilised for propulsion within the circuit. The pump was attached to the ECMO circuit through a customised pump cassette (Ismatec Ltd, Glattbrugg, Switzerland). 4.0 mm Tygon tubing was used as tubing for the circuit. A miniature oxygenator device (Living systems inc., Vermont, U.S.A.) was secured into the arterial limb of the circuit (Figure 2.4). Heparinised saline (20 units/ml) was used to prime the oxygenator and the tubing evacuating all the air. The prime volume of the circuit was 5mls,

this affects the haematocrit and therefore a different calibration for the conductance catheter is used.

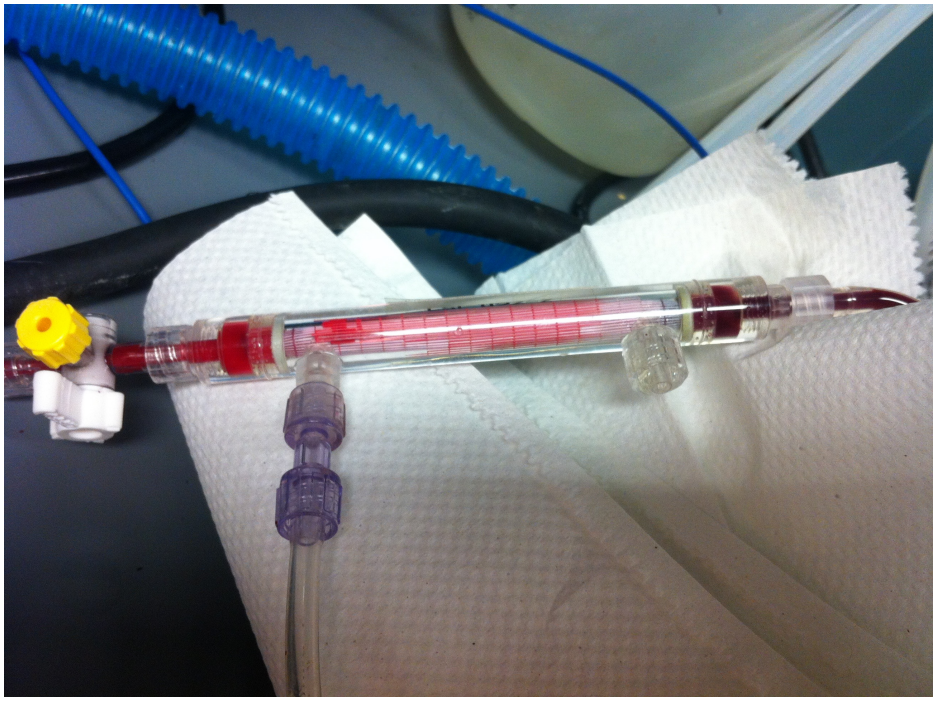

FIGURE 2-4 – MEMBRANE OXYGENATOR SHOWING DEOXYGENATED BLOOD AT THE INFLOW END, SIDE PORT FOR ATTACHMENT OF OXYGEN AND OXYGENATED BLOOD AT THE OUT-FLOW END.

Figure 2.5 below shows a schematic of the ECMO circuit

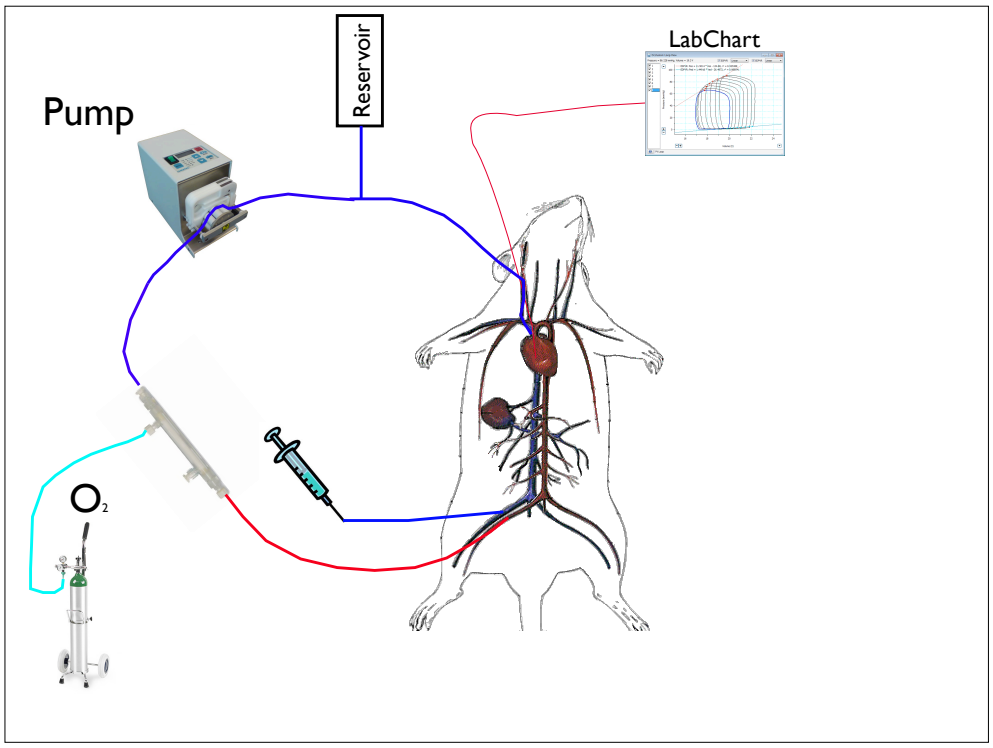

FIGURE 2-5 - FIGURE 2.5: SCHEMATIC OF ECMO CIRCUIT

The pump and associated apparatus were positioned to the right of the animal as show in figure 2.6. A 10 ml syringe filled with normal saline was attached to the circuit and acted as reservoir. Infusion of volume from the syringe was used to support ECMO perfusion and maintain flow if there was a reduction in venous drainage. A Y-circuit was constructed to allow for oxygen to be directed into both the oxygenator and also the ventilator. Using this configuration the route of oxygenation of the animal could be alternated between mechanical ventilation of the lungs via the tracheostomy and ECMO.

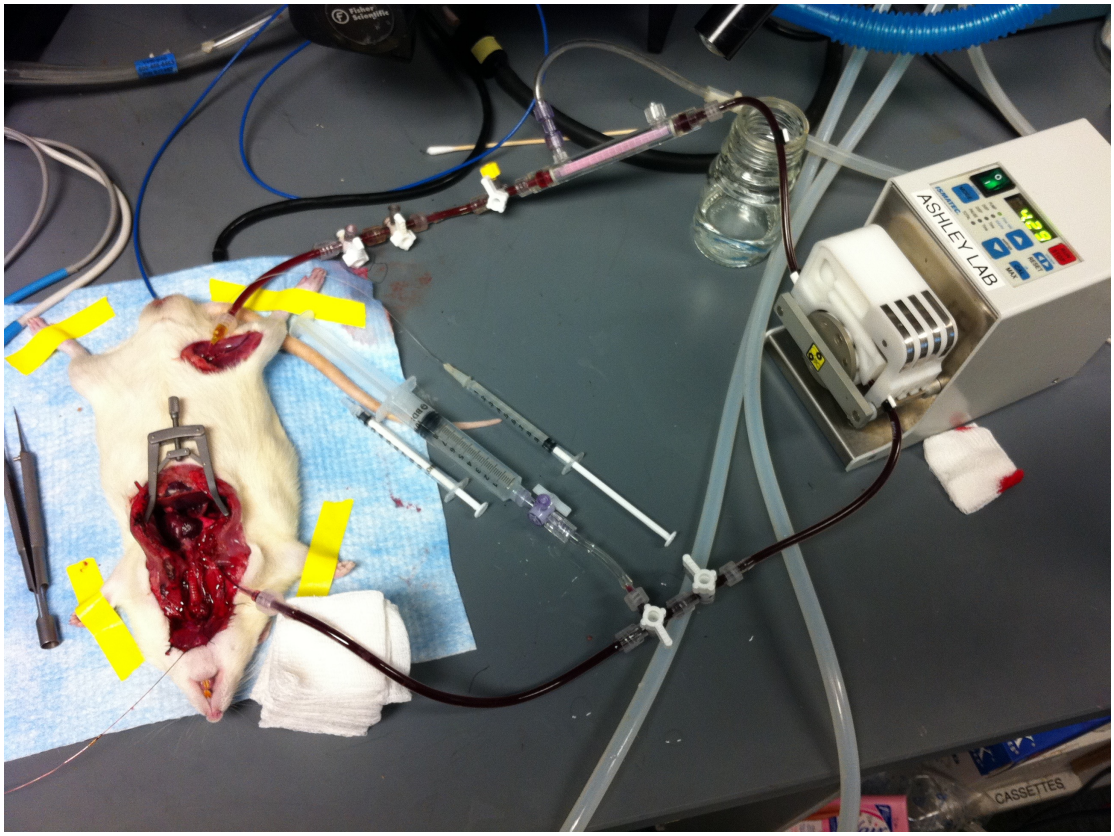

FIGURE 2-6 - SETUP OF THE ECMO CIRCUIT

2.2.9. Cardiac arrest and cessation of circulation

After cannulation for ECMO a further 400 units of heparin was administered intravenously. Both common carotid arteries had previously been ligated, thereby preventing cerebral perfusion and ensuring that inhalational anaesthesia could be discontinued without recovery of consciousness. Sudden cardiac arrest was initiated either by cessation of ventilation or by rapid ventricular pacing to induce ventricular fibrillation. For hypoxic arrest the tracheal cannula was removed from the tracheostomy site and a clamp was used to occlude the trachea. Hypoxia ensued and was followed by onset of hemodynamic instability. Tracheal occlusion culminated in hypoxic cardiac arrest. Ventricular fibrillation was induced by rapid ventricular pacing.

With both techniques the haemodynamics and arterial blood pressure were continuously monitored using the previously sited PV conductance catheter in the ascending aorta. The time from tracheal occlusion or ventricular fibrillation to cardiac arrest was documented. Following circulatory arrest the animal was subjected to a period of warm ischemia. The prevailing core body temperature during this period was maintained between 35 - 37 ^{o}C. The duration of warm ischemia observed was 15 minutes. We observed no differences between these 2 modes of cardiac arrest.

2.2.10. Cardiac resuscitation using ECMO

After the warm ischemic period had elapsed ECMO was commenced. Deoxygenated venous blood was drained via the jugular venous cannula and pumped through the membrane oxygenator. Oxygenated blood was then returned to the animal via the femoral arterial cannula. Pump flow rate was gradually increased until the perfusion pressure was approximately 50-60mmHg. Arterial blood samples were serially acquired for blood gas analysis. Acidosis was treated with intravenous administration of 8.4% sodium bicarbonate. Occasionally perfusion pressure needed to be augmented via intravenous injection of 0.1 mg of phenylephrine. Reperfusion of the coronary circulation was followed by cardiac reanimation with recovery of heartbeat, rate and rhythm. After 20 minutes of reperfusion and return of coordinated cardiac contraction, mechanical ventilation was recommenced and ECMO was discontinued. Consequently, the resuscitated heart was responsible for supporting the circulation. The PV conductance catheter was advanced into the LV via the ascending aorta. PV data was

acquired for measurement of load-independent contractility and compliance of the resuscitated LV. Temporary IVC occlusion was undertaken to reduce preload for the acquisition of a series of PV loops. 30 minutes after cardiac resuscitation satisfactory LV and RV PV loops were obtained, after which the conductance catheter was removed from the carotid artery or the pulmonary artery. The heart was excised for subsequent histological and molecular analysis. After excision a portion of the hearts were placed in a tissue freezing medium formulated with soluble glycols and resins and stored at -80^{o}C, the other hearts where used to isolate cardiac myocytes. The animal was euthanized via exsanguination and the carcass was disposed.

2.3. RODENT MODEL OF BRAIN STEM DEATH (DBD)

2.3.1. Ventilation and venous access

Anaesthesia, venous access and monitoring were undertaken as detailed above.

2.3.2. Tracheostomy and mechanical ventilation

Tracheostomy and mechanical ventilation were established as detailed above

2.3.3. Median Sternotomy

Median sternotomy undertaken as described above in order to expose the heart and the great vessels.

2.3.4. Insertion of pressure-volume conductance catheter

This was carried out as described above. LV and RV pressure-volume data was acquired for the measurements of load-independent ventricular contractility and compliance. The PV catheter was then placed into the ascending aorta for haemodynamic monitoring.

2.3.5. Brain stem death induction

The animal was placed in a supine position with head elevated. A skin incision was made over the right hemicranium to expose the periosteum of the skull. Using electrocautery the periosteum was dissected from the underlying bone. A 1.4 mm drill-bit was used to produce a burr hole in the right parietal bone. A 2 Fr Fogarty balloon catheter (Edwards Lifesciences, Irvine, California) was inserted into the cranial cavity. The balloon was then slowly inflated in the subdural space with 0.5 ml of sterile water over 2 minutes.[57] This manoeuvre consistently resulted in an increase in ICP with compression and herniation of the brain-stem. BSD was confirmed through observation of a hyperdynamic response with tachycardia and hypertension. Further confirmation of BSD was undertaken using an apnoea test. Administration of isoflurane was discontinued and the ventilator was switched off. Absence of any respiratory effort in the anaesthetised animal was taken as further confirmation of BSD. Two hours after the induction of BSD, the conductance catheter was reintroduced into the LV and RV in order to acquire PV loops. Arterial blood samples were removed for analysis of gas exchange and plasma biochemistry. The heart was excised for

subsequent isolation of cardiac myocytes. The animal was euthanised via exsanguination and the carcass was disposed.

2.4. Sham experiments

Sham experiments with the ECMO circuit running for 30 minutes in control animals yielded normal values in isolated cells. Control animals refer to no ECMO unless otherwise stated.

2.5. Pharmacological reagents

Epinephrine infusion was performed with 23 μg/kg/min for 30 minutes through the internal jugular vein.

To inhibit CAMKII, 1 mg of KN93 (Sigma) or 100 μg of myristoylated-AIP (Calbiochem) was used.

To inhibit PKA, 1 mg of H89 (Sigma) was raised in 1 cc of 0.9% normal saline and infused over 10 minutes.

Experimental protocols were initiated 10 minutes after infusion. For experiments with Alda-1, 0.0324g of Alda-1 dissolved in 2ml of 50%PEG/50%PBS and was injected intraperitoneally one hour before establishment of the cardiac arrest model.

In the isolated myocyte experiments, cells were exposed to 100 nM of epinephrine in the extracellular solution.

2.6. Isolation of ventricular cardiac myocytes.

Following each experiment adult ventricular cardiac myocytes were isolated from the rats based on previously published protocols.[58]

Briefly, the heart was excised and retrogradely perfused at 37°C with a calcium free solution containing (in mM) 120 NaCl, 14.7 KCl, 0.6 KH_2 PO_4, 0.6 Na_2 HPO_4, 1.2 $MgSO_4$ -7H_2O, 4.6 $NaHCO_3$, 10 Na-HEPES, 30 taurine, 10 2,3-butanedione monoxime, and 5.5 glucose (pH 7.0) for 4 min followed by an enzymatic digestion with collagenase type 2 (Worthington Biochemical, Lakewood, NJ) 394 U/mg. Figure 2.7 below shows the excised heart suspended in the Langendorff, figure 2.8 shows a close up of the excised heart. The digestion was initially performed in calcium free solution for 2 min, and $CaCl_2$ was then added for a final concentration of 50 M and perfused for an additional 6 minutes. The heart was then removed, and the LV and RV were separated. Each ventricle was first cut into small pieces and then further digested by gently pipetting with plastic transfer pipettes for 3–5 min. Stop buffer [calcium free solution + 12.5 mM $CaCl_2$ + 10% bovine calf serum (Hyclone, Logan, UT)] was added, and the cell suspension was collected in a 15-ml tube and using a Sorvall RT6000B benchtop centrifuge, centrifuged at 30 *g* for 3 min. Myocytes were resuspended in stop buffer containing 100 mM $CaCl_2$, allowed to rest for 2 min, and then centrifuged at 30 *g* for 3 min. These steps were repeated using stop buffer with increasing $CaCl_2$ concentrations until 1 mM was achieved.

After isolation, experiments were performed with freshly isolated myocytes resuspended in a HEPES-buffered solution containing (in mM): 1 $CaCl_2$, 137

NaCl, 5.4 KCl, 15 dextrose, 1.3 $MgSO_4$, 1.2 NaH_2PO_4, and 20 HEPES (pH 7.4).

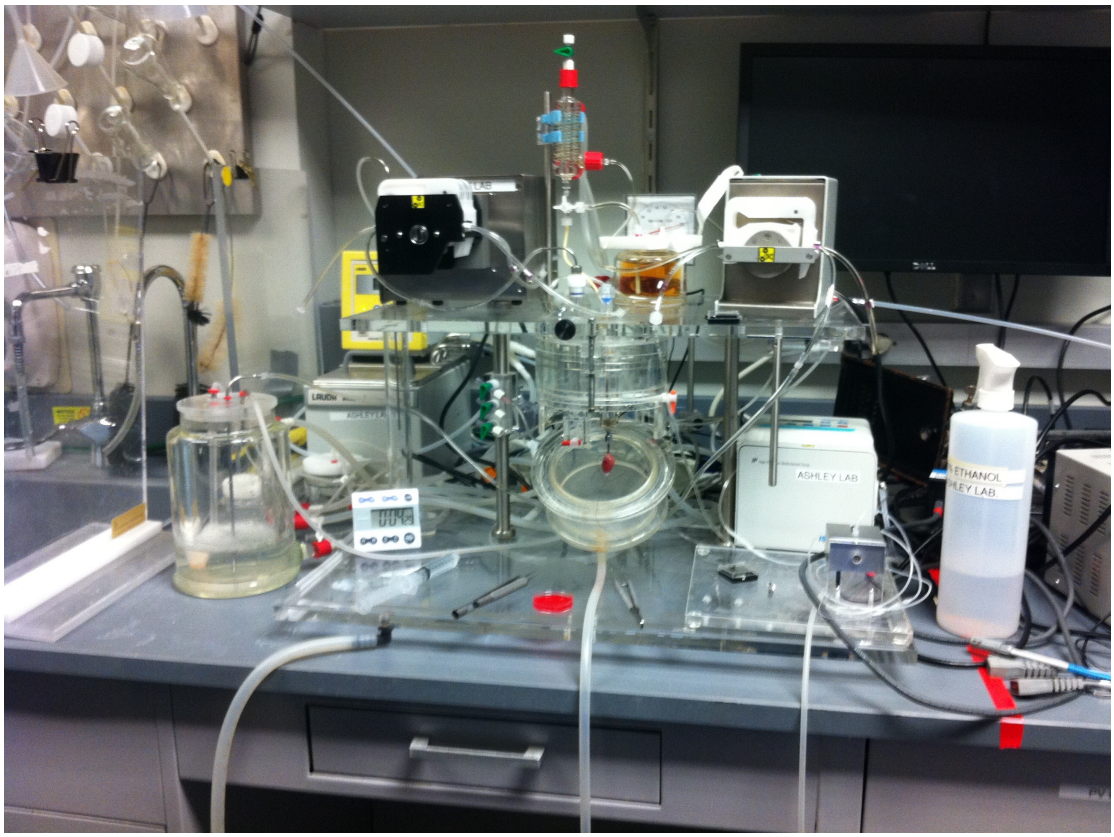

FIGURE 2-7 - LANGENDORFF APPARATUS FOR COLLAGENASE DIGESTION AND MYOCYTE ISOLATION

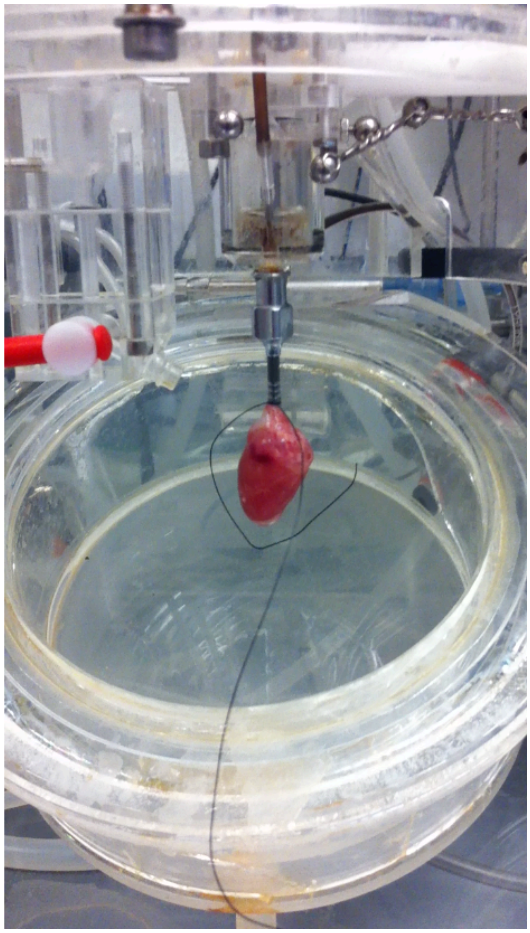

FIGURE 2-8 – CLOSE UP OF HEART ATTACHED TO LANGENDORFF

2.7. Myocyte unloaded shortening and relaxation.

Cell contraction properties of myocytes were evaluated with a video-based sarcomere spacing acquisition system (SarcLen; IonOptix, Milton, MA) as previously described.[58] Rod-shaped ventricular cardiomyocytes with clear striation patterns that were quiescent when un-stimulated, but robustly and symmetrically twitching to field stimulation, were chosen. These cells were placed in a culture chamber stimulation system (Cell MicroControls, Norfolk, VA), mounted on an inverted microscope (Nikon TE2000U; Nikon, Melville, NY), and electrically stimulated with suprathreshold voltage at frequencies

as specified in experiments. Changes in sarcomere length were recorded, and further analysis was performed using IonWizard software (IonOptix).

2.8. Calcium transient measurements

Ventricular myocytes were loaded with 0.2 μM of Fluo-5f-acetoxymethyl ester (Molecular Probes, Eugene, OR) for 30 min, and then allowed to incubate in dye free HEPES-buffered saline for additional 30 min to allow for de-esterification of the calcium dye. Myocytes were electrically field stimulated at a frequency specified in experiments. Cells were excited and spatially averaged calcium transients were measured using a standard FITC cube (Chroma) using the HyperSwitch system (IonOptix). The fluorescence transients were normalized to ΔF/F units and characterized according to the following parameters as previously described[59]: $(\Delta F/F)_{peak}$; time to peak (t_p was measured from the initiation of the rising phase of the transient), delay to baseline (t_d measured from the $(\Delta F/F)_{peak}$ to 90% of the return to baseline). The dye was assumed to be at near equilibrium with the calcium transient.

2.9. Two-Carbon Fiber Technique

Cells were isolated, prepared, and mounted on the inverted microscope similar to above. A pair of micro-carbon fibers, each attached to miniature hydraulic manipulators (SM-28, Narishige, Tokoyo, Japan) and computer-controlled with a piezoelectric translator (P-621.1CL, Physik Instruments, Karlsruhe/Palmbach, Germany) mounted on a custom made railing system (IonOptix, Milton, Mass), were attached to single isolated ventricular

myocytes robustly twitching in response to field stimulation (IonOptix, Milton, Mass). Figure 2.9 below shows the setup of the equipment. Cells were stretched axially by the piezoelectric translator movement of the carbon fibers using custom software (Matlab, courtesy of Mr. P Lee). Sarcomere length changes were confirmed via fast Fourier transformation of sarcomere banding (SarcLen; IonOptix Milton, MA). Carbon fiber bending was measured (IonOptix, Milton, Mass) and force was calculated as by using the following formula:

$$F = K(\Delta L_F - \Delta L_P)$$

Where ΔL_F is the change in distance between the two carbon fiber tips that are attached to the cell, and ΔL_P is the change in distance between the two piezoelectric translators to which the carbon fibers holders are mounted. K is the stiffness of the carbon fiber (0.15-0.25 $\mu N \cdot \mu m^{-1}$).[60] Individual diastolic and systolic cell results were plotted and fitted using a linear regression model (Origin, Northhampton, MA) to give both end-systolic and end-diastolic length-tension relationships (ESLTR and EDLTR, respectively). Data were normalised to the starting systolic force or as the Frank-Starling gain to eliminate the spring constant.[61]

FIGURE 2-9- INVERTED MICROSCOPE WITH A PIEZOELECTRIC TRANSLATOR MOUNTED ON A CUSTOM MADE RAILING SYSTEM

2.10. Western blotting

Left ventricles were homogenized over ice in mannitol-sucrose lysis buffer containing 1:300 dilutions of phosphatase inhibitor/protease inhibitor

cocktails 2 and 3 (Sigma-Aldrich) and 1% Triton-X v/v. Protein content was quantified using a Bradford assay (Bio-Rad). Protein separation was done in 10% SDS-PAGE gels transferred to Immobilon-P (Millipore). Blots were probed respectively with 1:1000 CAMKII G69 clone (Milllipore), 1:500 Phospho-CAMKII (Cell Signaling), and 1:1000 sarcomeric actin (Sigma-Aldrich). All secondary antibodies (anti-mouse HRP and anti-rabbit HRP) were obtained from GE Amersham. CAMKII and phospho-CAMKII were visualised using SuperSignal femto-ECL (Pierce). Sarcomeric actin was visualised using Amersham ECL. Image capture was made with Bio-RAD ChemiDoc XRS imaging. Quantification of densitometry was done with ImageJ v1.46n.

2.11. In Situ Optical Mapping of Voltage and Calcium in the Heart

In an attempt to visualize CICR in-vivo and map the voltage, we made the following imaging system. Our system as shown in the schematic below (figure 2.10) was constructed from readily-available optical filters, lenses, LEDs, electronics, and a single high-speed, electron-multiplied charge-coupled-device (EMCCD) camera (Photo-metrics, Tucson, AZ, USA).

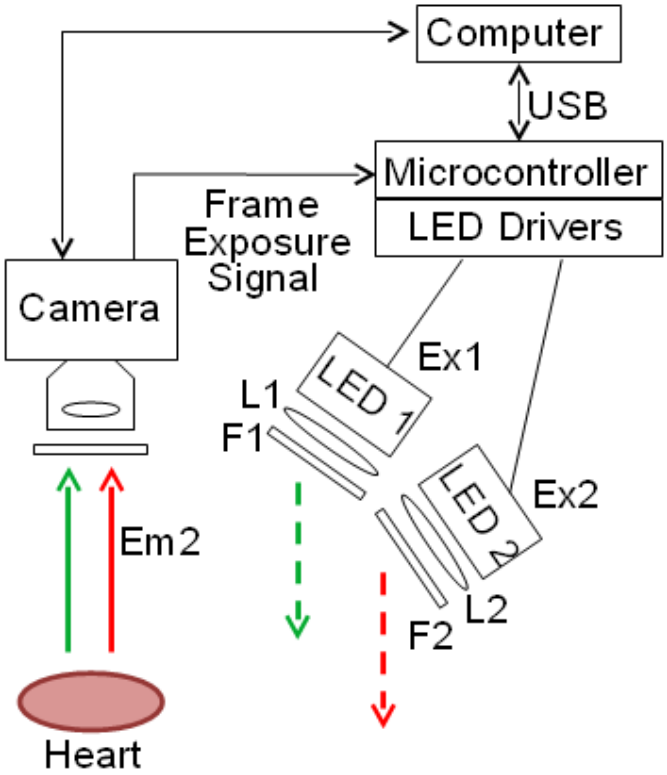

FIGURE 2-10 - SCHEMATIC OUTLINE OF THE IMAGING SYSTEM, HIGHLIGHTING KEY COMPONENTS. SINCE ONLY ONE CAMERA IS USED, THE SYSTEM REQUIRES NO CHALLENGING OPTICAL ALIGNMENT. EXCITATION SOURCES EX1: RED LED WITH A 640610 NM FILTER (F1), EX2: GREEN LED WITH A 540612.5 NM FILTER (F2).

We measured V_m using di-4- ANBDQPQ (Berlin Center for Cell Analysis and Modelling, University of Connecticut, USA) and $[Ca^{2+}]_i$ using rhod-2(AM) (Molecular Probes, Eugene, OR, USA). Di-4-ANBDQPQ was excited with Ex1: LED CBT-90-R (peak power output 32 W; peak wavelength 628 nm; Luminus Devices, Billerica, MA, USA) using excitation filter D640/206 (Chroma Technology, Bellows Falls, VT, USA). Rhod-2(AM) was excited with Ex2: LED CBT-90-G (peak power output 58 W; peak wavelength 524 nm; Luminus Devices) with excitation filter D540/256 (Chroma Technology). Light from the LEDs was collimated with plano-convex lenses (LA1951; Thorlabs, Newton, NJ, USA). Fluorescence emission from dye-loaded hearts was passed through custom-made multi-band emission filter F3, available

from Chroma (ET585/50-800/ 200 m; Chroma Technology), with high-percentage transmission spectra for both emission bands (~560–610 nm and ≥700 nm), and collected with a fast camera-suitable lens (f/# 0.95; DO-2595; Navitar). Fluorescence images were taken with a high-speed EMCCD camera (CascadeH 128+ or Evolve^{TM} 128, Photometrics) running at 510 (Cascade) or 530 (Evolve) frames-per-second (both at 128 X 128 pixels). Figure 2.11 shows the experimental setup with the camera in place over the heart.

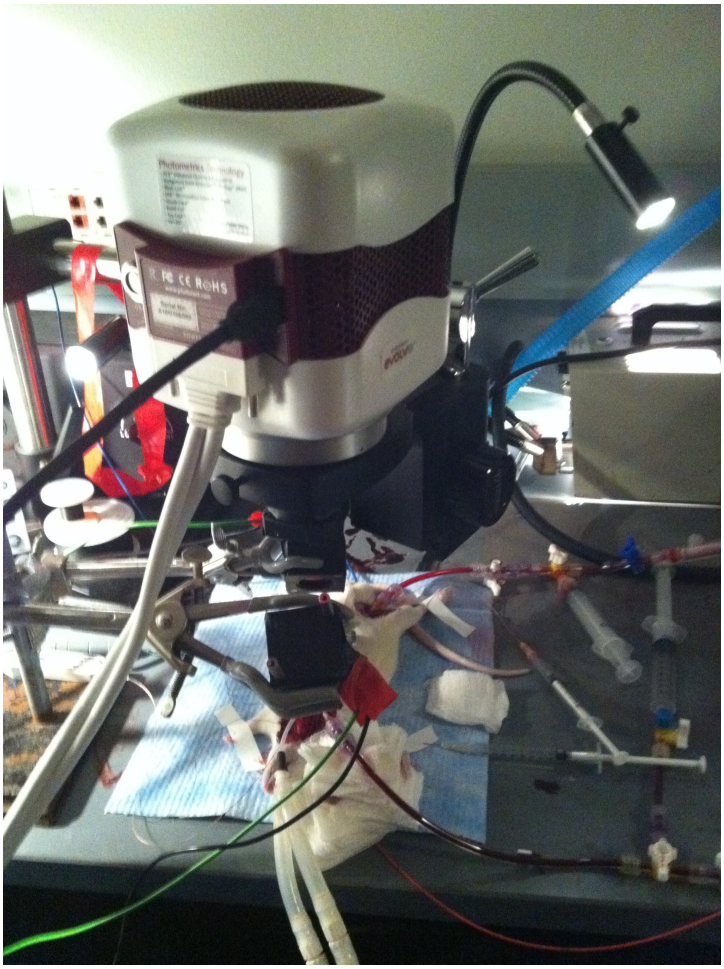

FIGURE 2-11 - EVOLVE (PHOTOMETRIC) CAMERA SHOWN IN THE EXPERIMENTAL SET UP, OVER THE RAT THAT IS ON ECMO

A microcontroller-based interface was implemented (figure 2.12) to synchronise excitation light switching with EMCCD camera frame exposure

periods (in our experiments, the camera ran off its internal clock; i.e. the camera was master and the LEDs were slaves). LEDs were controlled with a custom-built high-power LED driver circuit that enables illumination power to be tuned, and light output to be switched in the kHz range. An eight processor microcontroller (Propeller chip; Parallax, Rocklin, CA, USA) was used to control and coordinate all major components of the set-up. Control software for time-critical tasks was written in the microcontroller's assembly language, to ensure a time resolution of 50 ns. Communication with a standard desktop computer was implemented via a USB interface module (UM245R; Future Technology Devices International, Glasgow, UK). Custom software, written in MATLAB (The MathWorks, Natick, MA) was used to design experiments, to communicate with the microcontroller, and to perform optical mapping image processing. All electronic components used to build the micro-controller-based interface were acquired from major electronic components distributors (e.g. Digi-Key, Thief River Falls, MN, USA).

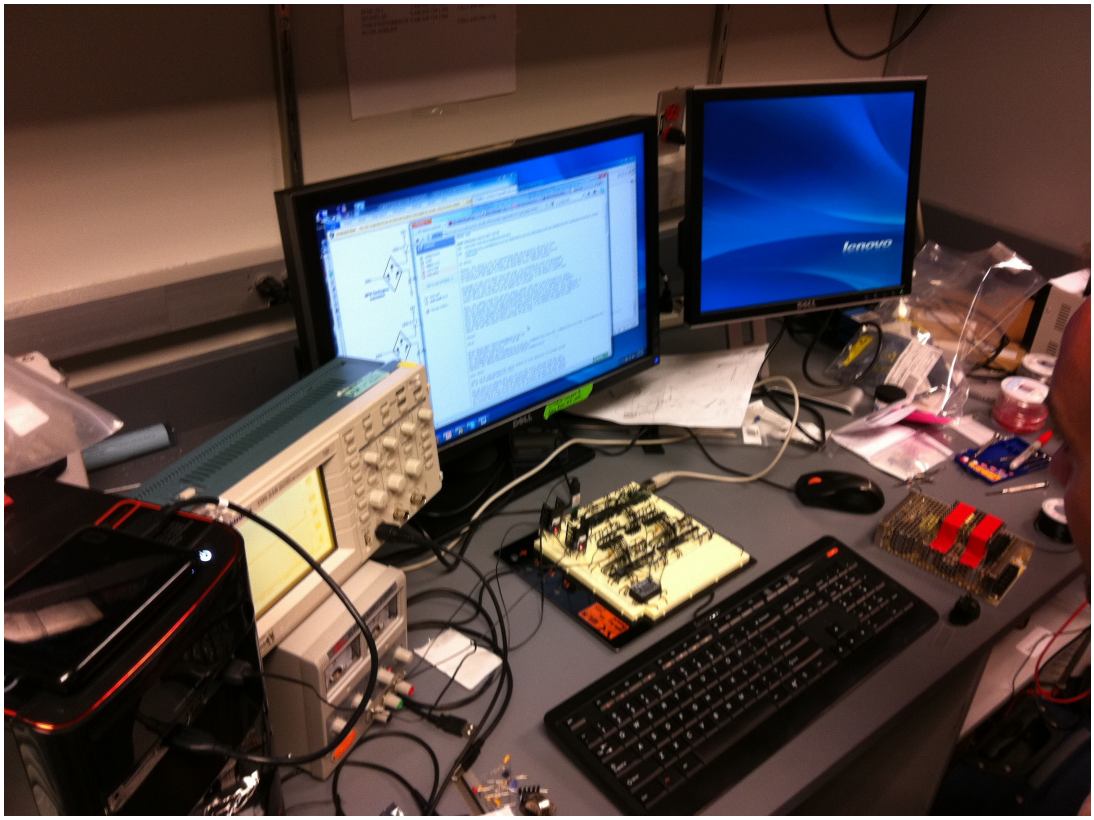

FIGURE 2-12– MICROCONTROLLER, COMPUTER RUNNING MATLAB, LED DRIVER CIRCUIT

Male Sprague-Dawley rats (250–300g) were anesthetised with 1–2% isoflurane in oxygen as described before. Rats were maintained at 37^{o}C and depth of anesthesia was monitored throughout according to standard protocols (APLAC, Stanford University). Tracheotomy was established with a 14-gauge cannula and the animal was ventilated at a pressure support of 15 mmHg at 60 breaths per minute (Kent Scientific, San Diego, CA, USA). A standard sternotomy was then performed. The right femoral artery (FA), external jugular vein (EJV), and ascending aorta (AA), via the carotid artery (CA), were cannulated with polyethylene tubing. Heparin (1,000 units/kg, Sigma-Aldrich) was administered intra-venously. A 1.4 Fr conductance catheter (Millar Instruments, Houston, Texas, USA) was introduced via the esophagus to provide an ECG lead. Blood pressure was monitored with a

pressure transducer (Hugo Sachs Electrical, March- Hugstetten, Germany) attached to the side-port of the FA cannula. For experiments with ventricular pacing, a pacing stimulator (Millar Instruments) was placed on the left ventricular epicardial apex. Dyes were loaded by direct aortic root injection, during loading of voltage dye di-4-ANBDQPQ we found no appreciable differences in these ECG traces or MAP. Rhod-2(AM) loading required ECMO support, as the $[Ca^{2+}]_i$ dye could lead to asystolic arrest during initial injection, with subsequent beating recoverable with circulatory support (which was always needed for calcium dye experiments). For select experiments as specified in the result, an ECMO circuit was used to maintain a mean coronary perfusion pressure of 60 mmHg (figure 2.13A). The ECMO circuit as described in detail above involved a micro-peristaltic pump (Digital Reglo Pump Model 1329, Ismatec Ltd., Wertheim- Mondfeld, Germany), in line with the tubing and a miniature membrane oxygenator (Living Systems Inc St. Albans, Vermont, USA), and in parallel to a venous reservoir. The circuit was primed with 5 mL of heparinised saline (20 units/mL) to remove all air. The ECMO circuit was attached in series to the EJV and FA, and run in a retrograde manner when used.

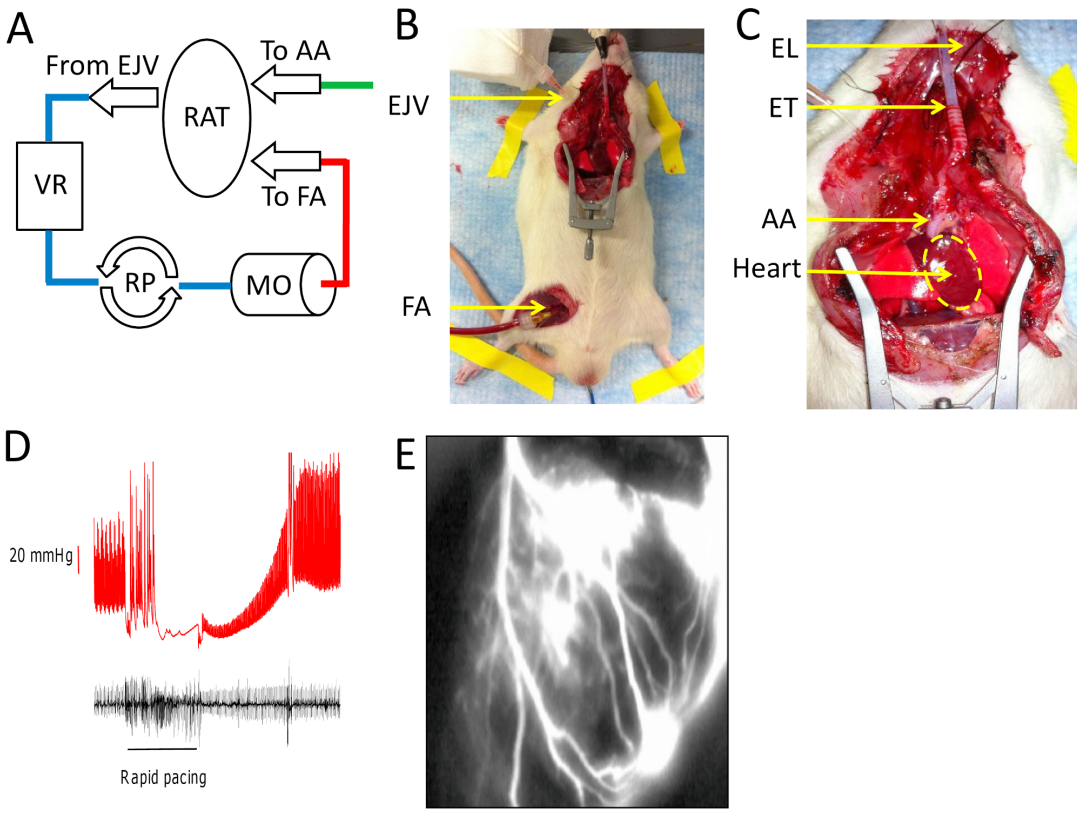

FIGURE 2-13 - (A) A SCHEMATIC OF THE RAT ECMO CIRCUIT BASED ON A STANDARD PUMP CIRCUIT (EJV: RIGHT EXTERNAL JUGULAR VEIN CATHETER, VR: VENOUS RESERVOIR, RP: ROLLER PUMP, MO: MINIATURE MEMBRANE OXYGENATOR, FA: RIGHT FEMORAL ARTERY CATHETER, AA: ASCENDING AORTA CATHETER VIA RIGHT CAROTID ARTERY). IN CARDIOPULMONARY BYPASS (CPB) MODE, BLOOD IS PUMPED FROM THE EJV THROUGH THE MO TO THE FA, DEPICTED BY ARROWS IN THE FIGURE. DYE IS INJECTED THROUGH THE AA CATHETER. (B) WHOLE-ANIMAL VIEW OF THE PREPARATION. (C) ZOOMED-IN VIEW OF THE OPEN CHEST, WITH THE HEART IN CLEAR VIEW (EL: ESOPHAGEAL ECG LEAD, ET: ENDOTRACHEAL TUBE). (D) AN EXAMPLE OF RVP AT 12 HZ TO DROP BLOOD PRESSURE (BP; RED TRACE), AFTER WHICH DYE WAS INJECTED VIA THE AORTIC ROOT. THE BP RECOVERED SOON AFTER CESSATION OF PACING. IMMEDIATELY AFTER LOADING AS SHOWN HERE, THE BP INCREASED REFLECTING THE FRANK-STARLING EFFECT OF PROLONGED LOADING. THE ACCOMPANYING ECG (BLACK TRACE) IS ALSO SHOWN. (E) ZOOMED-IN VIEW OF THE HEART IMMEDIATELY AFTER RHOD-2(AM) INJECTION DEMONSTRATING A FLUORESCENT CORONARY ANGIOGRAM.

Figures 2.13B and 2.13C show photographs of the imaging camera view of the preparation. Traditional coronary catheterisation has already been employed to load voltage dyes in larger animals without complications,[51] but was impractical in the rat. Therefore, dyes were injected into the ascending aorta via the carotid artery and towards the coronary circulation. To accomplish this, blood pressure had to be reduced to allow sufficient

coronary perfusion with the dyes. As shown in Figure 2.13D and 2.13E, blood pressure was reduced through combination of rapid ventricular pacing (RVP, 12 Hz) to impair ventricular diastolic filling, thereby reducing stroke volume sufficiently to decrease arterial blood pressure, similarly to what is done clinically during stent-valve implantation.[62] Once blood pressure was reduced sufficiently to decrease resistance to injection (Figure 2.13D), the aorta was temporarily cross-clamped, and dye was injected through the carotid artery catheter, mimicking the clinical aortic root injections of contrast agents.[62] Figure 2.13E shows a still image during dye loading (rapidly thereafter the dye leaves the vascular space because of its amphiphilic properties). We found that RVP and cross-clamp periods not exceeding 10 seconds were sufficient to permit dye loading through the coronary circulation. Blebbistatin was added to the circulation during final imaging to reduce wall motion.[63] When blebbistatin was used, cardiopulmonary bypass was used to preserve coronary perfusion.

2.12. Image processing

Custom MATLAB software was used to perform optical map image processing. Signals were filtered (in time) with local regression using weighted linear least squares and a 1st degree polynomial model (MATLAB's built-in smooth function) and images were filtered using 2D median filtering (MATLAB's built-in medfilt2 function).

2.13. Statistics

Pairwise comparisons were made using Student's t-test. One-way ANOVA was used in the event of multiple groups. Post hoc testing was carried out according to the method of Bonferroni. Exact P values are stated in most cases. All data is presented in the text as mean ± standard error of the mean.

CHAPTER 3.RESULTS

3.1. RODENT MODEL OF DONATION AFTER CIRCULATORY DEATH

Using the miniature ECMO circuit for reperfusion of the DCD heart, cardiac function was evaluated after reperfusion of the rat heart following circulatory arrest and warm ischemia. In human DCDs inotropic and ventilatory support are withdrawn. Cardiac arrest subsequently occurs due to asphyxiation and hypoxia after the donor is extubated. In order to simulate the hypoxic injury that produces cardiac arrest in the human DCD, the trachea was clamped in the rat model to produce asphyxiation and cardiac arrest. Tracheal occlusion was followed by progressive hypotension and bradycardia. This preceded cardiac arrest which occurred 5.4 +/- 2.8 minutes after tracheal occlusion. Following circulatory arrest and 15 minutes of warm ischemia the animal was reperfused with normothermic oxygenated blood using a miniature ECMO circuit. Reperfusion led to recovery of cardiac function with re-establishment of normal cardiac rhythm. After 30 minutes of reperfusion, the supportive extracorporeal circulation was weaned to allow the resuscitated heart to independently support the animal's circulation. Schematic of our ECMO circuit are depicted in figure 3.1.

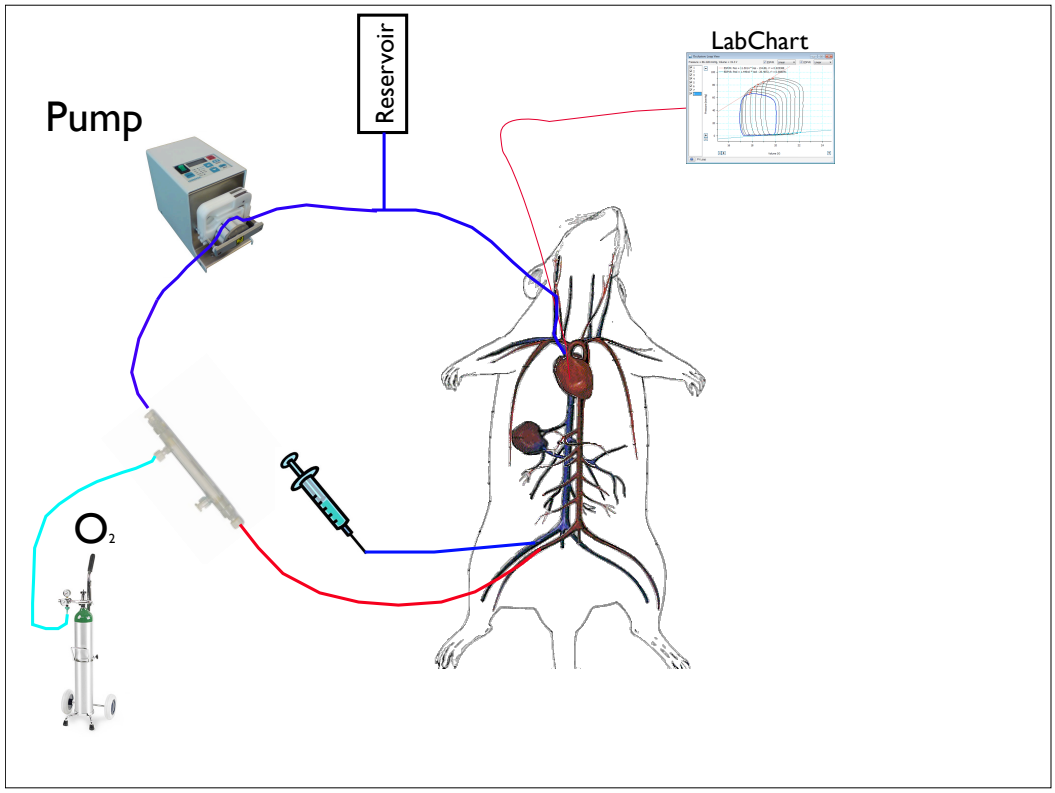

FIGURE 3-1 – MINIATURE ECMO CIRCUIT

Haemodynamic changes observed in the rat DCD are shown in figure 3.2

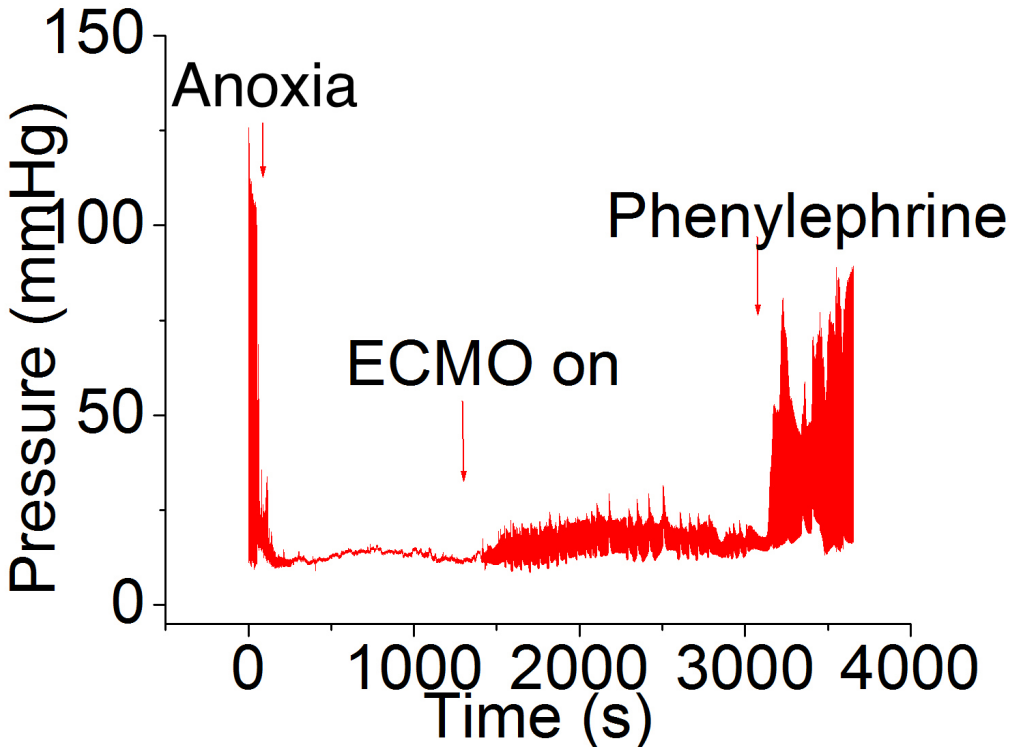

FIGURE 3-2 – ARTERIAL BLOOD PRESSURE CHANGES FOLLOWING CARDIAC ARREST AND THEN REPERFUSION WITH ECMO

3.2. RODENT MODEL OF DONATION AFTER BRAIN-STEM DEATH

Subdural balloon inflation was followed by a hyperdynamic response with marked hypertension and tachycardia, leading to a rise in ICP with consequent coning and transtentorial herniation of the brain-stem. The hemodynamic response to BSD is depicted in figure 3.3.

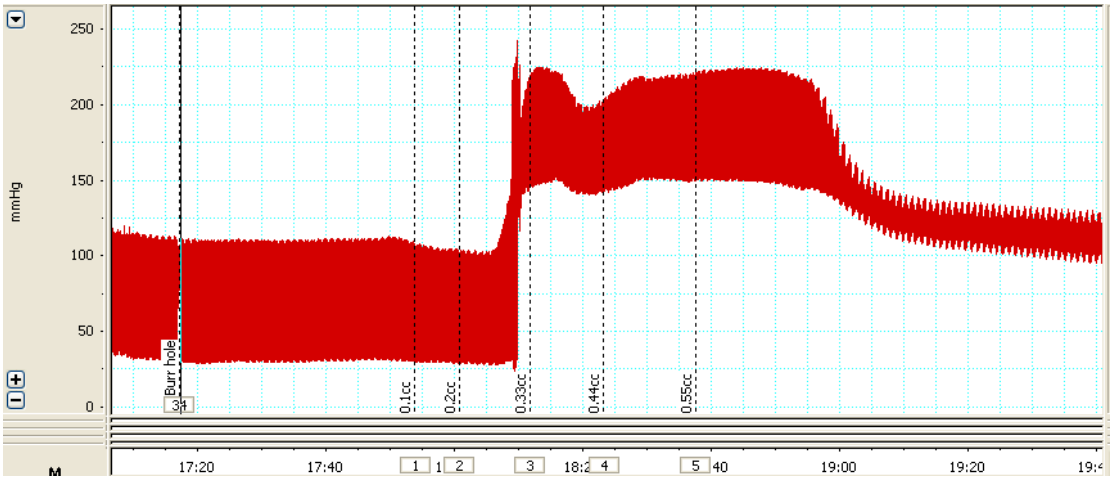

FIGURE 3-3 – BLOOD PRESSURE CHANGES DURING SUBDURAL BALLOON INFLATION AND BSD

With balloon inflation there was a sharp rise in arterial blood pressure with peak systolic pressures nearing 250 mmHg. This hypertensive crisis was then followed by a gradual decline in blood pressure back towards base line. In 3 rats this decline didn't stop and blood pressure fell to zero within 5 minutes.

In the rats that survived, data was collected at 2 hours after balloon inflation. Hypertension following balloon inflation was accompanied with an average rise in heart rate of almost 50 bpm. The hemodynamic response to BSD is secondary to a dramatic increase in circulating plasma catecholamines.[64] Exposure of the heart to markedly elevated catecholamine concentrations has been associated with cardiac dysfunction and a decline in hemodynamic performance.[65] There is uncertainty as to whether the cardiac dysfunction observed after BSD is due to primary impairment of LV contractility or secondary to abnormal loading conditions of the heart.[66,67]

3.3. PV analysis of DCD vs DBD

Pressure volume hemodynamic measurements were taken from both LV and RV before and after cardiac arrest and after DBD, representative PV loops are shown in figures 3.4 A-C and 3.5 A-C. The LV and RV measurements were not necessarily taken from the same animal. LV comprised of 16 control, 5 DBD & 7 DCD, RV comprised of 11 control, 12 DBD & 14 DCD. The data is shown in figure 3.6 below.

EDPVR exponentials did not well fit the data in the post-arrest samples therefore Tau(τ) was used to describe the lusitropic properties of the hearts. Analysis showed no significant change between the control group and DBD group when looking at ESPVR, PRSW and Tau. However, when looking at the measure of Contractility Index there was an increase in the DBD group. The DBD experiment was difficult to replicate. Many of the experiments failed after inducing brain death due to the animal not surviving the insult, while the ones that did survive may not have had a sufficient insult and therefore the increase in CI may be a result of increased circulating catacolamines with their adrenergic effects. There was, however, a significant decrement in contraction and relaxation following DCD (ESPVR -44%; CI-48%; PRSW -31%; τ +500%). Together, these data demonstrate the phenomenon of post cardiac arrest myocardial dysfunction (PMAD) following DCD. There was no difference seen when directly comparing changes in LV and RV function between control/DBD/DCD, this was reassuring to see as LV and RV have different embryological origins and often the first sign of organ failure post transplantation is RV dysfunction.

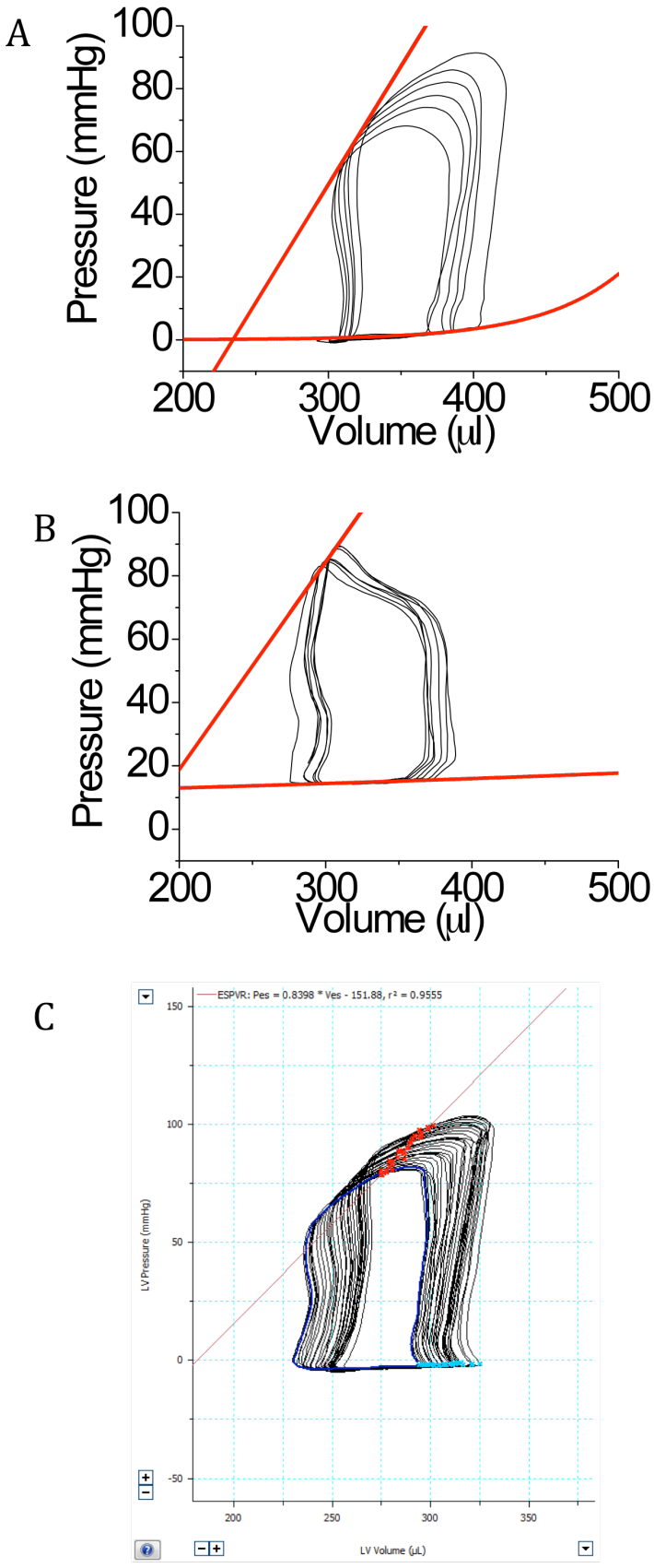

FIGURE 3-4 - REPRESENTATIVE PV LOOPS FROM THE LEFT VENTRICLE: A – CONTROL, B – DCD & C DBD. RED LINES DEMONSTRATING ESPVR AND EDPVR

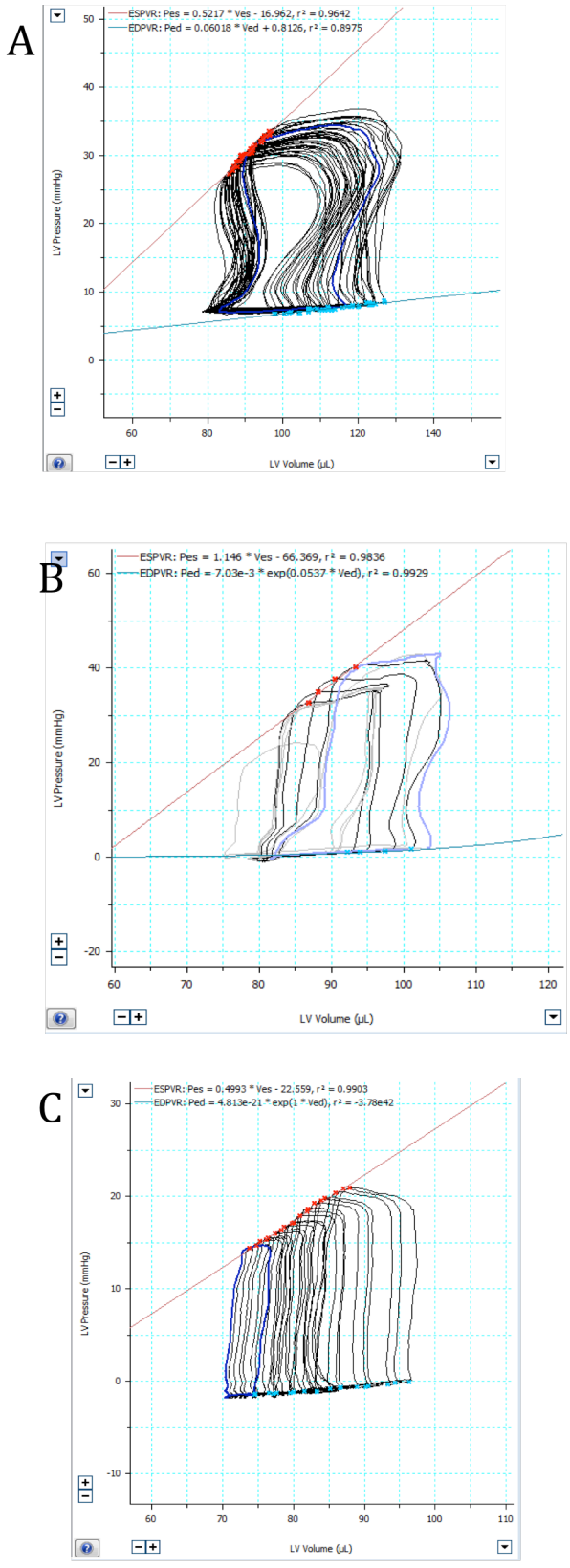

FIGURE 3-5 – REPRESENTATIVE PV LOOPS FROM THE RIGHT VENTRICLE: A – CONTROL, B – DCD & C DBD. RED LINES DEMONSTRATING ESPVR AND BLUE LINE EDPVR

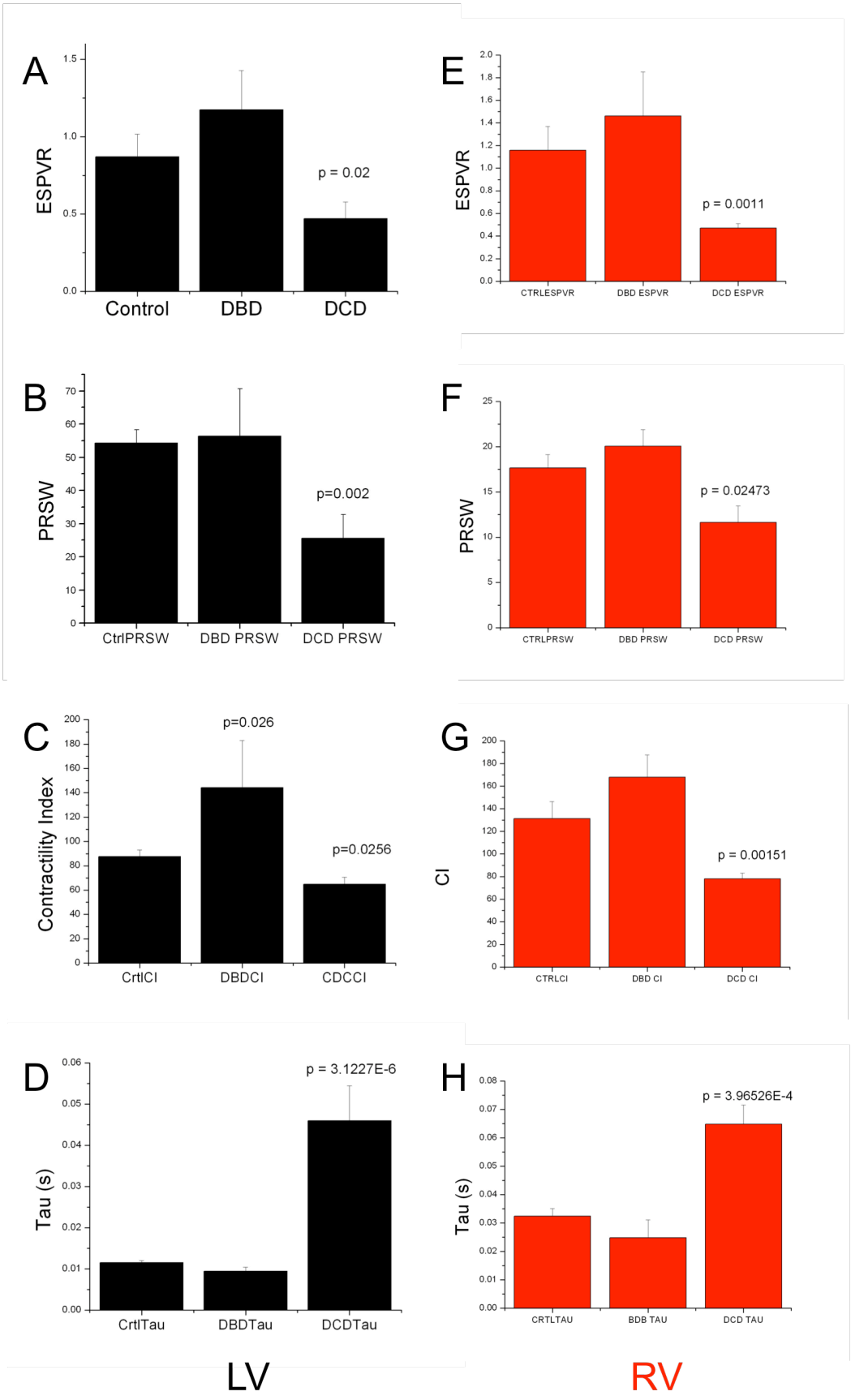

FIGURE 3-6 – SUMMARY DATA FOR BOTH LV(A-D IN BLACK) AND RV(E-H IN RED). A, SUMMARY DATA FOR LV ESPVR FOR CONTROL, DBD AND DCD. B, SUMMARY DATA FOR LV PRSW FOR CONTROL, DBD AND DCD. C, LV SUMMARY DATA FOR CI (MMHG/µL)*S FOR

CONTROL, DBD AND DCD. D, SUMMARY DATA FOR LV TAU FOR CONTROL, DBD AND DCD. E, SUMMARY DATA FOR RV ESPVR FOR CONTROL, DBD AND DCD. F, SUMMARY DATA FOR RV PRSW FOR CONTROL, DBD AND DCD. G, RV SUMMARY DATA FOR CI (MMHG/µL)*S FOR CONTROL, DBD AND DCD. H, SUMMARY DATA FOR RV TAU FOR CONTROL, DBD AND DCD. *P* VALUES IN GRAPHS ARE WITH RESPECT TO CONTROL USING POST HOC ANALYSIS. LV: CONTROL N=16, DBD N=5 & DCD N=7. RV: CONTROL N=11, DBD N=12 & DCD N=14

3.4. Cellular Contractility in Post-myocardial arrest dysfunction

To investigate cell function directly, we first examined unloaded sarcomere shortening (%SL) in isolated adult cells from LV control and PMAD hearts. In cells paced at 1 Hz steady state, the %SL for control and PMAD cells was 13±0.3 vs 10±0.7, a 23% decrease in the %SL in unloaded cells ($p=3e^{-4}$, n=142 cells from 12 animals and 186 cells from 10 animals for control and PMAD, respectively). Likewise, we found that the peak velocity of contraction (v_c) was 4.3±0.2 vs 2.6±0.1 while the peak velocity of relaxation (v_r) was 2.5±0.1 vs 2.0±0.1 1 µ/ms in control vs PMAD cells (same n as above, p=2e-14, p=5.2e-4; data not shown).

To validate the unloaded shortening data, and provide further insights into contractile dysfunction in PMAD, we investigated single cell force and contractility in PMAD and control left ventricular cells using the two-carbon fiber stretch technique.[60] Figure 3.7 A shows a single isolated adult left ventricular myocyte before and after a twitch in response to electrical stimulation, showing the carbon fiber bending. Figure 3.7 B shows the stepwise stretch protocol, the cellular Frank-Starling effect. Figure 3.7 C shows carbon fiber bending for the same stretched cell which is proportional to force.[60] Corresponding to the derivation by regression of load 'independent' values *in vivo*, the ESTLR and EDTLR are defined in single cells as the slopes of the linear regressions of systolic and diastolic force

plotted against sarcomere length obtained from plots shown in Figure 3.7 B,C. These two relationships are shown in Figure 3.7 D for the control fiber from Figures 3.7 B and C. These experiments were repeated in cells from PMAD animals (Figure 3.7 E). We found both the ESLTR and EDLTR to be depressed in the PMAD cells. In Table 3.1, pooled analysis of the slopes of the ESTLR and EDTLR for both control and PMAD cells are shown. For this pooled analysis, all ES and ED force measurements were normalized to the baseline (un-stretched) systolic force in order to remove any effect of variability in carbon fiber stiffness (variability in spring constant), and then linearly fit. As illustrated in Table 3.1, the ESLTR and EDLTR were 60% and 36% depressed in PMAD cells, respectively, compared with that of controls ($p<0.05$). In addition, we calculated the Frank-Starling gain by dividing the active force by the passive force at each stretched length, also a dimensionless index which describes PRSW at the single cell level. [61] In Figure 3.7 F, we therefore plot $PRSW_{cell}$ vs $afterload_{cell}$. As can be appreciated, this cellular data recapitulates length-tension curves obtain with PV loops, and suggests that contractility is significantly depressed in PMAD. Figure 3.7 G shows the active force frequency relationship (FFR) for both control and PMAD cells under no passive stretch (baseline sarcomere length) as measured by carbon fiber bending with twitch, demonstrating that the FFR is depressed in PMAD cells at all frequencies investigated.

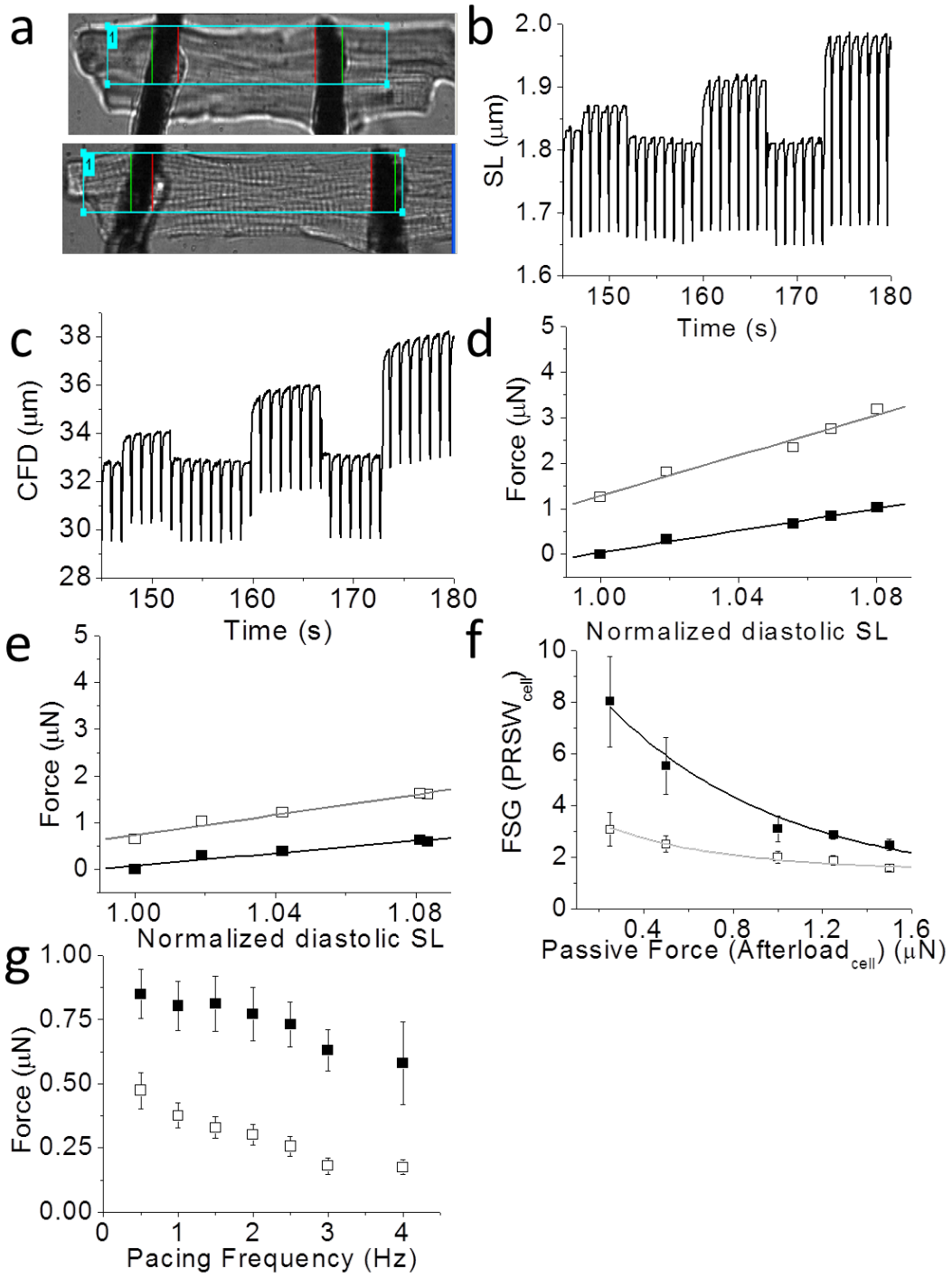

FIGURE 3-7 - IN VIVO AND ISOLATED CELL LOAD DEPENDENT PARAMETERS IN CONTROL AND CARDIAC ARREST. A. ISOLATED TWITCHING MYOCYTE (CONTRACTED STATE) BEFORE (TOP) AND DURING TWITCH IN RESPONSE TO ELECTRICAL ACTIVATION DEMONSTRATING CARBON FIBER BENDING. B THE SARCOMERE LENGTH (μM) IN RESPONSE TO 1 HZ PACING VS TIME AS CF STRETCH IS APPLIED TO THREE DIFFERENT ENDPOINT LENGTHS DEMONSTRATES THE CELLULAR FRANK-STARLING EFFECT. BETWEEN EACH STEP, THE CFS ARE RETURNED TO BASELINE. EACH STRETCH PRODUCES INCREASED SARCOMERE LENGTH CHANGE. C. CARBON FIBER BENDING (CFB) (PROPORTIONAL TO FORCE) VS TIME DEMONSTRATING THE INCREASE IN BOTH DIASTOLIC (PASSIVE) AND SYSTOLIC (ACTIVE) SINGLE CELL FORCE, RESPECTIVELY. D. STRETCH INDUCED PEAK SYSTOLIC (OPEN SQUARES) AND BASELINE DIASTOLIC (FILLED SQUARES) TENSION FROM A CONTROL CELL. THE LINEAR FITS TO THE

DATA REPRESENT THE EDLTR (BLACK LINE) AND ESLTR (GRAY LINE). IN THIS CASE, THE ESLTR WAS 22 µN/µM (R^2=0.96), AND THE EDLTR WAS 6.6 µN/µM (R^2=0.95). E. STRETCH INDUCED PEAK SYSTOLIC (OPEN SQUARES) AND BASELINE DIASTOLIC (FILLED SQUARES) TENSION FROM A PMAD CELL. IN THIS CASE, THE ESLTR WAS 11 µN/µM (R^2=0.92), AND THE EDLTR WAS 6 µN/µM (R^2=0.98). F. $PRSW_{CELL}$ VS $AFTERLOAD_{CELL}$ FORCE FOR CONTROL (OPEN SQUARES) AND PMAD (FILLED SQUARES), N= 8 CELLS FROM 3 HEARTS AND 8 CELLS FROM 2 HEARTS FOR CONTROL AND PMAD, RESPECTIVELY. EXPONENTIAL FITS TO THE DATA WERE DONE USING THE EQUATION FSG= Y0+A1E^(-X/T1). FOR CONTROL AND PMAD, RESPECTIVELY, Y0, A1, T1 WERE: 0.94 AND 1.47, 9.5 AND 2.7, 0.78 S AND 0.54 S. R^2 WERE 0.96 AND 0.92. N= 8 CELLS FROM 3 HEARTS AND 8 CELLS FROM 2 HEARTS FOR CONTROL AND PMAD, RESPECTIVELY. G. FORCE FREQUENCY RELATIONSHIP (FFR) FOR POOLED BSF (µM) VS PACING FREQUENCY FOR CONTROL (BLACK SQUARES) AND PMAD (OPEN SQUARES) PLOTTED WITH SE, N= 8 CELLS FROM 3 HEARTS AND 8 CELLS FROM 2 HEARTS FOR CONTROL AND PMAD, RESPECTIVELY.

Table 3.1 – In Vivo and Isolated Cell

	Control	PMAD (P Value)
ESPVR (mmHg/µl)	1.0±0.10	0.5±0.1 (0.02)
PRSW (mmHg)	58±8	30±6 (0.02)
CI (mmHg/µl)*s	93±6	64±6 (0.005)
τ (ms)	12±3	45±6 (7e-11)
ESLTR (au)	84±11	34±6 (0.04)
EDLTR (au)	44±6	28±6 (0.02)
Peak PRSWcell (au)	8±2	3.0±1 (0.006)

TABLE 3. 1 - IN VIVO AND ISOLATED CELL PARAMETERS: AU INDICATES ARBITRARY UNITS; CI, CONTRACTILITY INDEX; EDLTR, END- DIASTOLIC LENGTH-TENSION RELATIONSHIP; ESLTR, END-SYSTOLIC LENGTH-TENSION RELATIONSHIP; ESPVR, END-SYSTOLIC PRESSURE-VOLUME RELATIONSHIP; PMAD, POST–MYOCARDIAL ARREST DYSFUNCTION; PRSW, PRELOAD RECRUITABLE STROKE WORK; AND T, ISOVOLUMIC RELAXATION CONSTANT. CONTROL N=136 CELLS FROM 11 ANIMALS, PMAD N=164 CELLS FROM 12 ANIMALS.

3.5. Calcium induced calcium release

Previous reports examining ischemia–reperfusion using higher affinity calcium indicators[37] have found little change in calcium induced calcium release. Here, we used the lower affinity calcium indicator Fluo-5f because

rapid calcium transients are subject to dye kinetic filtering which can mask disease processes.[59] In Figure 3.8 A, a single sweep of a steady-state pacing train is shown for a PMAD and control cell. Consistent with an early report in post-ischemic myocardium,[41] we found that post arrest cells display markedly enhanced peak calcium transients. In pooled analysis, as shown in Figure 3.8 B, a significant 290% increased CICR amplitude was present. $\Delta F/F_{peak}$ from control (n=90 cells from 10 animals) and PMAD (n=123 cells from 12 animals) was 90±7 and 272±13, respectively (p=2e-29). We found no difference in the time to peak (t_p) of the calcium transient (52±4 and 46±10 ms, p=0.11, same n as above). The time to decay (t_d) of the CICR in PMAD was significantly prolonged (340± 9 *vs* 456± 9, p=4e-15), as was the time constant of decay (τ) (152±5 *vs* 216±7 ms, p=7e-10). Because this augmented CICR was present in isolated cells long after *in vivo* cardiac arrest, we labelled this as cardiac calcium "memory". This calcium cardiac memory was able to generate a spontaneous delayed increase in the calcium transient, the cellular surrogate of delayed after depolarisations as shown in Figure 3.8 C (top panel), and these delayed after depolarisations were capable of competing for the paced rhythm generating the cellular surrogate of triggered ventricular activity as well (Figure 3.8 C lower panel). Activity such as this was never seen in control cells.

To test whether higher affinity dyes used in prior experiments[32] might have masked these increases in CICR, we repeated experiments using a high affinity version calcium indicator, Fluo-4. We found that Fluo-4 filtered the signal substantially, dramatically reducing unloaded contractility and

minimizing the difference between control and post cardiac arrest (Figure 3.9).

3.6. Cardiac calcium memory is precipitated in vivo and mediated by catecholamines

In addition to the use of lower affinity calcium dyes, another important difference in the current report is our use of an *in vivo* model. We hypothesized that the neurohormonal axis may be important to ischemia reperfusion and to compare our data directly, we isolated cells from an ischemia-reperfusion Langendorff-preparation. We found that in isolated cells from these Langendorff "resuscitated" hearts sarcomeric shortening was minimally depressed and CICR was no different than controls (Figure 3.8 B, 15 minute arrest period).

We hypothesized that catecholaminergic activation was the key component promoting calcium cardiac memory *in vivo*. To test this possibility, in an otherwise stable ventilated animal, we infused epinephrine 23 μg/kg/min intravenously for 30 minutes. Infusion induced a typical adrenergic response and when turned off prior to cell isolation, the blood pressure and heart rate returned to normal (blood pH was also normal). We found a pronounced increase in CICR to a similar degree to that seen post cardiac arrest (Figures 3.8 A and B). Since it is hard to determine physiologically relevant doses and spectrum of adrenergic activators, we explored whether calcium cardiac memory resulted after brain-stem herniation, a state known to induce an endogenous catecholamine surge. Using a fogarty balloon inserted in the

cranial vault, we induced brainstem herniation, noted a similar dramatic heart rate and blood pressure response suggestive of adrenergic activation, and found a similar dramatic increase in the ΔF/Fpeak CICR of isolated cells (271 ± 21, n=110 cells from n=9 animals (p=2e-25 against control; Figure 3.8 B). We found no effect of beta-blocker administration (labetalol) on CICR augmentation despite a pronounced bradycardic response during administration.

3.7. Cardiac calcium memory is dependent on CAMKII and ryanodine but not PKA

A large increase in CICR in the face of reduced contractile function suggests a change in myofilament calcium sensitivity (Figure 3.8 F). In contrast, epinephrine directly added to the cell bath showed a marked increased contractile performance (%SL 20±0.5) associated with a more modest increase CICR (ΔF/F peak 141±0.53%). Since interplay between sub-acute and chronic beta-adrenergic signalling and CAMKII dependent pathways has been observed,[42,68,69] we tested whether CAMKII inhibition could block epinephrine infusion induced or PMAD induced calcium cardiac memory. As shown in Figure 3.8 B, we found that administration of the CAMKII inhibitor AIP was able to block the amplified CICR in both cases. We found that the lower affinity inhibitor KN93 was able to blunt calcium cardiac memory in PMAD (Figure 3.8 A, B), but not our arbitrary epinephrine infusion. Because CAMKII activation is in part activated by calcium dependent pathways, we tested whether specific inhibition of CICR during sudden cardiac arrest would blunt calcium cardiac memory. We found that for both epinephrine

infusion and PMAD, ryanodine too blocked the augmented CICR (Figure 3.8 B), suggesting that ryanodine receptor calcium release was crucial for this pathway. In contrast, and in agreement with our labetalol experiment, infusions of the PKA inhibitor H89 prior to induction of cardiac arrest did not prevent the increase in CICR (though this is a higher level than that seen for PMAD alone, we feel it is within the range seen for cardiac arrest for which a larger data set shows regression to the mean; Figure 3.8 B).

We measured both %SL (Figure 3.8 f) and force (Figure 3.8 g, h) in PMAD hearts exposed to either CAMKII inhibition with KN93 or with ryanodine during the initial cardiac arrest. We found that both %SL and baseline force were lower under these conditions, arguing that in these live cells, the augmented CICR acts to support contraction.

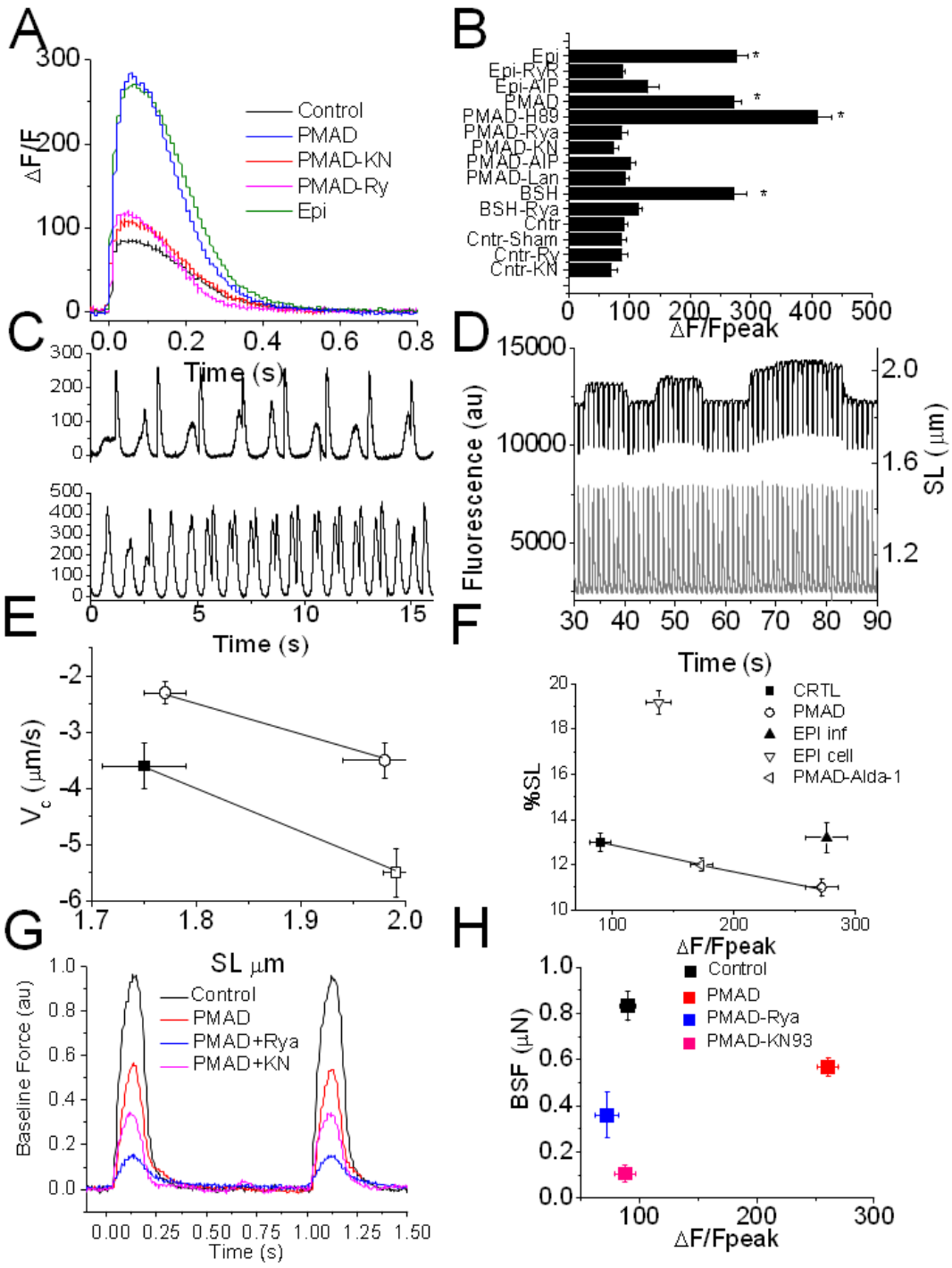

FIGURE 3-8 – CARDIAC CALCIUM MEMORY AFTER CARDIAC ARREST

A. EXAMPLE CICR TRANSIENTS MEASURED BY FLUO-5F IN CONTROL COMPARED AGAINST PMAD, AND ALSO PMAD IN WHICH ARREST WAS GENERATED IN THE PRESENCE OF KN93 (PMAD-KN) OR RYANODINE (PMAD-RY), AS WELL AS A CONTROL ANIMAL EXPOSED TO IV INFUSION OF EPINEPHRINE (EPI) FOR 30 MINUTES. CELLS WERE PACED STEADILY AT 1HZ. B. POOLED ANALYSIS OF ΔF/FPEAK FOR ALL CONDITIONS TESTED. THE ΔF/FPEAK WAS SIGNIFICANTLY HIGHER IN ANIMALS EXPOSED TO EPINEPHRINE INFUSION AND CARDIAC ARREST. RYANODINE AND KN93 REDUCED ΔF/FPEAK TO CONTROL LEVELS IN PMAD VENTRICULAR MYOCYTES. WT WAS NO DIFFERENT THAN SHAM. N=90, 123, 75, 9, 11, 15, 11, 31, 20, 51, 119, 19, 11 CELLS FOR CONTROL, PMAD, PMAD-AIP, PMAD-KN, PMAD-RY, EPI INFUSION, CONTROL-KN93 (CNTR-KN), CONTROL RYANODINE (CNTR-RY), EPI INFUSION WITH RYANODINE RYANODINE (EPI-RYR), PMAD- LANGENDORFF, BRAINSTEM

herniation (BSH), and BSH-ryanodine), and PMAD-H89. Cntr-Sham experiments demonstrated no difference compared with control. P values compared to control for PMAD, Epi infusion, were 6.4e-24, 2.2e-18 (corrected for multiple comparisons by Bonferroni correction). All other comparison were not significant. C. Example CICR transients from two different PMAD cells. Top panel shows CICR in response to 1Hz electrical stimulation followed delayed calcium transients. Bottom panel shows spontaneous calcium transients competing for paced rhythm at 1Hz pacing. D. Example traces for simultaneous CICR (bottom, gray) and cellular force (top, black) measurements are shown shown for an isolated cell electrically paced at 1 Hz. The SL was (in μm) ~1.87,~1.94 and ~2.0 at the slack length, the first, and the second stretch. E. Pooled analysis of velocity of contraction (V_c) vs sarcomere length for control and PMAD. The y axis is the V_c and the x is sarcomere length. Baseline (filled) and stretched (open) for pairs of similar stretches from ~1.8 μm ~ 2.0 μm. V_c were significantly lower in PMAD (red) than control (black); more negative is faster rate of contraction . However, the percentage change between the stretch and baseline in each group was identical (~152% of baseline), n= 8, 9 cells from 3 and 4 hearts for PMAD and control hearts respectively. F. Pooled data comparing unloaded %SL vs $\Delta F/F_{peak}$ of CICR under control, PMAD, epinephrine infusion in animal, but not cells (EPI inf), and epinephrine in isolated cells (EPI cell), but not in whole animal), as well as PMAD in presence of Alda-1 (PMAD-Alda, n=25 cells from 4 animals). N for control, PMAD, and Epi inf are the same as above. G. Baseline Force (BSF) in example cells paced steadily at 1 Hz in control, PMAD, PMAD-KN, PMAD-Ry cells. BSF was lower than control in PMAD cells, but even lower when calcium memory was blocked with either ryanodine or KN93. H. Pooled data for BSF measurements at 1 Hz steady-state pacing in control, PMAD in the presence and absence of KN93 or ryanodine. n= 8, 8, 5, 4 cells for control, PMAD, PM AD-KN, PMAD-Ry

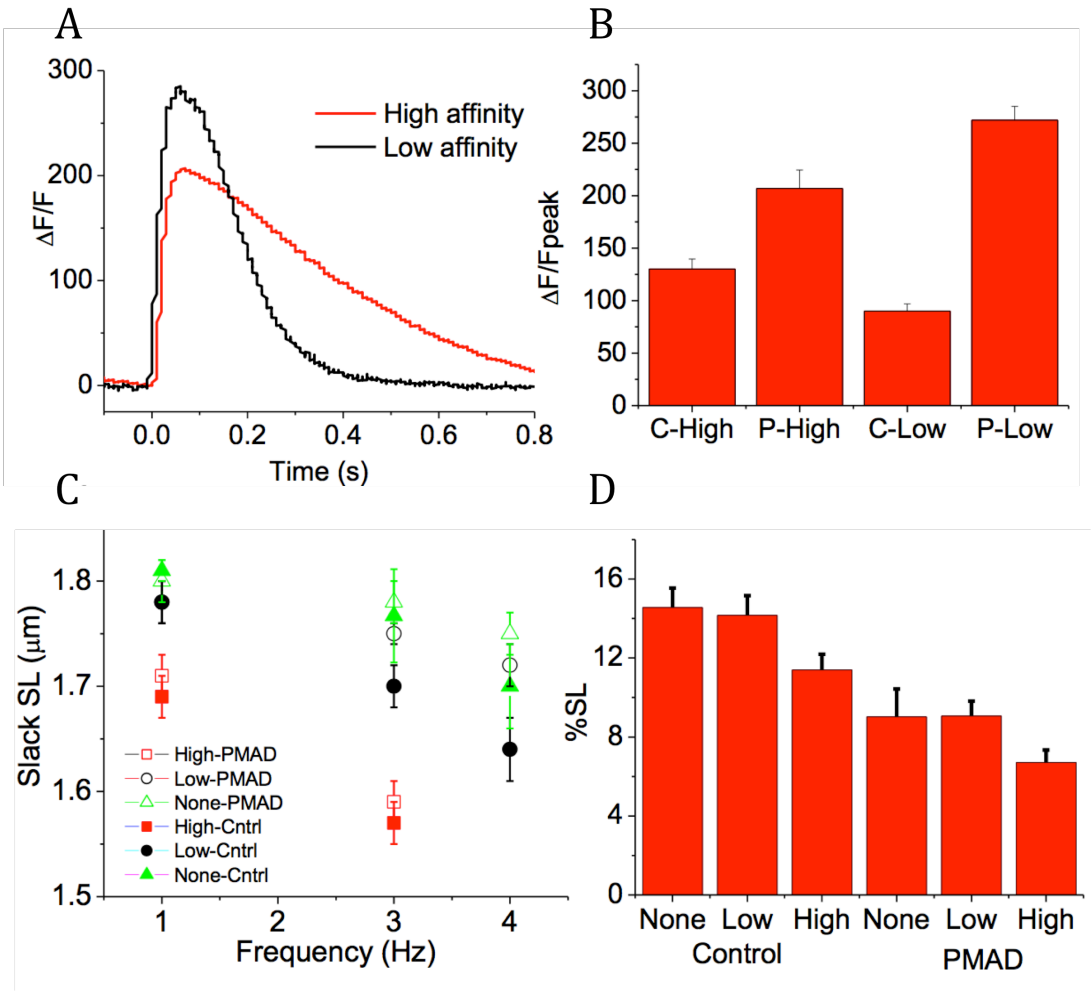

FIGURE 3-9 - HIGH VS LOW AFFINITY CALCIUM INDICATORS IN PMAD CALCIUM MEASUREMENTS.

A. TWO SUPERIMPOSED CICR TRANSIENTS FROM THE SAME PMAD CELL POPULATION LOADED WITH EITHER WITH FLUO-5F (LOW AFFINITY, BLACK) OR WITH FLUO-4 (HIGH AFFINITY, RED) ARE SHOWN DEMONSTRATING THE SIGNIFICANT FILTERING EFFECT OF THE HIGHER AFFINITY DYE BOTH IN TERMS OF AMPLITUDE AND TIME COURSE. ON AVERAGE, DECAY PHASE WAS SIGNIFICANTLY PROLONGED TO 533 ± 16 MS WITH FLUO-4 (DATA NOT SHOWN), ~100 MS LONGER THAN FLUO-5F (SEE TEXT). B. CALCIUM TRANSIENT ΔF/FPEAK FOR BOTH CONTROL (C) AND PMAD (P) CELLS MEASURED USING EITHER THE HIGH AFFINITY WAS HIGHER THAN THAT OBSERVED FOR LOW AFFINITY (LOW) OR HIGH AFFINITY (HIGH) FLUO DERIVATIVE. THE DIFFERENCE BETWEEN CONTROL AND PMAD WAS SUBSTANTIALLY MISSED USING THE HIGH AFFINITY DYE (ONLY ~152% FOR PMAD *VS* CONTROL ΔF/FPEAK, P=0.02, N=32 FROM 2 RATS FOR HIGH AFFINITY PMAD AND CONTROL). IN ADDITION, THIS CLIPPING OF THE DATA CAN AT THE EXPENSE OF PROLONGED BUFFERING WITH HIGHER ΔF/FPEAK WITH HIGH AFFINITY DYE IN CONTROL AND FRANK SATURATION WITH LOWER ΔF/FPEAK WITH HIGH AFFINITY DYE IN PMAD COMPARED TO RESPECTIVE MEASUREMENTS WITH LOW AFFINITY DYE. C. THE RESTING DIASTOLIC LENGTH MEASURED JUST PRIOR TO THE NEXT STIMULUS IN A PACING TRAIN (Y AXIS) IS PLOTTED AGAINST PACING FREQUENCY (X-AXIS) IN CELLS LOAD WITHOUT DYE (GREEN), WITH LOW AFFINITY DYE (BLACK) OR HIGH AFFINITY DYE (RED) IN CONTROL (OPEN) AND PMAD CELLS (FILLED). AS CAN BE SEEN, HIGH AFFINITY DYE SIGNIFICANTLY PREVENTS THE CELL FROM RETURNING TO RESTING LENGTH AT ALL FREQUENCIES TESTED, A PROCESS THAT RESULTS FROM THE DOMINANT BUFFERING FEATURE OF THE DYE. C. %SL IN UNLOADED CELLS FROM CONTROL AND PMAD CELLS LOADED WITH HIGH OR LOW AFFINITY CALCIUM DYE AT STEADY-STATE1 HZ PACING. THE HIGH AFFINITY DYE REDUCES THE %SL IN CONTROL CELLS ALMOST AS MUCH AS CARDIAC DEATH DOES ALONE, WHILE THE LOW AFFINITY DYE AND 1 HZ PACING DOES NOT

APPRECIABLE ALTER CONTRACTILE PERFORMANCE. FOR ALL EXPERIMENTS ABOVE, N=32 FROM 2 RATS FOR HIGH AFFINITY EXPERIMENTS IN BOTH PMAD AND CONTROL.

3.8. Calcium Force Relationship

As mentioned above, previous reports have documented an impaired myofilament affinity to calcium and a rightward shift in the force-pCa curve. However, many of these experiments relied on permeabilised preparations.[70] To overcome this limitation, other groups have investigated force-calcium relationships using whole muscle preparations and calcium concentration curves generated by varying extracellular calcium up to 30 mM in the presence of high affinity calcium dyes.[70] For these reasons, we developed a technique to measure calcium fluorescence in dynamically contracting cells using the lower affinity calcium dye Fluo-5f to investigate the calcium-force relationship.

The introduction of Fluo-5f did not distort the %SL (Figure 3.9). We explored the effects of load and CICR simultaneously in dynamically twitching fibers. It has been reported that CICR changes with stretch in amphibian cells,[71] but this has not yet been reported in mammalian cells, so we first examined whether the CICR waveform is affected by load. We saw no appreciable differences in CICR with stretch (Figure 3.8 D). We next investigated length dependent activation, the putative mechanism for the Frank-Starling effect,[72] by comparing contraction velocity before and after stretch. We compared the changes in the velocity of contraction between a group of control and PMAD cells (Figure 3.8 E). In these cells, care was taken to equalise baseline and stretched sarcomere lengths. While the post-stretch change in velocity was

similar (ratio post to pre-stretch v_c: 1.7±0.2 *vs* 1.8±0.2 for control *vs* PMAD, p=0.5), PMAD cells showed a significantly (36%) reduced length-dependent activation based on a decreased baseline velocity of contraction.

We generated calcium-force-frequency-relationships (CFFR) for control and PMAD cells shown in Figure 3.10 A and 3.10 B. These plots summarize the reduced myofilament calcium sensitivity demonstrating a reduction in force across all frequencies despite a markedly elevated CICR.

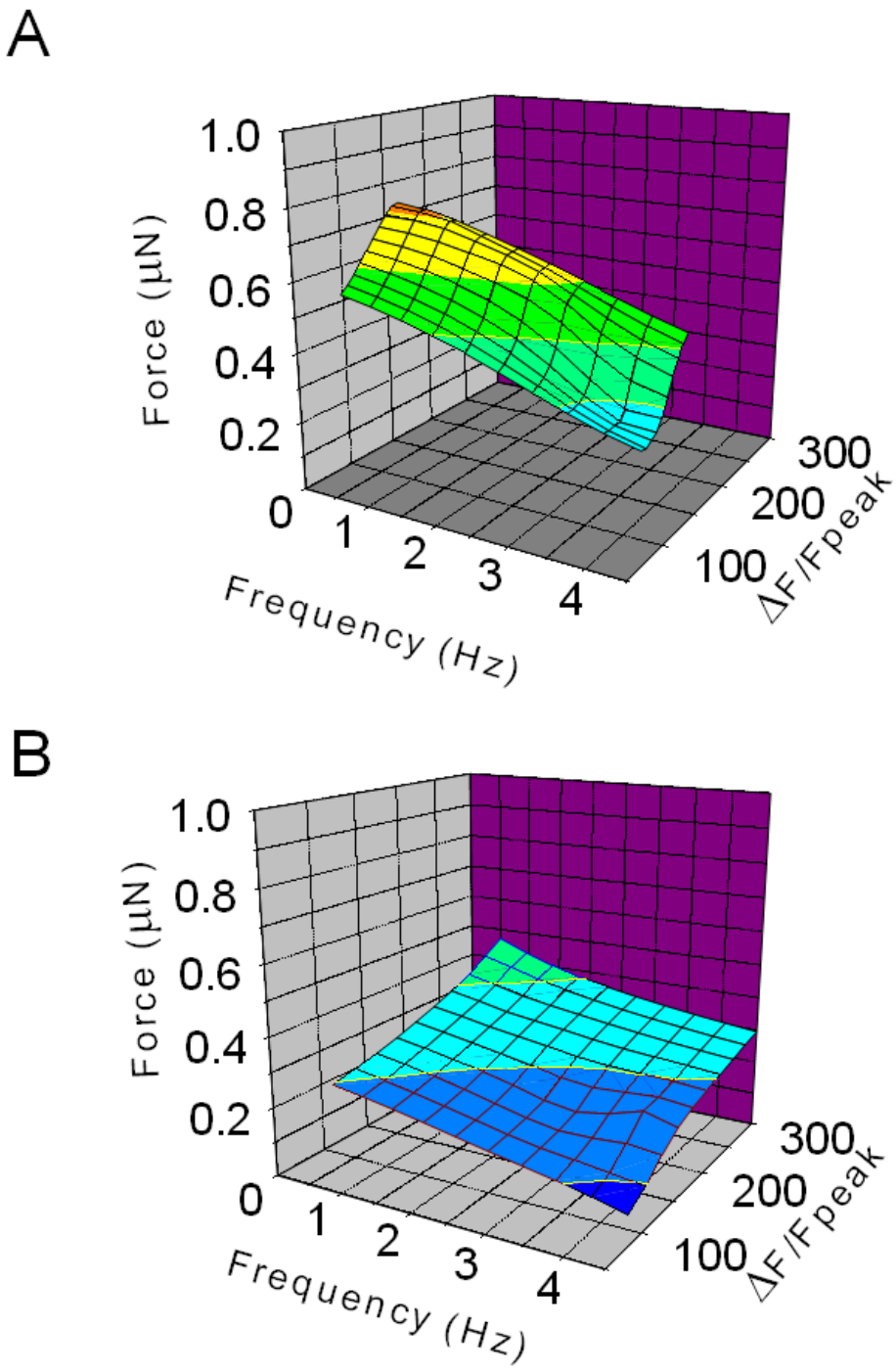

FIGURE 3-10 – CALCIUM FORCE FREQUENCY RELATIONSHIPS AFTER CARDIAC ARREST

A. PLOT OF FORCE, PACING FREQUENCY AND CALCIUM EXPRESSED AS ΔF/FPEAK FOR CONTROL CELLS AT SLACK LENGTH LOADED WITH FLUO-5F AND SIMULTANEOUSLY STRETCHED WITH CF. N=4 CELLS FROM 2 CONTROL HEARTS. THE CURVE SHOWS A STEEP CURVE SHIFTED TO LOWER ΔF/FPEAK. FORCE IS COLOR CODED WITH THE SAME PALLETTE AS IN PANEL B. B. SIMILAR PLOT IN POST ARREST CELLS. N=4 CELLS FROM 2 CONTROL HEARTS. BY COMPARISON TO PANEL A, THE CURVE IS SHIFTED TO A FLATTER CURVE DESPITE ALSO BEING SHIFTED TO HIGHER ΔF/FPEAKS (RIGHTWARD) AT ALL PACING FREQUENCIES. FORCE IS COLOR CODED WITH THE SAME PALLETTE AS IN PANEL A, AND ALL SCALE BARS ARE IDENTICAL.

3.9. CAMKII autophosphorylation increases post-cardiac arrest

CAMKII is known to be a mediator of early long term potentiation in neurons. LTP is part of the spectrum of synaptic plasticity and is associated with enhanced signalling in which CAMKII autophosphorylation plays an important role. We hypothesized that CAMKII autophosphorylation was a critical mediator of calcium cardiac memory. To confirm this observation, we used immunoblot analysis of whole heart isolates flash frozen immediately after resuscitation in PMAD and compared this with control hearts similarly treated. Blots were analyzed with site-specific antibodies against total CAMKII (Figure 3.11, top panel), threonine-287 (T287; autophosphorylation site, middle panel), and beta-actin expression in control and PMAD. CAMKII total expression increased non-significantly in PMAD compared with control hearts. However, the T287 autophosphorylation was significantly higher in PMAD.

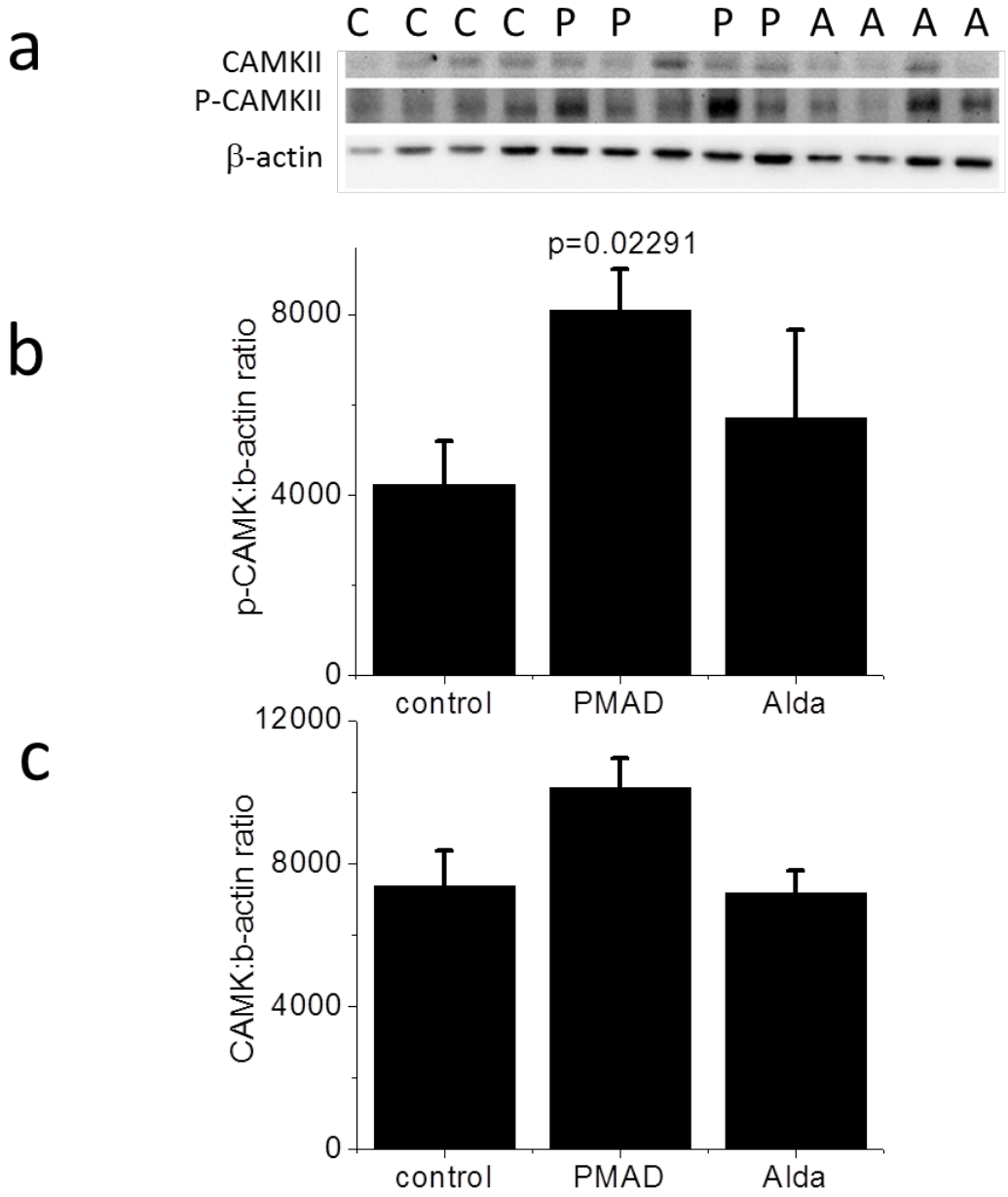

FIGURE 3-11 – CAMK PHOSPHORYLATION IN PMAD WITH AND WITHOUT ALDA-1. A. IMMUNOBLOTS AGAINST CAMKII (TOP PANEL), AUTOPHOSPHORYLATED (T287) CAMKII (MIDDLE PANEL), AND B-ACTIN (BOTTOM PANEL) IN CONTROL (C), PMAD IN THE ABSENCE (P) AND PRESENCE OF ALDA-1 (A). B. QUANTITATIVE ASSESSMENT OF IMMUNE BLOT ANALYSIS AGAINST CAMKII NORMALIZED TO B-ACTIN C. QUANTITATIVE ASSESSMENT OF IMMUNE BLOT ANALYSIS AGAINST AUTOPHOSPHORYLATED CAMKII NORMALIZED TO B-ACTIN. FOR AUTOPHOSPHORYLATED CAMKI, STUDENT T-TEST P=0.02291, AND MANN-WHITNEY P=0.03

3.9.1. Alda-1 improves cardiac performance while reducing CICR in DCD

Although much is known regarding the role of oxidative stress in ischemia and reperfusion, less is understood regarding aldehydic stress. Recently, it has been shown in the setting of myocardial infarction that ALDH2 plays a pivotal role in cardioprotective signalling and reduces ischemic damage through detoxification of reactive aldehydes (such as 4-HNE and acetaldehyde) to non-reactive acids (such as 4-hydroxynon-2-enoic acid and acetic acid). A small molecule activator of ALDH2 (Alda-1) prevents inhibition of ALDH2 (by 4-HNE) and, thus, ensures continued detoxification of reactive aldehydes during ischemia-reperfusion.[73] We hypothesized that activating ALDH2 during *in vivo* cardiac arrest would improve myocardial performance. Indeed, Alda-1 administration had a dramatic positive impact. First, weaning from resuscitation *in vivo* (defined as reaching 20% of the pre-arrest MAP) occurred in 63% (n=8 animals) of animals exposed to Alda-1 compared with only 12% (n=30 animals) in the absence of Alda-1 after cardiac arrest (figure 3.12 D). Furthermore, the performance of the hearts weaned off bypass support after cardiac arrest was improved dramatically in the presence of Alda-1. In particular, we found that whole animal cardiac contractility, as indexed by ESPVR, PRSW, CI, and τ were returned to near control levels after Alda-1 (Table 3.2 and figure 3.12 A-C). At the cellular level, we found that that the increased CICR seen in PMAD was reduced by 30% (Figure 3.8 B), and that the %SL vs CICR was improved as well to a state between control and PMAD (Figure 3.8 F). In addition, immunoblot analysis of CAMK and autophosphorylated CAMKII revealed that in the

presence of Alda-1 during cardiac arrest, T287 autophosphorylation was abrogated (Figure 3.11 B-C). Alda-1 had no effect on these same parameters before arrest

Table 3.2 – In Vivo measurements

	Control	PMAD (P Value)	Alda - PMAD
ESPVR (mmHg/µl)	1.0±0.10	0.5±0.1 (0.02)	1.1±0.2
PRSW (mmHg)	58±8	30±6 (0.02)	55±16
CI (mmHg/µl)*s	93±6	64±6 (0.005)	89±12
τ (ms)	12±3	45±6 (7e-11)	19±7

TABLE 3. 2 - IN VIVO PARAMETERS; ESPVR, PRSW, CI AND TAU IN CONTROL N=11, PMAD N=30 AND PMAD WITH ALDA ON BOARD N=8.

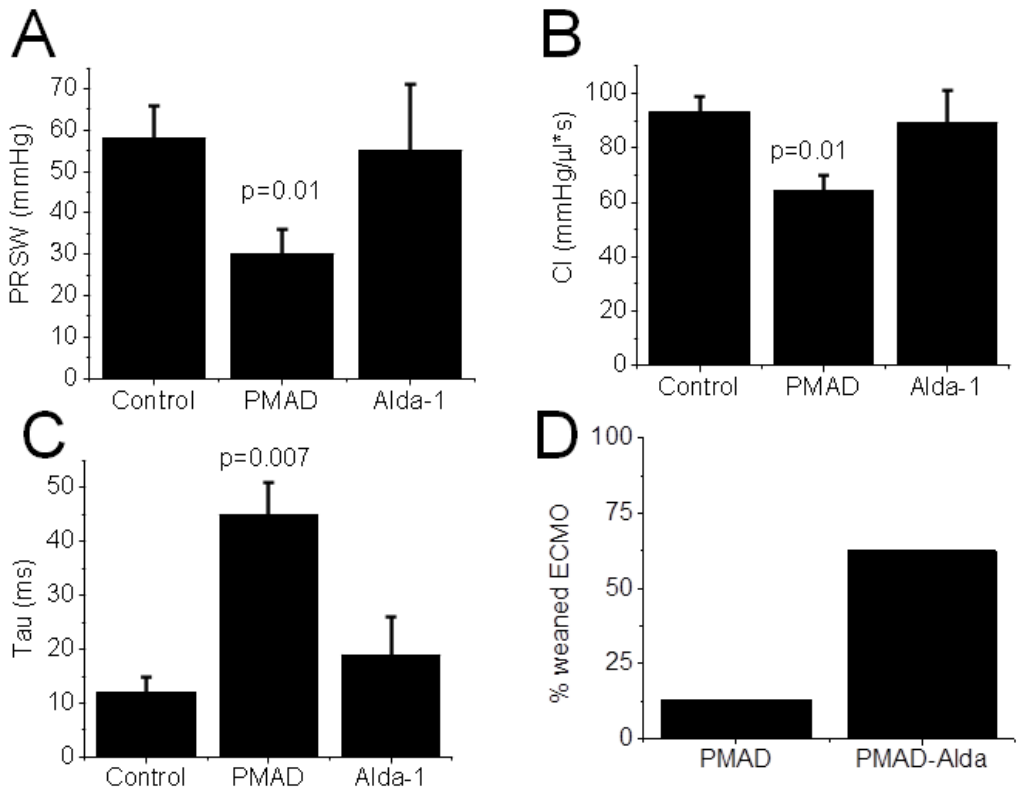

FIGURE 3-12 – ALDA-1 IMPROVED IN VIVO CONTRACTILITY AND RECOVERY RATE TO SPONTANEOUS CIRCULATION AFTER CARDIAC ARREST. A, SUMMARY DATA FOR PRELOAD RECRUITABLE STROKE WORK (PRSW) FOR CONTROL, PMAD, AND PMAD-ALDA (*P*=0.04). B, SUMMARY DATA FOR CARDIAC INPUT (CI) FOR CONTROL, PMAD, AND PMAD-ALDA. C, SUMMARY DATA FOR TAU FOR CONTROL, PMAD, AND PMAD-ALDA. D, ALDA-1 IMPROVED CHANCES OF WEANING FROM ECMO RESUSCITATION. CONTROL N=11, PMAD =30 & PMAD-ALDA N=8. *P* VALUES IN GRAPHS ARE WITH RESPECT TO CONTROL USING POST HOC ANALYSIS. COMPARISONS BETWEEN GROUPS WERE PERFORMED WITH KRUSKALL-WALLIS NONPARAMETRIC TESTS

3.10. In Situ Optical Mapping of Voltage and Calcium in the Heart

We chose di-4-ANBDQPQ[53] to report V_m, and rhod-2(AM) to report $[Ca^{2+}]_I$ changes, as both dyes had previously been used successfully in diluted-blood perfused Langendorff hearts.[74] To avoid cross-talk between dye emissions, we made use of the ratiometric properties of di-4-ANBDQPQ.[53,55] As shown in Figure 3.13 A, excitation of this dye with either blue or red wavelengths produces action potential (AP) fluorescence signals that

increase or decrease with changes in V_m, respectively (although not used in this study, ratiometric V_m imaging can be used to reduce motion artifacts). During exposure to green light (used for excitation of rhod-2(AM)) there is no change in voltage- related emission, as this occurs at the excitation-isosbestic point for di-4-ANBDQPQ. This approach allows simultaneous V_m and $[Ca^{2+}]_i$ imaging (Figure 3.13) without emitted signal cross-talk.

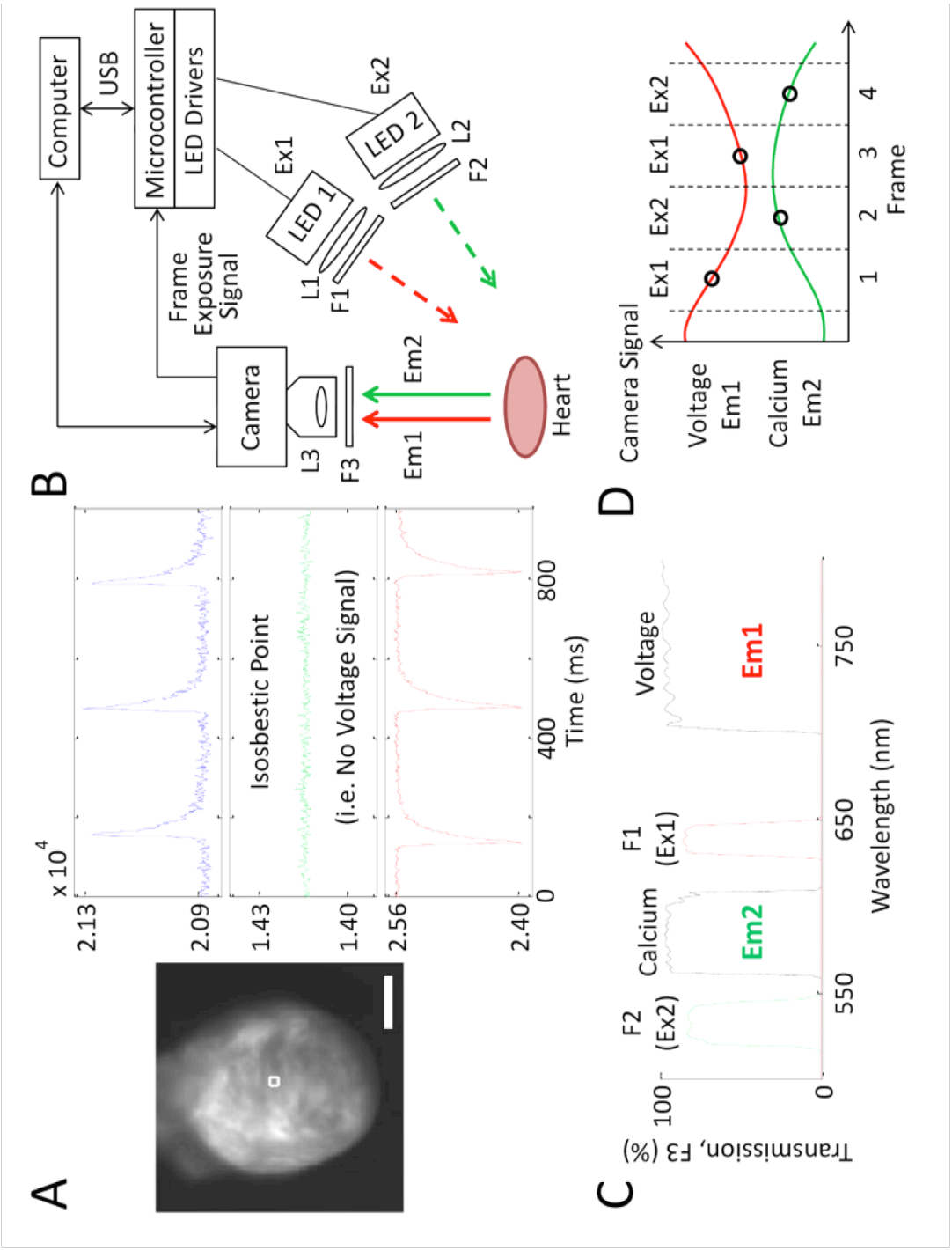

FIGURE 3-13 - SCHEMATIC ILLUSTRATION OF MULTI-PARAMETRIC IMAGING APPROACH. (A) DI-4-ANBDQPQ FLUORESCENCE IN A LANGENDORFF-PERFUSED RAT HEART (SINUS RHYTHM), EXCITED WITH BLUE (BLUE LED, 470610 NM FILTER), GREEN (GREEN LED, 540612.5 NM FILTER) AND RED (RED LED, 640610 NM FILTER) WAVELENGTHS. THESE FLUORESCENCE SIGNALS (TAKEN FROM THE 464-PIXEL WHITE-SQUARE REGION ON THE LEFT-VENTRICLE) WERE COLLECTED THROUGH A CUSTOM-MADE MULTI-BAND EMISSION FILTER (F3 IN B, C). THE GREEN TRACE ($[Ca^{2+}]_i$) SHOWS NEGLIGIBLE EMISSION CHANGES WHEN DI-4-ANBDQPQ IS EXCITED AT THE EXCITATION- ISOSBESTIC POINT. SCALE BAR = 5 MM. (B) SCHEMATIC OUTLINE OF THE IMAGING SYSTEM, HIGHLIGHTING KEY COMPONENTS. SINCE ONLY ONE CAMERA IS USED, THE SYSTEM REQUIRES NO CHALLENGING OPTICAL ALIGNMENT. EXCITATION SOURCES EX1: RED LED WITH A 640610 NM FILTER (F1), EX2: GREEN LED WITH A 540612.5 NM FILTER (F2). (C) TRANSMISSION SPECTRUM OF THE CUSTOM MULTI-BAND EMISSION FILTER THAT PASSES BOTH V_M (EM1) AND $[Ca^{2+}]_i$ (EM2) EMITTED FLUORESCENCE SIGNALS. F1 AND F2 EXCITATION FILTER SPECTRA ARE SHOWN AS DASHED CURVES. (D) BASIC PRINCIPLE BEHIND THE SINGLE-CAMERA MULTI-LED APPROACH: DURING ANY FRAME EXPOSURE (OCCURRING BETWEEN THE VERTICAL DASHED LINES), THE PARAMETER BEING MEASURED BY THE CAMERA SENSOR IS DETERMINED BY THE EXCITATION SOURCE (EITHER EX1 OR EX2) THAT IS SWITCHED ON DURING THAT PERIOD. A SUFFICIENTLY

FAST CAMERA (COMPARED TO EM1 AND EM2 SIGNAL DYNAMICS), AND INTERPOLATION BETWEEN MEASURED DATA POINTS, PROVIDES SIMULTANEOUS MEASURES OF MULTIPLE PARAMETERS, HERE V_M AND $[Ca^{2+}]_i$. FOR THESE IMAGES, BLEBBISTATIN WAS USED TO ELIMINATE THE CONTRIBUTION OF MOTION TO THE SIGNALS.

A schematic illustration of the overall single-camera imaging/ multiple-LED excitation system is shown in Figure 3.13 B. The multi- band emission filter used (F3 in Figure 3.13 B) was custom-fabricated by Chroma Technology (Bellows Falls, VT, USA) to provide transmission bands for fluorescence emitted from both di-4- ANBDQPQ (Em1) and rhod-2(AM) (Em2; Figure 3.13 C). Figure 3.13 D illustrates the principle behind our approach: During one camera frame-exposure, excitation light 1 (Ex1) is turned on, producing V_m signal emission collected through the Em1-band; during the next frame exposure, excitation light source 2 (Ex2) is turned on, producing $[Ca^{2+}]_i$ signal emission collected through the Em2- band, and so on. Since the camera frame rate (here 500 frames- per-second; kHz frame rates can be achieved with pixel-binning) is faster than physiological signal dynamics, with interpolation, one can record electrophysiologically-relevant dynamic changes in both V_m and $[Ca^{2+}]_i$ (such as the action potential [AP] and the calcium transient [CaT]), and assess AP and CaT propagation.

Figure 3.14 shows results obtained using the imaging system in proof-of-principle work on saline-perfused rat hearts in Langendorff mode. In Figure 3.14 A, AP and CaT fluorescence signals from one location on the left ventricle are plotted, while Figure 3.14 B shows a time series of normalized V_m and $[Ca^{2+}]_i$ fluorescence intensity maps, highlighting the well-known

delay (here about 17 ms) of the CaT peak relative to AP upstroke (see Movie M1 in eThesis). M1 shows AP and CaT fluorescence signals from four other points on the same heart, demonstrating signal quality across the whole field of view. Unless otherwise stated for these images and what follows, blebbistatin was used to reduce the contribution of motion to the fluorescence signals.

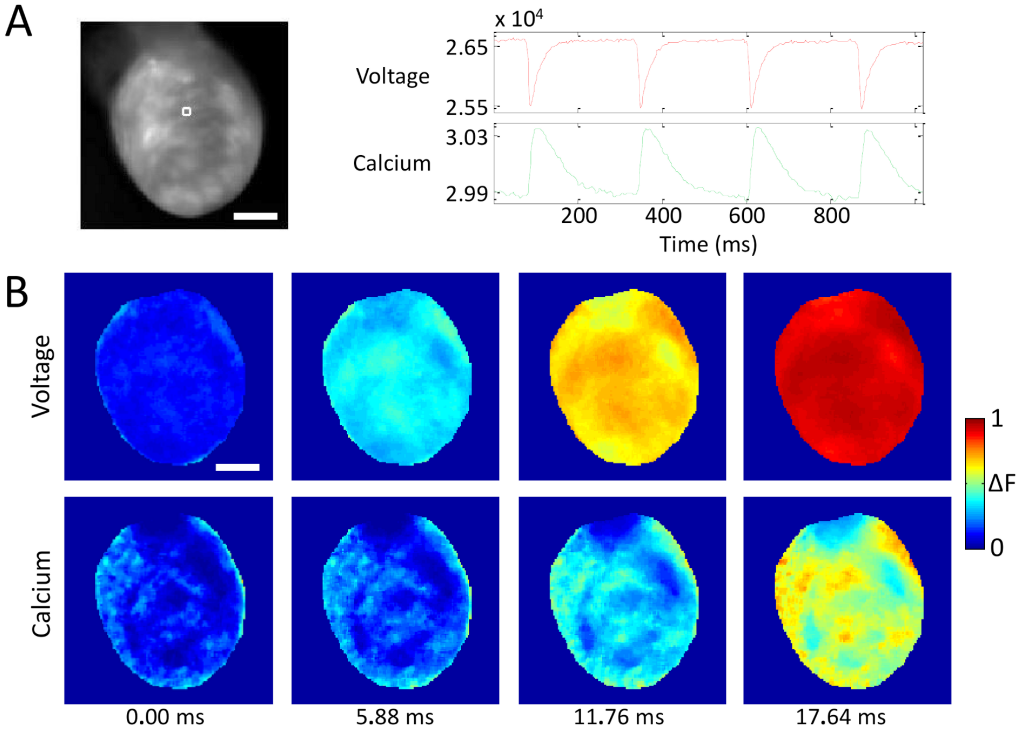

FIGURE 3-14 - SIMULTANEOUS IMAGING OF V_M AND $[CA^{2+}]_I$ IN A LANGENDORFF-MODE SALINE-PERFUSED RAT HEART. (A) V_M (RED) AND $[CA^{2+}]_I$ (GREEN) FLUORESCENCE SIGNALS (CAMERA SIGNALS ON A 16-BIT SCALE) TAKEN FROM THE 464-PIXEL WHITE-SQUARE REGION ON THE LEFT VENTRICLE. (B) NORMALIZED FLUORESCENCE INTENSITY MAPS (COLORBAR SHOWN) AT PROGRESSIVE TIME POINTS DURING SINUS RHYTHM. THE DELAY OF THE CAT RELATIVE TO THE AP PEAK (,17 MS FROM TRANSIENTS IN PART A) IS CLEARLY VISIBLE. SCALE BAR = 5 MM. FOR THESE IMAGES, BLEBBISTATIN WAS USED TO ELIMINATE THE CONTRIBUTION OF MOTION TO THE SIGNALS.

Next, we applied our imaging system to the rat heart in vivo using di-4-ANBDQPQ and rhod-2(AM) in isolation. Figure 3.15 shows the in vivo

preparation used (details can be found in the Methods section). In Figure 3.15 F, we show summed results of the heart rate (in ms), PR, QRS, and QTc intervals for far field EKG recordings immediately before and 5 minutes after loading of voltage dye. We found no appreciable differences in these ECG traces (n = 3). In addition, mean arterial pressure (MAP) is shown again immediately before and 5 minutes after loading with voltage dye. There was no appreciable effect on MAP with voltage dye loading. As noted in the Methods section, to reduce motion contamination in both the V_m and $[Ca^{2+}]_i$ fluorescence, blebbistatin was added during imaging. With the addition of blebbistatin we used cardiopulmonary bypass (CPB) circuit to maintain blood pressure as described in the Methods section.

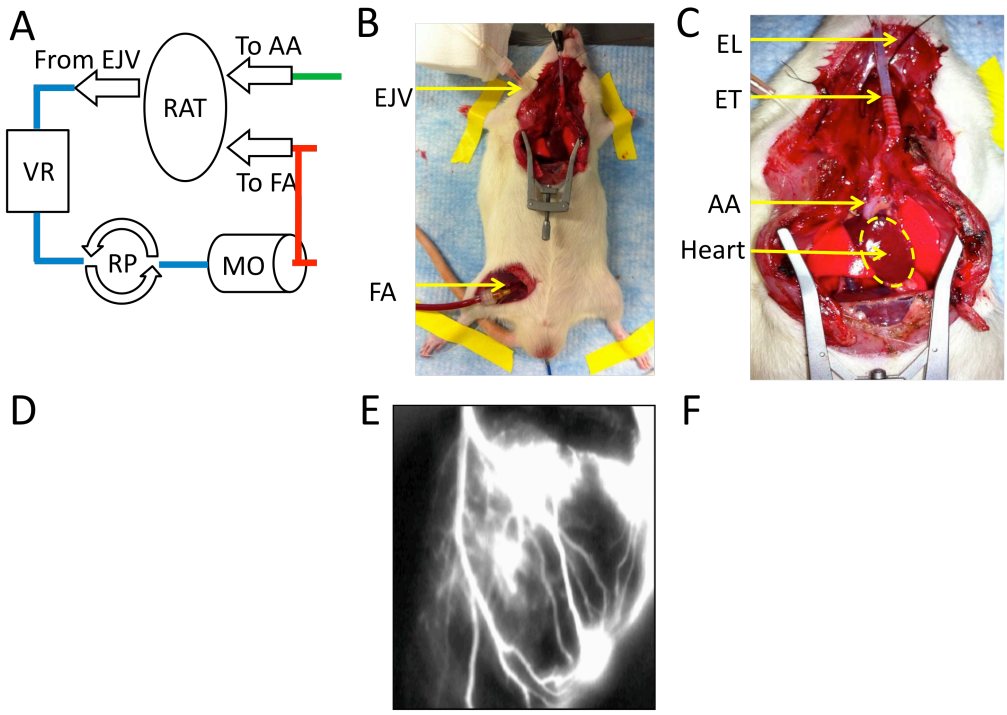

FIGURE 3-15 - IN VIVO RAT WHOLE-HEART PREPARATION. (A) A SCHEMATIC OF THE RAT CARDIOPULMONARY BYPASS (CPB) CIRCUIT BASED ON A STANDARD PUMP CIRCUIT (EJV: RIGHT EXTERNAL JUGULAR VEIN CATHETER, VR: VENOUS RESERVOIR, RP: ROLLER PUMP, MO: MINIATURE MEMBRANE OXYGENATOR, FA: RIGHT FEMORAL ARTERY CATHETER, AA: ASCENDING AORTA CATHETER VIA RIGHT CAROTID ARTERY). IN CPB MODE, BLOOD IS PUMPED FROM THE EJV THROUGH THE MO TO THE FA, EPICTED BY ARROWS IN THE FIGURE. DYE IS INJECTED THROUGH THE AA CATHETER. (B) WHOLE-ANIMAL VIEW OF THE PREPARATION. (C) ZOOMED-IN VIEW OF THE OPEN CHEST, WITH THE HEART IN CLEAR VIEW

(EL: ESOPHAGEAL ECG LEAD, ET: ENDOTRACHEAL TUBE). (D) AN EXAMPLE OF RVP AT 12 HZ TO DROP BLOOD PRESSURE (BP; RED TRACE), AFTER WHICH DYE WAS INJECTED VIA THE AORTIC ROOT. THE BP RECOVERED SOON AFTER CESSATION OF PACING. IMMEDIATELY AFTER LOADING AS SHOWN HERE, THE BP INCREASED REFLECTING THE FRANK-STARLING EFFECT OF PROLONGED LOADING. THE ACCOMPANYING ECG (BLACK TRACE) IS ALSO SHOWN. (E) ZOOMED-IN VIEW OF THE HEART IMMEDIATELY AFTER RHOD-2(AM) INJECTION DEMONSTRATING A FLUORESCENT CORONARY ANGIOGRAM. (F) POOLED DATA ON HEART RATE (HR IN MS), MEAN ARTERIAL BP (MAP IN MMHG—RIGHT AXIS), AS WELL AS FAR FIELD EKG PARAMETERS OF PR, QRS, AND QTC INTERVALS (IN MS) FOR IMMEDIATELY BEFORE (BLACK) AND AT 5 MINUTES AFTER LOADING WITH VOLTAGE DYE (RED).

Figure 3.16A shows normalized V_m fluorescence intensity maps at progressive time points in a heart in vivo (see Movie M2 in eThesis). Figure 3.16B shows normalized V_m fluorescence intensity maps at progressive time points 1 hour after LAD suture ligation to induce local myocardial infarction (to be differentiated from scar) (see Movie M3 in eThesis). In the left panel, a raw grayscale fluorescence image of V_m signal emission during diastole shows that the infarcted tissue is darker than surrounding normal myocardium (upper right quadrant), as the dye cannot reach the infarct. In the normalized V_m fluorescence intensity maps, AP propagation proceeds through viable tissue (best appreciated in Movie M3 in eThesis). In Figure 3.16C, we show a necropsy specimen of the endocardial surface of the same heart, highlighting V_m emission differences at the normal (bright) and infarcted (dark) tissue. The left panel in Figure 3.16C shows the specimen submersed beneath 1 cm of blood, while on the right, a coverslip has been placed on the tissue (bubbles highlight the coverslip-tissue interface). This gross demonstration of normal versus infarct tissue illustrates the ability of the dye to differentiate between the two tissue types rapidly. Clearly, collateralization of infarcted tissue by remodelling, and identification of scar from viable tissue will be critical to investigate, as has been done using

voltage dyes in vitro.[50] But, this was not possible in this small animal model because, while the LAD infarct did indeed lead to scar formation we did not see collateralization in our infarct model. In Figure 3.16D, we show an example of calcium fluorescence measurements in vivo. Here, normalized $[Ca^{2+}]_i$ fluorescence intensity maps are shown for the epicardial surface containing the atria. The activity shown is during atrial fibrillation. Because the electrical activation frequency of atrial fibrillation is exceedingly high (8–9 Hz in the rat) and disorganised, atrial contraction is uncoordinated. While this is detrimental clinically, imaging is improved as movement is minimized (no blebbistatin needed; see Movie M4 in eThesis).

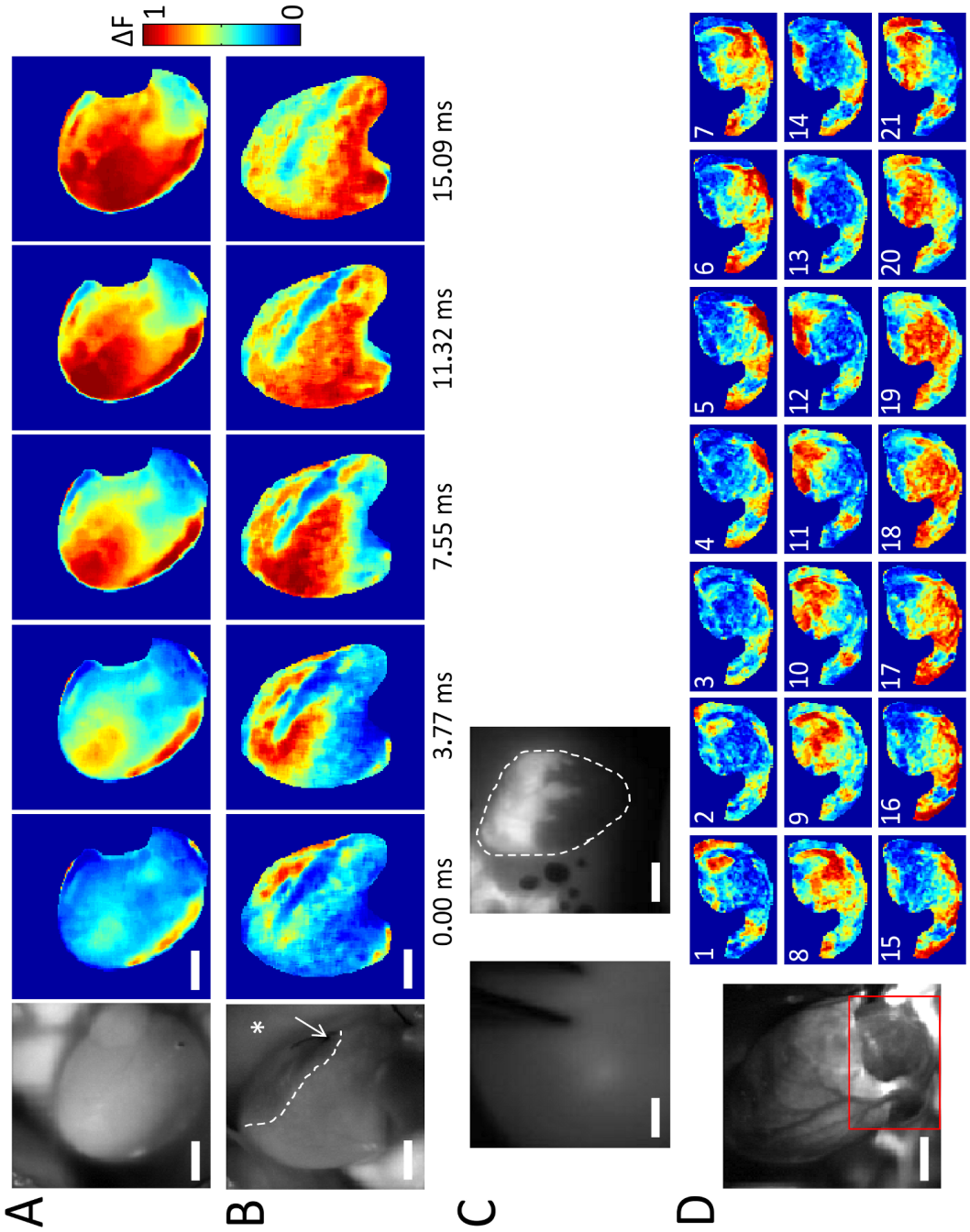

FIGURE 3-16 - IN VIVO IMAGING OF V_M AND $[CA^{2+}]_I$ DYNAMICS IN RAT VENTRICLES/ATRIUM, DURING SINUS RHYTHM AND IN ATRIAL FIBRILLATION. (A) NORMALIZED V_M FLUORESCENCE INTENSITY MAPS (COLOUR BAR SHOWN) AT PROGRESSIVE TIME POINTS OF THE CARDIAC CYCLE WITH THE HEART IN SINUS RHYTHM. (B) NORMALIZED V_M FLUORESCENCE INTENSITY MAPS AT SEQUENTIAL TIME POINTS OF THE HEART IN SINUS RHYTHM, 1 HOUR AFTER SUTURE-LIGATION OF THE PROXIMAL LAD (TO MIMIC MYOCARDIAL INFARCTION). IN THE LEFT-MOST (RAW GRAYSCALE) PANEL, THE INFARCTED TISSUE CAN BE RECOGNIZED AS THE DARK REGION (ONE SIDE DEMARCATED BY DOTTED WHITE LINE) IN THE TOP-RIGHT QUADRANT OF THE IMAGE; IN THE NORMALIZED FLUORESCENCE MAPS IT IS RECOGNIZED AS THE PERSISTENTLY BLUE REGION IN THE SAME AREA. SUTURE LOCATION IS INDICATED WITH A WHITE ARROW. THE ASTERISK MARKS LUNG TISSUE. (C) ENDOCARDIAL VIEW OF SAME INFRACTED HEART AS IN (B), AFTER NECROPSY, SUBMERGED IN BLOOD (LEFT) AND WITH A COVERSLIP GENTLY PLACED ON THE TISSUE (RIGHT). THE BRIGHT AREAS CORRESPOND TO NON-INFARCTED TISSUE, WHILE THE DARK AREAS CORRESPOND TO INFARCTED TISSUE

WHERE THE DYE IS ABSENT. THE DASHED WHITE LINE DEMARCATES HEART TISSUE BORDER. NOTE THE AIR BUBBLES ON THE LEFT SIDE OF THE PANEL AT THE COVERSLIP-TISSUE INTERFACE. (D) NORMALIZED [CA^{2+}]$_i$ FLUORESCENCE INTENSITY MAPS AT SEQUENTIAL CAMERA FRAMES IN PART OF THE LEFT AND RIGHT ATRIA DURING ATRIAL FIBRILLATION, INDUCED BY GLOBAL VENTILATORY HYPOXIA. SCALE BAR = 5 MM. FOR A AND B, BLEBBISTATIN WAS USED TO REDUCE, BUT NOT ELIMINATE, THE CONTRIBUTION OF MOTION TO THE SIGNALS, WHILE FOR C, NO BLEBBISTATIN WAS USED. TISSUE SHOWN IN B AND C CORRESPOND TO A DIFFERENT HEART THAN THAT SHOWN IN A.

In the final set of experiments, we dual-loaded the in vivo heart with both rhod-2(AM) and di-4-ANBDQPQ. Figure 3.17A shows V_m (red) and $[Ca^{2+}]_i$ (green) fluorescence signals from a point on the left ventricle, demonstrating AP and CaT measurements (some motion artefacts present in signals). Figure 3.17B shows normalized V_m and $[Ca^{2+}]_i$ fluorescence intensity maps at progressive time points from the same heart (see Movie M5 in eThesis). Figure 3.17C shows V_m (top traces) and $[Ca^{2+}]_i$ (bottom traces) fluorescence signals from three points on the left ventricle of another heart, demonstrating varying motion artefact effects when contraction is not completely eliminated. In contrast to the loading of di-4-ANBDQPQ, during which hemodynamic effects were not seen, rhod-2(AM) application by direct root injection required ECMO support, as the $[Ca^{2+}]_i$ dye could lead to asystolic arrest during initial injection, with subsequent beating recoverable with circulatory support (which was always needed for calcium dye experiments). Dye loading protocols in vivo need to be optimised. Our data, however, shows that it is possible in principal to conduct combined V_m and $[Ca^{2+}]_i$ imaging in the blood-perfused mammalian heart in vivo.

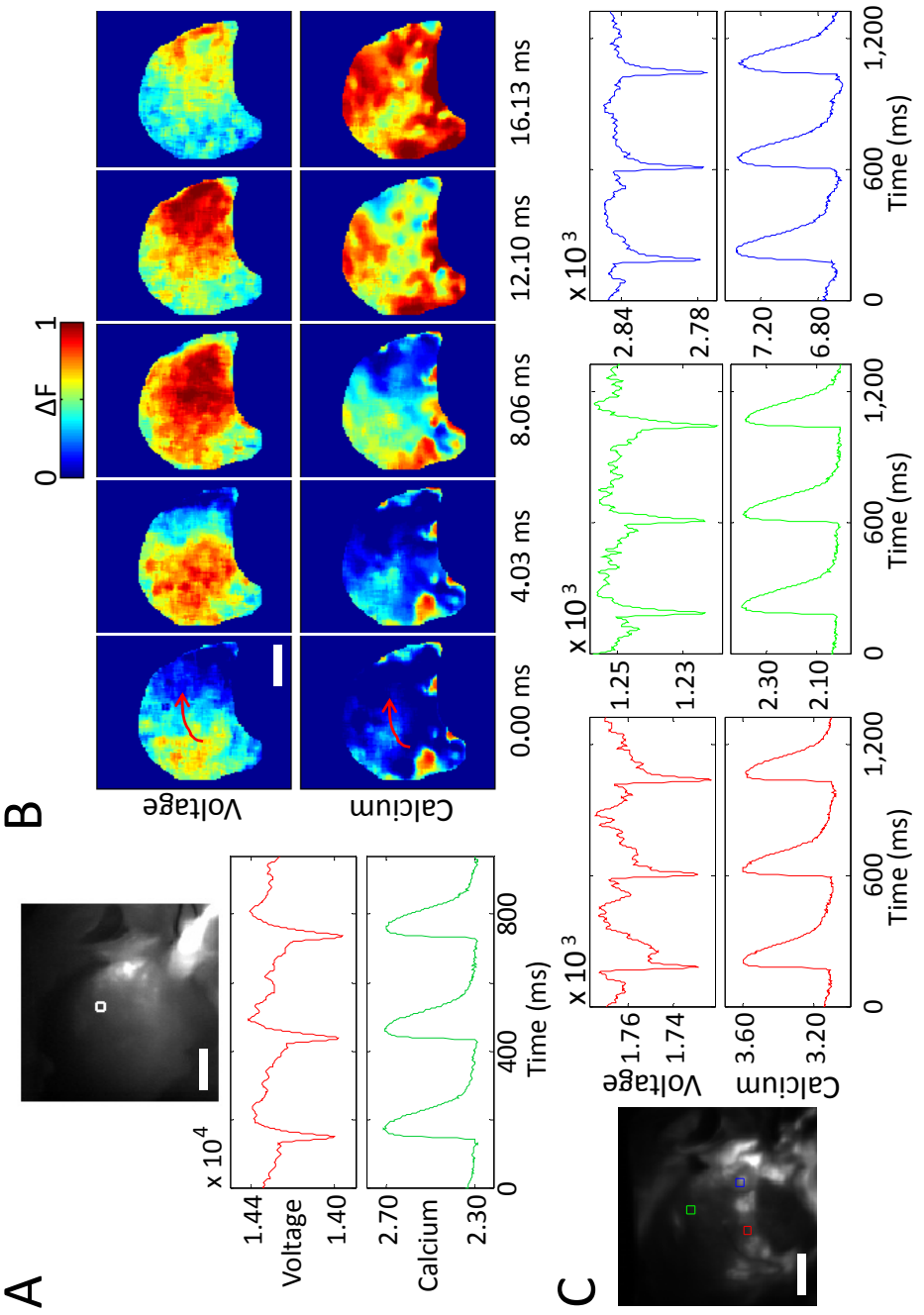

FIGURE 3-17 - IN VIVO IMAGING OF V_M AND $[Ca^{2+}]_I$ DYNAMICS IN RAT VENTRICLES DURING SINUS RHYTHM. (A) AP (RED) AND CAT (GREEN) FLUORESCENCE SIGNALS TAKEN FROM THE 464-PIXEL WHITE-SQUARE REGION HIGHLIGHTED IN THE TOP PANEL (LEFT VENTRICLE). (B) NORMALIZED FLUORESCENCE INTENSITY MAPS (COLORBAR SHOWN) FOR V_M AND $[Ca^{2+}]_I$ DURING SINUS RHYTHM FROM THE SAME HEART; NOTE THE PREVIOUSLY MENTIONED DELAY BETWEEN V_M AND $[Ca^{2+}]_I$ PEAKS (RED ARROW INDICATES ELECTRICAL WAVE PROPAGATION DIRECTION). (C) AP (TOP TRACES) AND CAT (BOTTOM TRACES) FLUORESCENCE SIGNALS TAKEN FROM THREE 464-PIXEL SQUARE REGIONS FROM THE LEFT VENTRICLE OF ANOTHER HEART, SHOWING VARYING MOTION ARTIFACT EFFECTS. SCALE BAR = 5 MM. FOR THESE IMAGES, BLEBBISTATIN WAS USED TO REDUCE, BUT NOT ELIMINATE, THE CONTRIBUTION OF MOTION TO THE SIGNALS. FOR B, NON-UNIFORM DYE-LOADING AND MOTION ARTIFACT ARE THE CAUSE OF SIGNAL QUALITY HETEROGENEITY.

CHAPTER 4. DISCUSSION AND CONCLUSIONS

It has been recognized for more than three decades that following cardiac arrest, myocardial dysfunction occurs[32] and is a critical factor in recovery.[31] To date, most research focused on ischemia-reperfusion has used a Langendorff isolated heart preparation to investigate mechanisms and concluded that calcium transients are not increased. Here, we have developed an *in vivo* model of post-myocardial cardiac arrest ventricular dysfunction which leaves neurohormonal responses intact. Using this model, we describe a greatly increased calcium induced calcium release in isolated cardiac myocytes reproduced by in vivo epinephrine infusion and brain stem death. We also find cardiac calcium memory to be mediated by autophosphorylation of CAMKII. We also find it to be dependent on ryanodine receptor calcium but not PKA activation in vivo. Finally, we found that a small molecular activator of the aldehyde dehydrogenase 2 dramatically improves cardiac performance at the whole heart and cellular level and reduces autophosphorylation of CAMKII, consistent with a role for aldehydic stress in the injury mechanism.

The role of CAMKII has been described in seminal investigations.[42,75-77] Its activation has been found to be important in the generation of electrical storm[73] while after I/R, inhibition can prevent the occurrence of ventricular arrhythmias.[78] Here we hypothesize that acute myofilament dysfunction leads to an increase in CICR which leads to auto-activation of CAMKII and triggers a more prolonged negative remodelling that can lead to cardiomyopathy. Such a proposed mechanism has similarities to neuronal

plasticity where CAMKII senses phasic changes and augments post-synaptic signals.[79] We speculate that just as the brain induces long-term potentiation[80] in the heart, the unique features of CAMKII autophosphorylation and its ability to follow calcium changes phasically[77] allow integration of the "post-synaptic" dyadic cleft calcium and generate a series of myopathic changes.[42,68,81-84]

In addition, we describe a system for measuring force and calcium simultaneously in isolated myocytes and establish a role for length dependent activation in the single cell Frank-Starling effect. Cell shortening, while a reliable measure as an indicator of cell function grossly, does not allow interrogation of the cellular equivalent of the Frank-Starling Law. Furthermore, in spite of the important information gleaned from the carbon fiber system on load-dependent force, the underlying mechanism of calcium regulated length dependent activation cannot be fully characterised without some characterisation of calcium and force. Indeed, while surrogates of the role of calcium on isometric force can be made with skinned fiber preparations, one of the critical components missing in understanding force generation is a description of the dynamic calcium-force interaction in response to action potential evoked CICR.[85]

Our data has several limitations. We cannot directly verify whether adrenergic activation persists in the isolated cells. It is worth noting that the response to acute catecholamines, however, was different than subacute

infusion, and that calcium cardiac memory was CAMKII dependent, not PKA dependent. Furthermore, existing data in cultured ventricular cells has already demonstrated that catecholaminergic signalling switches from a PKA dependent pathway to a CAMKII dependent pathway with more chronic infusion. Though we have demonstrated that calcium measurements can be made in live animals in situ, the complexity of cardiac arrest with recovery and calcium dye measurements has at present been elusive. Preliminary data from brainstem herniation seems to support the in vivo expression of calcium cardiac memory, though this remains to be verified as the technique of in vivo measurements is perfected.

We show that inhibiting aldehydic adduct formation during arrest/reperfusion increases myofilament sensitivity, reduces CaMKII activation, and improves survival. These mechanisms should be explored further as potential targets for human therapeutic trials.

With in-situ Optical Mapping of Voltage and Calcium in the heart we introduce a multi-parametric imaging approach, building on a near-infrared voltage dye and red-shifted calcium dye, which relies on a multi-band filter to study two key parameters responsible for arrhythmia in vivo using a single camera. The technique, also suitable for Langendorff-perfused hearts, is scalable and less expensive than traditional optical mapping methods. In contrast to the single previous report on in vivo optical mapping,[51] our system is adaptable, in principle, to trans-catheter endoscopic methods,

such as used to visualise the endocardium in humans[86-89] opening the door to clinical development as an arrhythmia mapping tool.

Because EAM suffers from suboptimal spatiotemporal resolution and can be very time consuming,[90,91] alternative invasive modalities have been developed to circumvent some of these limitations. As an example, direct endocardial visualisation through optical catheters can simplify the procedure of ablation by relying on visualized anatomy through a saline-filled balloon.[92,93] However, visualization catheters do not report complex electrical activity by comparison to EAM. With its high spatiotemporal resolution, optical mapping may meet this need by allowing for complex electrophysiology and direct anatomy to be mapped simultaneously through a minimally invasive approach. In addition, because optical catheters can visualize ablation lesions,[87] in combination with optical mapping, it may be possible to visualize the interplay of ablation lesions and electrical block. Optical mapping also allows $[Ca^{2+}]_i$ measurements, a parameter not accessible to traditional EAM. Given the interplay of V_m and $[Ca^{2+}]_i$ in arrhythmogenesis,[49] clinically mapping this parameter could be fruitful. Finally, optical mapping can be conducted beat by beat, allowing for mapping of transient arrhythmias or infrequent ectopic events.

In-situ optical mapping has several limitations. First and foremost, we have yet to couple our imaging system to a direct visualisation catheter. Second, in our experiments, excitation-contraction un-couplers were needed to reduce motion artifact from fluorescence transients, which is undesirable.

However, motion correction algorithms[94] and ratiometric imaging of fluorescence transients[95] have been used extensively to deal with motion artifacts in signals. In the isolated heart preparation, mechanical restriction or ratiometric imaging with post-acquisition motion tracking has been shown to significantly reduce motion artifacts, but imaging a strongly contracting whole-heart is still an unsolved problem.[52] Indeed, an even simpler approach has been used with direct visualisation catheters where local mechanical immobilisation by the endocardial balloon successfully limits motion artifacts,[86] even as applied to high resolution laser based ablation in patients.[96] Third, while we found no evidence of short-term detrimental effects of di-4-ANBDQPQ, long term toxicity studies need to be done. However, the recent track record in voltage-sensitive dye development has been impressive, making us optimistic overall. Fourth, the calcium arrest seen during in vivo loading is thought to be caused by the calcium-buffering properties of the dye on either intra- or extracellular calcium levels. Further exploration of lower- affinity calcium dyes with red-shifted emissions may prove fruitful. In spite of these significant limitations discussed above, this proof-of-principle investigation confirms that ‘optical EAM’ is possible in vivo and argues for continued development.

CHAPTER 5. FUTURE DIRECTION

Our aim was to undertake scientific assessment of hearts resuscitated following circulatory arrest using a small animal model of DCD heart donation. We hypothesized that reperfusion of the heart after cardiac arrest would result in recovery of cardiac activity with sufficient function to allow for transplantation. The hypothesis was based on the fact that historical experience of heart transplantation used organs removed after cardiac arrest.

Having shown that following cardiac arrest with a 15 minute warm ischaemic time it is possible to resuscitate the heart and also by treating the animals with a small molecular activator of the aldehyde dehydrogenase 2 to dramatically improve the cardiac function at the whole heart and cellular level opens doors to the potential of using hearts from the DCD donor for transplantation. We show that inhibiting aldehydic adduct formation during arrest/reperfusion increases myofilament sensitivity, reduces CaMKII activation, and improves survival. These mechanisms should be explored further as potential targets for human therapeutic trials.

Work from our group has carried on looking into DCD hearts as potential organs for transplantation – in particular with regards to resuscitation in the donor and then ex-vivo blood perfusion on a custom rig. The organ care system developed by Transmedics is an example of an ex-vivo perfusion

system designed to perfuse the donor heart with oxygenated blood. This device allows for continuous biochemical assessment as well as functional assessment.

In July 2014 the first adult heart transplant from a DCD donor was transplanted in Australia.[97] In March of 2015 Papworth Hospital performed the first DCD heart transplant in Europe. The clinical programme is ongoing and so far 32 DCD hearts have been transplanted successfully. Early combined international results from 4 centres utilising DCD donor hearts have reported a 30 day survival of 96.4%.[98] At Papworth hospital DCD donors have increased the overall cardiac transplant activity by 45%.[99] These short-term results have been reassuring and we await long term follow up.

Further work is currently ongoing into reconditioning of both the DCD and DBD hearts with ex-vivo perfusion. The agonal phase in the DCD donor can vary greatly from 1 minute – 130 minutes,[99] the impact of this on donor heart function is unknown and this provides an avenue for future research.

CHAPTER 6. APPENDICES

6.1. TIMING AND VENUE OF RESEARCH

The work described in this thesis was conducted between May 2010 to October 2011, at the Falk Cardiovascular Research Institute at Stanford University Medical Center (Palo Alto, CA)

6.2. RESEARCH FUNDING

The author was awarded The Gledhill Fellowship by Papworth Hospital NHS Foundation Trust. The work at Stanford was supported by Dr. Euan Ashley's laboratory.

6.3. ATTRIBUTIONS

The author is very grateful to contributions to this body of research made by colleagues and collaborators. I would like to thank Photometrics for graciously loaning their Evolve- 128 EMCCD camera for the in vivo studies. The author is directly responsible for the design, planning, execution and analyses of all experiments and the preparation of this thesis

.

CHAPTER 7. BIBLIOGRAPHY

1. Large, S. R. Is there a crisis in cardiac transplantation? *Lancet* **359,** 803–804 (2002).
2. Alonso, A. *et al.* Renal Transplantation From Non–Heart-Beating Donors: A Single-Center 10-Year Experience. *Transplant Proc* **37,** 3658–3660 (2005).
3. D'alessandro, A. M. *et al.* Liver transplantation from controlled non-heart-beating donors. *Surgery* **128,** 579–588 (2000).
4. Abt, P. L. *et al.* Survival following liver transplantation from non-heart-beating donors. *Ann. Surg.* **239,** 87–92 (2004).
5. De Vleeschauwer, S. *et al.* Early outcome after lung transplantation from non-heart-beating donors is comparable to heart-beating donors. *J Heart Lung Transplant* **28,** 380–387 (2009).
6. Steen, S. *et al.* Transplantation of lungs from non-heart-beating donors after functional assessment ex vivo. *ATS* **76,** 244–52– discussion 252 (2003).
7. Barnard, C. N. The operation. A human cardiac transplant: an interim report of a successful operation performed at Groote Schuur Hospital, Cape Town. *S. Afr. Med. J.* **41,** 1271–1274 (1967).
8. Boucek, M. M. *et al.* Pediatric heart transplantation after declaration of cardiocirculatory death. *N Engl J Med* **359,** 709–714 (2008).
9. Ali, A. *et al.* Cardiac recovery in a human non-heart-beating donor after extracorporeal perfusion: source for human heart donation? *J Heart Lung Transplant* **28,** 290–293 (2009).
10. Noterdaeme, T. *et al.* What is the potential increase in the heart graft pool by cardiac donation after circulatory death? *Transplant International* **26,** 61–66 (2012).
11. Van Norman, G. A. Another Matter of Life and DeathWhat Every Anesthesiologist Should Know about the Ethical, Legal, and Policy Implications of the Non–Heart-beating Cadaver Organ Donor. *Anesthesiology* **98,** 763–773 (2003).
12. A definition of irreversible coma. Report of the Ad Hoc Committee of the Harvard Medical School to Examine the Definition of Brain Death. *JAMA* **205,** 337–340 (1968).
13. Vliet, V. D., Slooff, M. J. H., Rijkmans, B. G. & Kootstra, G. Use of Non-Heart-Beating Donor Kidneys for Transplantation. *Eur Surg Res* **13,** 354–360 (1981).
14. MA, V., KM, L., GG, P. & G, K. Short- and long-term results with adult non-heart-beating donor kidneys. *Transplant Proc* **20,** 743–745 (1988).
15. Wynen, R. M. *et al.* Long-term follow-up of transplanted non-heart-beating donor kidneys: preliminary results of a retrospective study. *Transplant Proc* **25,** 1522–1523 (1993).
16. Wijnen, R. M. *et al.* Outcome of transplantation of non-heart-beating donor kidneys. *Lancet* **345,** 1067–1070 (1995).
17. Matesanz, R. & Miranda, B. Outcome of transplantation of non-heart-beating donor kidneys. *Lancet* **346,** 53 (1995).

18. Daemen, J. H. *et al.* Non-heart-beating donor program contributes 40% of kidneys for transplantation. *Transplant Proc* **28,** 105–106 (1996).
19. TRANSPLANTATION, N. B. A. Organ Donationand Transplantation. 1–167 (2015).
20. Purshouse, K., Large, S., Dargie, H., Dunning, J. & Neuberger, J. Is There a Crisis in Heart Transplantation? Reflection over 10 Years. *Open Journal of Organ Transplant Surgery* **2,** 1–4 (2012).
21. TRANSPLANTATION, N. B. A. ANNUAL REPORT ON CARDIOTHORACIC TRANSPLANTATION 2014/15. 1–131 (2015).
22. Lannon, J. D. *et al.* The UK Retrieval Team 'Scout' Pilot Programme. *HEALUN* **33,** S162 (2014).
23. McKeown, D. W., Bonser, R. S. & Kellum, J. A. Management of the heartbeating brain-dead organ donor. *British Journal of Anaesthesia* **108,** i96–i107 (2011).
24. Salim, A. *et al.* The Effect of a Protocol of Aggressive Donor Management: Implications for the National Organ Donor Shortage. *J Trauma* **61,** 429–435 (2006).
25. Grafton, G., Samoukovic, G. & Colvin, M. M. Cardiac Donor Selection and Management. *Curr Transpl Rep* **2,** 338–344 (2015).
26. FOUNDATION, B. H. AHeart transplant will transformmy life. 1–41 (2015).
27. Nolan, J. P. *et al.* Post-cardiac arrest syndrome: Epidemiology, pathophysiology, treatment, and prognostication. *Resuscitation* **79,** 350–379 (2008).
28. Stub, D., Bernard, S., Duffy, S. J. & Kaye, D. M. Post Cardiac Arrest Syndrome: A Review of Therapeutic Strategies. *Circulation* **123,** 1428–1435 (2011).
29. Kilgannon, J. H. *et al.* Early arterial hypotension is common in the post-cardiac arrest syndrome and associated with increased in-hospital mortality. *Resuscitation* **79,** 410–416 (2008).
30. Zia, A. & Kern, K. B. Management of postcardiac arrest myocardial dysfunction. *Current Opinion in Critical Care* **17,** 241–246 (2011).
31. Kern, K. B., Hilwig, R. W., Rhee, K. H. & Berg, R. A. Myocardial dysfunction after resuscitation from cardiac arrest: an example of global myocardial stunning. *J Am Coll Cardiol* **28,** 232–240 (1996).
32. Bolli, R. & Marbán, E. Molecular and cellular mechanisms of myocardial stunning. *Physiological Reviews* **79,** 609–634 (1999).
33. Zaugg, C. E., Ziegler, A., LEE, R. J., Barbosa, V. & Buser, P. T. Postresuscitation stunning: postfibrillatory myocardial dysfunction caused by reduced myofilament Ca2+ responsiveness after ventricular fibrillation-induced myocyte Ca2+ overload. *Journal of Cardiovascular Electrophysiology* **13,** 1017–1024 (2002).
34. Weiss, J. N., Nivala, M., Garfinkel, A. & Qu, Z. Alternans and Arrhythmias: From Cell to Heart. *Circulation Research* **108,** 98–112 (2011).
35. Kim, S.-J., Depre, C. & Vatner, S. F. Novel mechanisms mediating stunned myocardium. *Heart Fail Rev* **8,** 143–153 (2003).
36. Solaro, R. J. & Arteaga, G. M. Heart failure, ischemia/reperfusion injury and cardiac troponin. *Adv. Exp. Med. Biol.* **592,** 191–200 (2007).

37. Salas, M. A. *et al.* Journal of Molecular and Cellular Cardiology. *Journal of Molecular and Cellular Cardiology* **48,** 1298–1306 (2010).
38. Vittone, L., Mundiña-Weilenmann, C. & Mattiazzi, A. Phospholamban phosphorylation by CaMKII under pathophysiological conditions. *Front. Biosci.* **13,** 5988–6005 (2008).
39. VALVERDE, C. *et al.* Phospholamban phosphorylation sites enhance the recovery of intracellular Ca2+ after perfusion arrest in isolated, perfused mouse heart. *Cardiovascular Research* **70,** 335–345 (2006).
40. Valverde, C. A. *et al.* Transient Ca2+ depletion of the sarcoplasmic reticulum at the onset of reperfusion. *Cardiovascular Research* **85,** 671–680 (2010).
41. Kusuoka, H., Koretsune, Y., Chacko, V. P., Weisfeldt, M. L. & Marbán, E. Excitation-contraction coupling in postischemic myocardium. Does failure of activator Ca2+ transients underlie stunning? *Circulation Research* **66,** 1268–1276 (1990).
42. Zhang, R. *et al.* Calmodulin kinase II inhibition protects against structural heart disease. *Nat Med* **11,** 409–417 (2005).
43. Ali, A. A. *et al.* Hearts From DCD Donors Display Acceptable Biventricular Function After Heart Transplantation in Pigs. *American Journal of Transplantation* **11,** 1621–1632 (2011).
44. Bhakta, D. & Miller, J. M. Principles of electroanatomic mapping. *Indian Pacing Electrophysiol J* **8,** 32–50 (2008).
45. Gepstein, L., Hayam, G. & Ben-Haim, S. A. A novel method for nonfluoroscopic catheter-based electroanatomical mapping of the heart. In vitro and in vivo accuracy results. *Circulation* **95,** 1611–1622 (1997).
46. Efimov, I. R. Optical Imaging of the Heart. *Circulation Research* **95,** 21–33 (2004).
47. Salama, G. & Hwang, S.-M. Simultaneous optical mapping of intracellular free calcium and action potentials from Langendorff perfused hearts. *Curr Protoc Cytom* **Chapter 12,** Unit 12.17 (2009).
48. Skrzypiec-Spring, M., Grotthus, B., Szelag, A. & Schulz, R. Isolated heart perfusion according to Langendorff---still viable in the new millennium. *J Pharmacol Toxicol Methods* **55,** 113–126 (2007).
49. Bers, D. M. Calcium Cycling and Signaling in Cardiac Myocytes. *Annu. Rev. Physiol.* **70,** 23–49 (2008).
50. DING, C. *et al.* High-Resolution Optical Mapping of Ventricular Tachycardia in Rats with Chronic Myocardial Infarction. *Pacing and Clinical Electrophysiology* **33,** 687–695 (2010).
51. Dillon, S. M., Kerner, T. E. & Hoffman, J. A system for in-vivo cardiac optical mapping. *IEEE Eng Med Biol Mag* 95–108 (1998).
52. Herron, T. J., Lee, P. & Jalife, J. Optical Imaging of Voltage and Calcium in Cardiac Cells & Tissues. *Circulation Research* **110,** 609–623 (2012).
53. Matiukas, A. *et al.* Near-infrared voltage-sensitive fluorescent dyes optimized for optical mapping in blood-perfused myocardium. *HRTHM* **4,** 1441–1451 (2007).
54. Waggoner, A. S., Wachman, E. S. & Farkas, D. L. Optical filtering systems for wavelength selection in light microscopy. *Curr Protoc Cytom* **Chapter 2,** Unit 2.4 (2001).

55. Lee, P. *et al.* Single-sensor system for spatially resolved, continuous, and multiparametric optical mapping of cardiac tissue. *Heart Rhythm* **8,** 1482–1491 (2011).
56. Entcheva, E., Kostov, Y., Tchernev, E. & Tung, L. Fluorescence imaging of electrical activity in cardiac cells using an all-solid-state system. *IEEE Trans Biomed Eng* **51,** 333–341 (2004).
57. van der Hoeven, J. A. *et al.* Induction of organ dysfunction and up-regulation of inflammatory markers in the liver and kidneys of hypotensive brain dead rats: a model to study marginal organ donors. *Transplantation* **68,** 1884–1890 (1999).
58. Charo, D. N. *et al.* Endogenous regulation of cardiovascular function by apelin-APJ. *Am J Physiol Heart Circ Physiol* **297,** H1904–13 (2009).
59. Woods, C. E., Novo, D., DiFranco, M. & Vergara, J. L. The action potential-evoked sarcoplasmic reticulum calcium release is impaired in mdx mouse muscle fibres. *J. Physiol. (Lond.)* **557,** 59–75 (2004).
60. Iribe, G., Helmes, M. & Kohl, P. Force-length relations in isolated intact cardiomyocytes subjected to dynamic changes in mechanical load. *Am J Physiol Heart Circ Physiol* **292,** H1487–H1497 (2006).
61. Bollensdorff, C., Lookin, O. & Kohl, P. Assessment of contractility in intact ventricular cardiomyocytes using the dimensionless 'Frank–Starling Gain' index. *Pflugers Arch - Eur J Physiol* **462,** 39–48 (2011).
62. Cribier, A. *et al.* Technique of transcatheter aortic valve implantation with the Edwards-Sapien heart valve using the transfemoral approach. *Herz* **34,** 347–356 (2009).
63. Fedorov, V. V. *et al.* Application of blebbistatin as an excitation-contraction uncoupler for electrophysiologic study of rat and rabbit hearts. *HRTHM* **4,** 619–626 (2007).
64. Edgar, P., Bullock, R. & Bonner, S. Management of the potential heart-beating organ donor. *Contin Educ Anaesth Crit Care Pain* **4,** 86–90 (2004).
65. Novitzky, D., Wicomb, W. N., Cooper, D. & Rose, A. G. *Novitzky: Electrocardiographic, hemodynamic and endocrine... - Google Scholar*. (J Heart Transplant, 1984).
66. Szabó, G. *et al.* Role of neural and humoral factors in hyperdynamic reaction and cardiac dysfunction following brain death. *HEALUN* **19,** 683–693 (2000).
67. Szabó, G., Hackert, T., Sebening, C., Vahl, C. F. & Hagl, S. Modulation of coronary perfusion pressure can reverse cardiac dysfunction after brain death. *ATS* **67,** 18–25– discussion 25–6 (1999).
68. Grimm, M. & Brown, J. H. β-Adrenergic receptor signaling in the heart: Role of CaMKII. *Journal of Molecular and Cellular Cardiology* **48,** 322–330 (2010).
69. Wang, W. Sustained 1-Adrenergic Stimulation Modulates Cardiac Contractility by Ca2+/Calmodulin Kinase Signaling Pathway. *Circulation Research* **95,** 798–806 (2004).
70. Gao, W. D., Backx, P. H., Azan-Backx, M. & Marbán, E. Myofilament Ca2+ sensitivity in intact versus skinned rat ventricular muscle. *Circulation Research* **74,** 408–415 (1994).
71. Fabiato, A. & Fabiato, F. Dependence of the contractile activation of

skinned cardiac cells on the sarcomere length. *Nature* **256,** 54–56 (1975).
72. de Tombe, P. P. *et al.* Journal of Molecular and Cellular Cardiology. *Journal of Molecular and Cellular Cardiology* **48,** 851–858 (2010).
73. Chen, C.-H. *et al.* Activation of aldehyde dehydrogenase-2 reduces ischemic damage to the heart. *Science* **321,** 1493–1495 (2008).
74. Qian, Y. W., Clusin, W. T., Lin, S. F., Han, J. & Sung, R. J. Spatial Heterogeneity of Calcium Transient Alternans During the Early Phase of Myocardial Ischemia in the Blood-Perfused Rabbit Heart. *Circulation* **104,** 2082–2087 (2001).
75. Grueter, C. E., Colbran, R. J. & Anderson, M. E. CaMKII, an emerging molecular driver for calcium homeostasis, arrhythmias, and cardiac dysfunction. *J Mol Med* **85,** 5–14 (2006).
76. Bers, D. M. Cardiac excitation-contraction coupling. *Nature* **415,** 198–205 (2002).
77. Song, Q., Saucerman, J. J., Bossuyt, J. & Bers, D. M. Differential integration of Ca2+-calmodulin signal in intact ventricular myocytes at low and high affinity Ca2+-calmodulin targets. *J. Biol. Chem.* **283,** 31531–31540 (2008).
78. Bell, J. R., Curl, C. L., Ip, W. T. K. & Delbridge, L. M. D. International Journal of Cardiology. *International Journal of Cardiology* 1–7 (2011). doi:10.1016/j.ijcard.2011.02.038
79. Amici, M. *et al.* Neuronal calcium sensors and synaptic plasticity. *Biochem. Soc. Trans* **37,** 1359 (2009).
80. Okamoto, K., Bosch, M. & Hayashi, Y. The Roles of CaMKII and F-Actin in the Structural Plasticity of Dendritic Spines: A Potential Molecular Identity of a Synaptic Tag? *Physiology* **24,** 357–366 (2009).
81. Saucerman, J. J. & Bers, D. M. Journal of Molecular and Cellular Cardiology. *Journal of Molecular and Cellular Cardiology* 1–5 (2011). doi:10.1016/j.yjmcc.2011.06.005
82. VILAPETROFF, M. *et al.* CaMKII inhibition protects against necrosis and apoptosis in irreversible ischemia–reperfusion injury. *Cardiovascular Research* **73,** 689–698 (2007).
83. Passier, R. *et al.* CaM kinase signaling induces cardiac hypertrophy and activates the MEF2 transcription factor in vivo. *J. Clin. Invest.* **105,** 1395–1406 (2000).
84. Schott, P. *et al.* Proteome changes in CaMKII. *Cardiovascular Pathology* **19,** e241–e250 (2010).
85. de Tombe, P. P. & Granzier, H. L. The cytoskeleton and the cellular transduction of mechanical strain in the heart: a special issue. *Pflugers Arch - Eur J Physiol* **462,** 1–2 (2011).
86. Anh, D. J. *et al.* Characterization of human coronary sinus valves by direct visualization during biventricular pacemaker implantation. *Pacing Clin Electrophysiol* **31,** 78–82 (2008).
87. Eversull, C. S. *et al.* Direct visualization of cardiac radiofrequency ablation lesions. *J Cardiovasc Transl Res* **2,** 198–201 (2009).
88. Anh, D. J. *et al.* Early human experience with use of a deflectable fiberoptic endocardial visualization catheter to facilitate coronary sinus cannulation. *HRTHM* **3,** 875–878 (2006).
89. Irani, A. R. *et al.* Visualizing ablation gaps in vitro using a deflectable

fiber optic endocardial visualization catheter. *J Interv Card Electrophysiol* **25,** 107–110 (2009).
90. LaPage, M. J. & Saul, J. P. Update on rhythm mapping and catheter navigation. *Curr Opin Cardiol* **26,** 79–85 (2011).
91. Hameedullah, I. & Chauhan, V. S. Clinical considerations for allied professionals: understanding and optimizing three-dimensional electroanatomic mapping of complex arrhythmias--part 1. *Heart Rhythm* **6,** 1249–1252 (2009).
92. Metzner, A. *et al.* One-year clinical outcome after pulmonary vein isolation using the novel endoscopic ablation system in patients with paroxysmal atrial fibrillation. *Heart Rhythm* **8,** 988–993 (2011).
93. Gerstenfeld, E. P. & Michele, J. Pulmonary vein isolation using a compliant endoscopic laser balloon ablation system in a swine model. *J Interv Card Electrophysiol* **29,** 1–9 (2010).
94. Rohde, G. K., Dawant, B. M. & LIN, S.-F. Correction of motion artifact in cardiac optical mapping using image registration. *IEEE Trans Biomed Eng* **52,** 338–341 (2005).
95. KONG, W., WALCOTT, G. P., SMITH, W. M., JOHNSON, P. L. & KNISLEY, S. B. Emission Ratiometry for Simultaneous Calcium and Action Potential Measurements with Coloaded Dyes in Rabbit Hearts: Reduction of Motion and Drift. *Journal of Cardiovascular Electrophysiology* **14,** 76–82 (2003).
96. Phillips, K. P. *et al.* Anatomic location of pulmonary vein electrical disconnection with balloon-based catheter ablation. *Journal of Cardiovascular Electrophysiology* **19,** 14–18 (2008).
97. FRCS-CTh, K. K. D. *et al.* Adult heart transplantation with distant procurement and ex-vivo preservation of donor hearts after circulatory death: a case series. *Lancet* **385,** 2585–2591 (2015).
98. Page, A. A., Messer, S., Tsui, S. S. & Large, S. R. Early Results Using Donation After Circulatory Death (DCD) Donor Hearts. *Curr Transpl Rep* 1–8 (2016). doi:10.1007/s40472-016-0106-9
99. Messer, S. J. *et al.* Functional assessment and transplantation of the donor heart after circulatory death. *J Heart Lung Transplant* **35,** 1443–1452 (2016).